DISSERTATION

NONLINEAR INTERNAL WAVE - TOPOGRAPHIC INTERACTION AND TURBULENT MIXING USING NUMERICAL SIMULATIONS

Submitted by

Matthew Roy Klema

Department of Civil & Environmental Engineering

In partial fulfillment of the requirements

For the Degree of Doctor of Philosophy

Colorado State University

Fort Collins, Colorado

Fall 2021

Doctoral Committee:

Advisor: Subhas Karan Venayagamoorthy

Peter Nelson
Sarah Rathburn
Christopher Thornton

ABSTRACT

NONLINEAR INTERNAL WAVE - TOPOGRAPHIC INTERACTION AND TURBULENT MIXING USING NUMERICAL SIMULATIONS

Stratified fluid mixing in the oceanic setting involves complex overturning processes and turbulence working against stable background stratification driving fluid interaction between regions of different density that arise due to temperature and salinity variations. Mixing across layers of constant density (isopycnals) occurs when overturning results from flow events such as the breaking of internal waves. Increased study of processes that contribute to turbulent mixing in stratified fluids help to improve our an understanding of oceanic circulation currents, thermohaline circulation, nutrient and pollutant mixing as well as informing global climate and weather models. Quantitative measurement of turbulence and turbulent mixing in the field is limited by the difficulty of making temporally and spatially resolved measurements. Numerical simulation has become an important tool in studies of turbulent processes in the stratified flow environment environment. Our understanding of these small scale processes increase our ability to explain and predict phenomena such as the weakening of the mid-Atlantic current. Recent increases in available computational resources have allowed for increases in simulation resolution but they remain insufficient to simultaneously resolve the large scale structures such as inertial gravity waves as well as turbulence, an inherently small scale process. This has led to most simulations at the large scale only allowing for studies of bulk flow processes with parameterized mixing. On the other hand, theoretically based simulations at the laboratory scale are not able to fully incorporate physically realistic processes that occur in the actual environment. In addition to simulations at the laboratory scale this research presents simulations at an intermediate scale in an effort to demonstrate that study at this scale is needed for bridging the observations at the small scale ($\leq 10\ m$) to the realistic field scale (~ 1000 m). There are no studies in the current literature comprehensively analyzing the interaction be-

tween internal waves and multiple topographic ridges such as those found in the Earth's oceans or multiple isolated structures such as seamounts, especially at scales smaller than the field scale ($\sim 1000\ m$) but larger than the laboratory scale ($\leq 10\ m$). Research on the physics of internal waves interacting with isolated and multiple ridges remains an open line of inquiry and are theorized to be the location of significant amounts of turbulent mixing. Intermediate scale simulations are needed to help display realistically reproducible results and demonstrate that the knowledge gained from larger parameterized simulations and resolved small-scale simulations can inform a broader understanding of stratified turbulence and mixing.

The Osborn model is one of the most common methods for parameterizing turbulence through the prescription of a turbulent eddy diffusivity $K_\rho = \Gamma\epsilon/N^2$, where Γ is a irreversible mixing coefficient, ϵ is the dissipation of turbulent kinetic energy and N is the buoyancy frequency. For various reasons, including the limitations of instrumentation, an assumption of a constant $\Gamma = 0.2$ and an isotropic ϵ is common when the turbulent eddy diffusivity is derived from field measurements of overturning flow scales and a single component of the velocity gradient tensor. Using direct numerical simulations (DNS) of stably stratified turbulence with an assumption of $\Gamma = 0.2$ results in K_ρ less than that computed directly from the DNS. Furthermore, for most stratified flows an assumption of an isotropic kinetic energy dissipation rate leads to an overestimate of K_ρ. Using DNS data, it is shown here that improved estimates of K_ρ computed directly from measured data can be obtained without either of these assumptions using the instantaneous vertical density profile and existing parameterizations derived from measurable quantities leading to better estimation of K_ρ. This finding has potential to greatly improve estimates of ocean mixing derived from measurements.

Rotation of the Earth visibly influences large scale structures in the oceanic environment such as internal gravity waves. DNS simulations with rotational forcing are used to examine rotations impact on the turbulent scales of flow. Analyses comparing calculated values of the irreversible mixing coefficient as a function of the turbulent Froude number in flows including forcing by Coriolis rotation f show no difference from flows without rotational forcing. Commonly the ratio

N/f is used for flow regime classification. A new parametric space denoting the relative forcing of f and N clearly shows the ambiguity of this dimensionless parameter for flow classification as a wide range of turbulence is observed in flows with the same N/f classification. A ratio of the turbulent diffusivity to the molecular diffusivity $\hat{\kappa} = K_\rho/\kappa$ is shown as a valuable tool for eliminating unrealistic flow simulations, where $\hat{\kappa} > 0(10)$ should be used to ensure a separation of molecular and turbulent scales. This analysis definitively shows that Coriolis forcing does not influence values of the mixing coefficient, a small scale parameter, and that classifications of flow regimes using N/f are clearly ambiguous. These results are combined with simulation results without rotation, with continuous forcing and with mean shear incorporated to show that all these simulations follow the same trends for the irreversible mixing coefficient Γ as a function of the turbulent Froude number ($Fr_t = \frac{\epsilon}{Nk}$).

Detailed analysis of a 43-simulation parametric study examines the interaction between internal waves and bottom topography, specifically oceanic ridges. Results show similar flow structures in relatively-larger scale flows, that do not resolve the smallest turbulent scales as those simulated at the laboratory scale. Bridging the gap between the laboratory scale and field scale is becoming possible with recent increases in computational resources. These simulations start to fill an obvious gap in research using numerical simulations. Flows with increased Froude number show increased turbulence, dissipation and non-linear dynamics. Critical slopes clearly concentrate internal wave beams as internal waves interact with topography increasing turbulence. Smaller ridge heights allow for more of the internal wave energy to be transmitted while a tall ridge reflects more energy. Formation of bolus cores are observed for conditions corroborating field and DNS observation of energy flux and flow structure. Topographic ridge height is shown to influence the characterization of turbulence in addition to the slope criticality and wave amplitude of forcing. Increased non-linearity of the internal waves combined with energy resulting from critical topographic slopes is shown to result in increased distribution and magnitude of turbulence. These flow conditions are shown to increase the mass and distance travelled by generated boluses, one of the most significant influences on turbulent mixing. There are no studies in the current literature comprehensively analyzing the interaction between internal waves and multiple ridges or multiple isolated structures especially at scales below the field scale ($\sim 100\ m$) and above the laboratory scale ($\leq 10\ m$). Much remains to be understood on the physics of internal waves interacting with isolated and multiple ridges. This work provides a start to the bridge in this simulation gap showing the utility of fundamental process models in informing physically realistic models and field measurements to improve understanding and prediction of mixing in stratified geophysical flows.

ACKNOWLEDGEMENTS

First, I would like to thank Dr. Karan Venayagamoorthy. The Ph.D. work presented here would not have been possible without his knowledge, encouragement, enthusiasm and support. Beyond directly guiding me through this journey of scientific research he has also become a mentor in aspects of life beyond academics. I am grateful for his efforts in promoting my research leading to support and funding through the U.S. Office of Naval Research. Funding from the Office of Naval Research under Grant No. N00014-18-1-2773 is gratefully acknowledged.

Additionally, I would also like to thank Dr. Christopher Thornton. In addition to serving as a member of my doctoral committee I was able to gain insight from his suggestions and advice during his mentorship as my master's thesis advisor. Also, I would like to thank Dr. Peter Nelson and Dr. Sara Rathburn for their helpful suggestions, advice and committee service. In addition to the initial encouragement to pursue study in engineering Dr. Laurie Williams has been a continual pillar of support, advice and encouragement advocating for graduate study, application of engineering for improving the world around us and an interest in teaching.

My colleagues in the EFML, Jessica Baker, Dr. Amrapalli Garanaik, Dr. Oladapo Asperi, Dr. Marie Rostello, Joe Pugh, Joey Sinclair and Harshit Mishra have all been a valuable source of conversation, ideas and support resulting in cherished memories and friendships.

The love and support of my family has been instrumental in this process. Thomas and Barbara Klema have always been willing to lend encouragement or an understanding hand or ear. My siblings Nathan, Julia and Mariah have all provided outlets for fun, provided positivity and at times necessary diversion. My dog Stella has been a loyal, fun and kind companion, making sure I balanced study and a healthy lifestyle. Ben Luck's friendship through this process has been invaluable source of strength.

Most importantly, I would like to my partner and wife Nora Flucke. Her love, support, encouragement, and sacrifice made pursuing this journey possible. I could not have done this without her.

TABLE OF CONTENTS

LIST OF TABLES

LIST OF FIGURES

Chapter 1

Introduction

1.1 Motivation

Fluids in the Earth's oceans and the atmosphere are typically stratified due to variations in temperature and/or salinity. If the fluid is stably stratified, then the higher density fluid lies below the fluid of a lower density. Vertical perturbations of a fluid of a certain density into fluids of different density leads to a restoration force driven by gravity or buoyancy and is the basis for the initial generation of internal waves. These oscillations are termed internal waves because they are internal to a fluid.

Interest in breaking internal waves, especially in the ocean, has been an increasing area of research and study. Understanding of internal wave generation, propagation and fate is seen as crucial to the understanding of global oceanic circulation (Thorpe, 2004). The turbulence resulting from the breaking of internal waves in the ocean is one of the dominant processes believed to have enough energy to be one of the main drivers of vertical mixing in the global ocean circulations (Kunze & Sanford, 1996; Polzin et al., 1997). Figure 1.1 show the variety of turbulent processes that create mixing in the ocean. Some of the depicted processes are driven by internal waves (e.g. breaking, reflection/interaction, internal tides, etc.) while others are surface tides, wind on the surface of the water and fluvial input. Length scales relevant in stratified flow vary from less than 1 mm to 100 m (Thorpe, 2004) while the energy-containing scales that drive the processes can be on the order of magnitude of the ocean or globe. As with the length scales, the characteristic time scales of the dynamic processes also vary. Relative distribution of processes as a function of time and length scales is shown in Figure 1.2. Turbulence can lead to the transport of sediment, nutrients and biological material in baroclinic intrusions. Numerous observations (Gregg, 1987; Kunze & Sanford, 1996; Kunze et al., 2006; Ledwell et al., 2011) show that there is weak mixing normal to the surfaces of constant density (isopycnals), which is known as diapycnal mixing. However, diapycnal (across isopycnal) mixing observations from near the boundaries, and specifically in regions of rough topography (Polzin et al., 1997; Klymak et al., 2006; Levine & Boyd, 2006) show increases in orders of magnitude which has led to the conjecture that internal wave breaking as a result of topographic interaction is a major source of mixing (Munk & Wunsch, 1998).

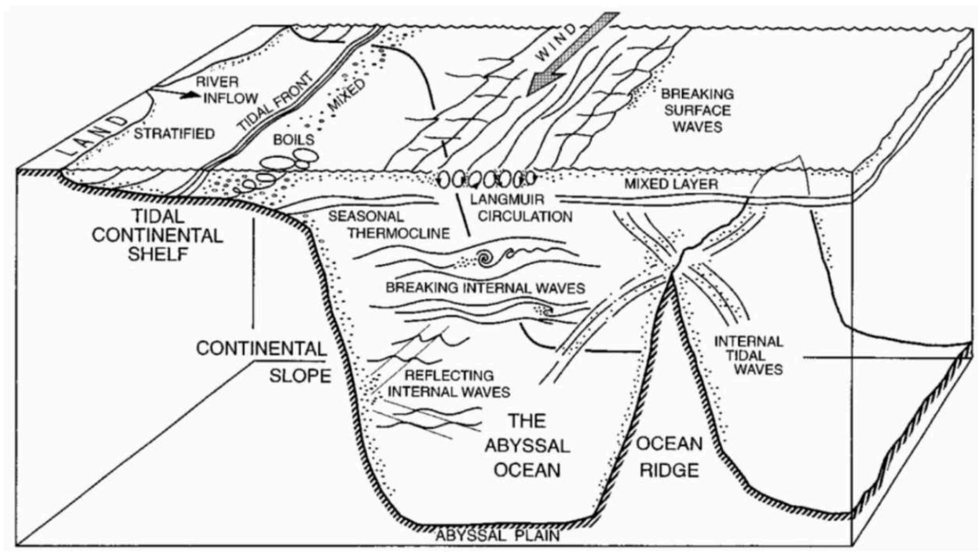

Figure 1.1: Sketch depicting processes that can lead to turbulence in the ocean. Depiction is not drawn to scale (Thorpe, 2004).

Quasi-steady mean flow over topography as a result of low frequency tidal oscillation leads to lee wave and hydraulic-jump type phenomena. Unlike the classical hydraulic jump in an open channel flow these waves and jumps are affected by and generally inhibited by the stratification. These types of phenomena have been observed in the field at a variety of locations (Wesson & Gregg, 1988; Alford et al., 2013; Nikurashin & Ferrari, 2013) suggesting that continued study of lee-wave driven turbulence should help inform the mixing processes accounted for in the next generation of climate and oceanic circulation models. Models currently are not able to fully account for all of these processes accurately. Internal wave interaction with barotropic tidal currents and bottom topography also leads to the generation of internal tides (Wunsch, 1975). Fate of these radiated low-mode internal tides is still uncertain (Garrett & Kunze, 2007) where some energy is thought to scatter into higher modes (St. Laurent & Garrett, 2002) as some energy moves into higher fre-

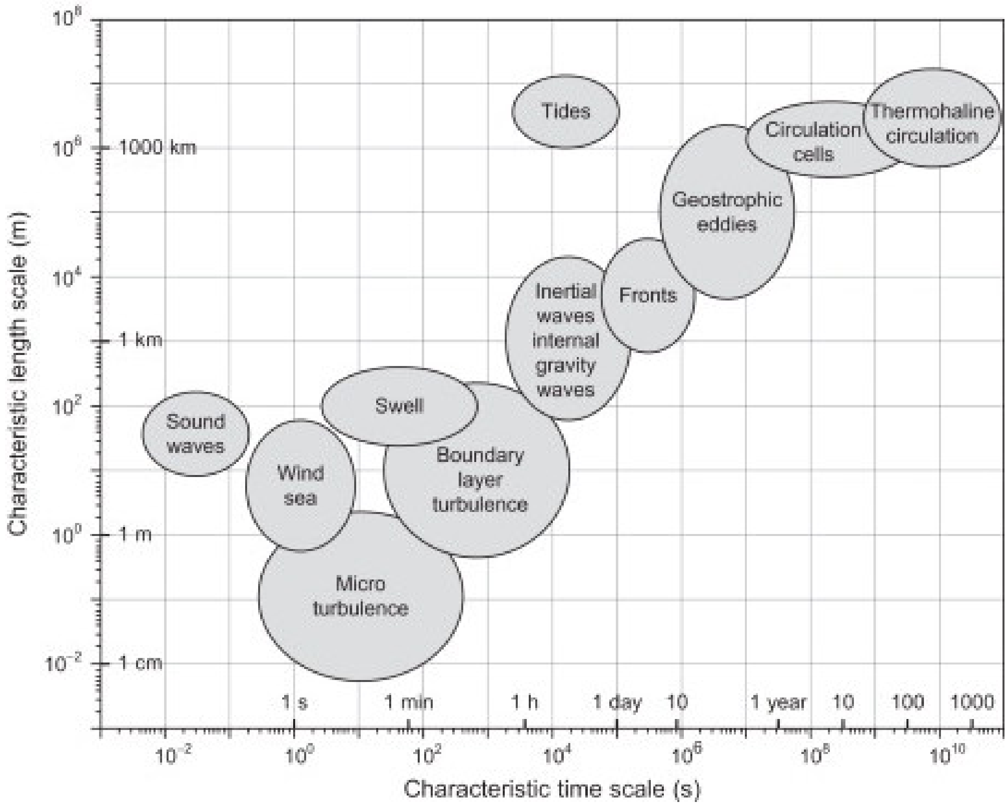

Figure 1.2: Illustration depicting the span of the relevant time and spatial scales in geophysical fluid dynamics (Cushman-Roisin & Beckers, 2008).

quency internal waves in the ocean interior (Polzin, 2009) or break on remote topographies across the ocean basin (Hult et al., 2009; Venayagamoorthy & Fringer, 2012). Plumes of high density fluid propagating into fresh unmixed fluid are called gravity currents and are important phenomena that impact mixing in a stratified fluid. Interactions of internal waves and topography result in turbulent mixing and the forcing of high density fluid cores upslope over or on top of topographic features in the form of boluses fluid flow (Venayagamoorthy & Fringer, 2007; Legg & Adcroft, 2003). Interaction of complex bathymetric topography and the internal wave field causes internal waves to steepen and break as a result shear or convective instability. Studies by Cacchione & Wunsch (1974), Helfrich (1992), Venayagamoorthy (2006), Shroyer et al. (2009) and Walter et al. (2014) extensively show the interaction of the internal wave field with a continental slope. Sarkar (2003) and Jalali et al. (2017) show some initial simulations that are compared to observational data from the South China Sea showing realistic models of the observed phenomena. Jarosz et al.

(2014) and Klymak et al. (2006) show that isolated mid ocean ridges can be considered turbulent mixing “hot spots." due to the internal wave induced mixing. Most initial simulations of the flow structure and the wave-topographic interaction model a simple, single triangular ridge at either laboratory ($\sim 1\ m$) or field scales ($> 1000\ m$). Numerical, experimental and observational studies of the turbulent mixing processes in these types of cases need additional research.

Using numerical studies, mixing due to internal wave breaking, both isolated and as a result of flow-topography interaction, can be parameterized in terms of the forcing of the wave energy and the geometric parameters of the topography. Internal waves are much more complex phenomena than surface waves as they are three-dimensional and are affected by the surrounding stratification that varies both spatially and temporally in the ocean as a result of current and wave propagation.

1.2 Background & Objectives

This dissertation research uses data derived from numerical simulations to study the fundamental physics of internal wave turbulence in stably stratified fluid flows in both an isolated setting and as a result of interaction with topography. The three main objectives of this research are as follows:

1. **Show how direct numerical simulations (DNS) can be used to inform field scale simulations and observations.** Use of informed dimensionless number parameterizations and consideration of flow physics can be used for improved estimates of ocean mixing. DNS results have the ability to enhance understanding of the processes and quantities that are difficult to measure directly in field settings and that are parameterized in numerical simulations at the field scale.

2. **To better understand the turbulence and mixing resulting from internal wave interaction with topographic ridges through a parametric study performed using geometric parameters but also with consideration of the forcing mechanism (i.e. mean flow, tidal flow).** Combinations of internal wave interaction with topography leads to bores, wave-wave interaction, hydraulic jumps and lee wave generation. This part of the research will extend the knowledge of internal waves and tides interacting with continental slopes (Venayag-

amoorthy & Fringer, 2006; Legg, 2004b) and isolated ridges (Klymak et al., 2012; Legg, 2014; Jalali et al., 2017). Furthermore, it will attempt to combine the results of the previous works and show how turbulent processes change under the conditions provided by variation to the bathymetry-wave interaction.

3. **Understand the influence of the precision and scale of numerical models for stratified flow problems.** Numerical modeling of natural processes is limited by scales. Computational resources are currently not sufficiently powerful to both resolve the smallest scales of turbulence and model a large field-scale simulation. This part of the research will be informed by results from laboratory-scale direct numerical simulations (DNS) and large eddy simulations (LES) that resolve the smaller scales to evaluate the results of intermediate-scale models that use parameterizations for turbulent mixing processes. Massachusetts Institute of Technology general circulation model (MITgcm), a widely used and accepted stratified flow modeling tool for large field-scale simulations (Marshall et al., 1997) was adapted and used for simulations at intermediate scales. Determination of the effect of large-scale processes such the rotation of the earth (Coriolis rotation) on the turbulence scales is also considered as an aspect of model scale effects.

Increased understanding of turbulent mixing process will impact areas of fundamental research, field-scale simulations of stratified turbulence, through parameterizations and robust parameter scalings relating relevant fluid and flow properties. The models analyzed here, as well as future models building on this research, will help inform applied field research through the ability to direct targeted measurement and data collection campaigns. At the broader level, this will help improve our understanding of global oceanic circulation and mixing through more physics based global climate models that inform societal decision making processes.

1.3 Dissertation Layout

The remainder of the dissertation is laid out in the following Chapters:

- Chapter 2 presents an analysis of the driving physics, governing equations as well as a discussion of different computational fluid dynamics modeling methods, direct numerical simulation (DNS) versus large eddy simulations (LES) versus Reynolds averaged Navier-Stokes (RANS) simulations.

- Chapter 3 covers a literature review of stably stratified flow, interactions of stratified flow with topography, as well as turbulent mixing and use of numerical simulations as a tool for helping to understand these processes. Descriptions of the methods and limitations of field measurement instrumentation are briefly discussed. Common non-dimensional parameters are introduced.

- Chapter 4 uses DNS data analyses to develop an improved method of inferring the diapycnal diffusivity/mixing from quantities measured in the field, directly addressing objective 1.

- Chapter 5 presents research completed in collaboration with the National Center for Atmospheric Research (NCAR) and uses DNS to show that while Coriolis rotation directly influences large-scale eddies of the flow, which supply the energy for mixing, it does not directly influence the smaller, turbulent scales of the flow. This chapter also addresses objective 1.

- Chapter 6 addresses objectives 2 and 3 through a two-dimensional parametric study of internal wave interactions with isolated Gaussian ridges at intermediate scales using highly resolved MITgcm simulations.

- Chapter 7 also addresses objectives 2 and 3 by looking at the flow structures present in the MITgcm simulations that result from internal wave interaction with ridge topography.

- Chapter 8 summarizes the conclusions that can be drawn from the work presented in the preceding chapters of the dissertation.

1.4 Summary

This dissertation presents work using numerical simulations to gain insight into the turbulent mixing processes in stratified flows occurring due to the interaction of nonlinear internal waves, internal tides and other phenomena in an isolated setting as well as a result of interaction with simulated bottom topography. Two DNS data sets are used to make scaling arguments with dimensionless parameters for improved understanding of turbulent processes and their inference. With a continuously stratified fluid a parametric study using a combination of forcing and geometric parameters is presented. Intermediate-scale range of simulations were used in a context to study turbulent mixing processes and see how well they compare with lab- and field-scale simulations. Also presented is how well turbulent mixing processes can be parameterized in larger-scale models for more accurate use of these modeling tools and accounting for the accuracy of modeled turbulence. Use of dimensional analysis and parametric space is also used to illustrate and isolate certain effects of turbulence and how these are parameterized in large-scale models and inferred from field measurements.

Chapter 2

Governing Equations and Numerical Methodology

This chapter presents the governing equations for fluid flow, a discussion on the scales of turbulence and overview of numerical approximation methods used to provide solutions to the Navier-Stokes equations. This chapter aims to provide the background needed for discussion of the relevant literature in Chapter 3 and the work presented in Chapters 4-7. These equations can be solved exactly in theory, but the complexity of highly turbulent flow creates a need for simplifying assumptions, parameterizations and solutions based on numerical approximation.

2.1 Governing Equations

The governing equations of fluid motion are derived from the conservation of mass, momentum, and energy using the continuum hypothesis. The continuum hypothesis assumes that a fluid is a continuously deformable substance rather than a collection of individual molecules. Taking a discreet and deformable differential volume of fluid the Reynolds transport theorem is used to derive the conservation equations,

$$\frac{D\mathbf{B}_{sys}}{Dt} = \frac{\partial}{\partial t}\int_{cv} \rho\beta d\forall + \int_{cs} \rho\beta\mathbf{U}\cdot\hat{\mathbf{n}}dA \tag{2.1}$$

where β is a generic intensive (per unit of mass) property of B, ρ is the density of the fluid, $\mathbf{U}$ is the velocity vector at the system boundary and $\mathbf{n}$ is the unit normal vector, convention positive outward from the integral control volume surfaces. $\frac{D}{Dt}$ is notation for the substantial, or material derivative, of extensive property B following the system in this notation. The right-hand side of Eqs. (2.1) contains two terms that represent the instantaneous time rate of change of β within the control volume and the time rate of change of β within the system due to the amount of β entering and leaving the control volume, $\forall$.

Assuming a differential control volume and applying the Gauss divergence theorem to Eq. (2.1) coverts the equation to differential form. In terms of fluxes, the terms of the equation are the time rate of change of B within the system as the sum of the changes of β within a fixed control volume and the net flux of β through the control surfaces that define the control volume

$$\rho\frac{D\beta}{Dt} = \frac{\partial(\rho\beta)}{\partial t} + \nabla\cdot(\rho\beta\mathbf{U}). \tag{2.2}$$

2.1.1 Conservation of Mass

If the extensive property, B, of interest is mass then mass per unit mass, $\beta = 1$. Equation 2.2 simplifies to

$$0 = \frac{1}{\rho}\frac{D\rho}{Dt} + \nabla\cdot\mathbf{U}, \tag{2.3}$$

where the left hand side is equal to zero as mass can not be created or destroyed inside the system. This equation represents conservation of mass within a fixed control volume as a sum of material changes in density within the control volume and the net flux of mass through the control surfaces.

2.1.2 Conservation of Momentum

Newton's second law applied to a system of particles defines conservation of momentum where the sum of the forces acting on the system of fluid particles is equal to the change in momentum of the system. In integral form this is defined by

$$\frac{D}{Dt}\int_{sys}\mathbf{U}\rho d\rlap{/}V = \frac{\partial}{\partial t}\int_{cv}\mathbf{U}\rho d\rlap{/}V + \int_{cs}\mathbf{U}\rho\mathbf{U}\cdot\hat{\mathbf{n}}dA, \tag{2.4}$$

where $\beta = \mathbf{U}$. Application of the Gauss divergence theorem converts this equation to the differential form of Newton's second law written per unit volume of fluid

$$\rho \frac{D\mathbf{U}}{Dt} = -\nabla p + \rho \mathbf{f} + \nabla \cdot \tau_{ij}, \tag{2.5}$$

where the three terms on the right hand side of the equation represent the force of pressure, p, body forces, $\mathbf{f}$ and the rank tensor of viscous shear stress forces, τ_{ij}. If a constant density is assumed then there are 10 unknowns between the four equations in that comprise Eqs. (2.3) and Eq. (2.5). In order to close the set of equations, Stokes hypothesis can be applied assuming an incompressible (constant density) fluid $\tau_{ij} = 2\mu S_{ij}$, where μ is the dynamic viscosity and $S_{ij} = \frac{1}{2}\left(\frac{\partial U_i}{\partial x_j} + \frac{\partial U_j}{\partial x_i}\right)$, is the strain rate tensor. When this constitutive relation for τ_{ij} is substituted into equation 2.5 the resulting equation is the Navier-Stokes equation for incompressible fluid

$$\rho \frac{D\mathbf{U}}{Dt} = -\nabla p + \rho \mathbf{g} + \mu \nabla^2 \mathbf{U}, \tag{2.6}$$

where the dynamic viscosity is considered nearly constant and the only body force is a result of gravitational acceleration, g, $\mathbf{f} = \mathbf{g} = -\mathbf{k}g$.

2.1.3 Conservation of Energy

An equation of state and the thermodynamic equation are needed to close the system of equations given by Eqs. (2.3) and Eq. (2.6) when the density is not a known constant. The first law of thermodynamics states that the change of energy within a defined system is a result of heat transfer and work rate exchange between the system and the surroundings. The intensive property for defining conservation of energy is specific energy for a system of fluid particles $\mathcal{E} = e + \frac{1}{2}\mathbf{U}\cdot\mathbf{U} + \Phi$, where the respective terms on the right hand side of the equation represent the internal, kinetic and potential energies of the system. With $\beta = \mathcal{E}$ and following the same procedure as for conservation of mass and momentum the Reynolds transport theorem simplifies to

$$\rho \frac{D\mathcal{E}}{Dt} = -\nabla \cdot (\mathbf{q} + p\mathbf{U} - \tau_{ij} \cdot \mathbf{U}), \tag{2.7}$$

where $\mathbf{q}$ is the heat flux per unit area, $p\mathbf{U}$ and $\tau_{ij} \cdot \mathbf{U}$ are the pressure and viscous work terms. If the viscous work term is neglected, through the definition of enthalpy, the conservation of energy equation can be written in terms of temperature, T:

$$\frac{dT}{dt} = K_T \nabla^2 T, \tag{2.8}$$

where K_T is the coefficient of thermal diffusivity. If the density of a fluid is a linear function of temperature, the energy equation (Eq. (2.8)) can be written as a function of density

$$\frac{d\rho}{dt} = K_\rho \nabla^2 \rho, \tag{2.9}$$

where K_ρ is the molecular diffusivity of density replaces K_T as the density can also be affected by changes in salinity (Kundu et al., 2008). $K_\rho \approx K_T$ when the primary stratifying agent is temperature (Thorpe, 2005).

2.1.4 Boussinesq Approximations

In many geophysical settings, a fluid can be considered incompressible. If changes in density due to variations in pressure, salinity and temperature are small, the governing conservation equations can be simplified. If a fluid is assumed incompressible the conservation of mass Eq. (2.3) can be written as

$$\nabla \cdot \mathbf{U} = 0, \tag{2.10}$$

also known as the continuity equation and implies that the velocity field is solenoidal or divergence free.

If the density and pressure terms in the conservation of momentum equation, Eq. (2.6) are replaced by a decomposition into a background and fluctuating term ($\rho(\mathbf{x},t) = \rho_0 + \delta\rho(\mathbf{x},t)$ and $p(\mathbf{x},t) = p_0 + \delta p(\mathbf{x},t)$) the equation becomes

$$\frac{D\mathbf{U}}{Dt} = -\frac{1}{\rho_0}\nabla\delta p + \frac{\delta\rho}{\rho_0}\mathbf{g} + \nu\nabla^2\mathbf{U}, \tag{2.11}$$

where ν is the kinematic viscosity, the background pressure is assumed hydrostatic (i.e. $\nabla p_0 = \rho_0\mathbf{g}$) and density perturbations, δp, are due to changes in salinity or temperature, not due to pressure: the incompressible Navier-Stokes equations. In most geophysical settings $\delta\rho << \rho_0$ which leads to the main emphasis of the Boussinesq approximation that all variations in density can be neglected except when multiplying the gravity term. The resulting term in the equation, $(\delta\rho/\rho_0)\mathbf{g}$, shows that density is an active scalar and is known as the buoyancy term.

Using simplification and decomposition of the density Eq. (2.9) is modified to become the density transport equation:

$$\frac{D\delta\rho}{Dt} = K_\rho\nabla^2\delta\rho. \tag{2.12}$$

This equation is dynamically coupled to the momentum equation and must be solved concurrently. Equations (2.10)-(2.12) represent the Boussinesq set and represent the governing equations most commonly used in most geophysical applications. If the Coriolis force influences a particular flow this term will be added to the momentum equation to account for its impact. The Boussinesq approximations break down if pressure changes are great enough to impact the density of the fluid (i.e. compressible flow) or the hydrostatic pressure is very large. It is important to understand the simplifications and approximation used in the derivation of this set of equations so that they can be applied correctly in the study of geophysical flows.

2.2 Scales of Turbulence

In most areas of fluid dynamics it is common to see the turbulence of fluid flow characterized by the Reynolds number $Re = \mathcal{U}\mathcal{L}/\nu$ where $\mathcal{U}$ is a characteristic velocity scale, $\mathcal{L}$ is a characteristic length scale and ν is kinematic viscosity. The largest eddy diameter defines the characteristic length $\mathcal{L}$ scale constrained by the boundaries of the system. Characteristic velocity is the speed of the largest eddy and is a function of the geometric length scale, $\mathcal{U}(\mathcal{L})$. A time scale can be defined from the ratio of these two quantities $\tau(\mathcal{L}) = \mathcal{L}/\mathcal{U}(\mathcal{L})$, the time it takes the characteristic eddy to complete a single circulation. Time and geometric scales that define climate, oceanic circulations and other geophysical processes are much larger than the scales that define turbulence. The largest eddies in a system transport the majority of momentum and energy within a system. Contained within the characteristic eddy is a range of smaller eddies that dynamically interact until they reach their smallest theoretical size, generally denoted by η, where they can be dissipated by the viscosity of the fluid[1]. In other words the largest circulation is set by the geometry of the system, the smallest is set by the viscosity of the fluid and there is a distribution of intermediate eddy sizes between. Richardson (1922) proposed a framework that describes the transfer of turbulent kinetic energy across these scales and this description still underpins our understanding of the fundamentals of turbulence where turbulent kinetic energy is transferred between the scales by an energy cascade until it reaches a scale small enough for the kinetic energy to be dissipated into internal energy.

Most current descriptions of turbulence in theory are based on a statistical approach and assumptions that the flow is homogeneous, isotropic and stationary. These assumptions can be made to help understand a wide variety of flow phenomena although they are not accurate for all types of flow conditions. The hypotheses of Kolmogorov (1941) rely on classification of high Reynolds

[1]In this dissertation the Greek letter η is used both to denote a turbulent length scale as well as change in the height of the free surface in numerical simulations. Unless otherwise noted assume η denotes the Kolmogorov turbulent length scale.

number flow as stationary (i.e. in statistical equilibrium in time) and the existence of three flow regime ranges; (1) the energy containing range, (2) the inertial subrange where energy is transferred between scales and (3) the dissipation range. The inertial and dissipation range taken together are referred to as the universal equilibrium range and based on his theory turbulence should be statistically isotropic and only depend on the kinetic energy dissipation rate, ϵ, and the the kinematic viscosity, ν. Within the inertial subrange the transfer of energy can be described using solely ϵ. Conversion to internal energy depends only on ν within the dissipation range. Using these two parameters Kolmogorov defined a characteristic length, velocity and time scale of the smallest turbulent eddy, respectively:

$$\eta \equiv (\nu^3/\epsilon)^{1/4}, \tag{2.13}$$

$$u_\eta \equiv (\nu\epsilon)^{1/4}, \tag{2.14}$$

$$\tau_\eta \equiv (\nu/\epsilon)^{1/3}. \tag{2.15}$$

Kolmogorov followed the energy cascade postulation of Richardson (1922) but did not address the mechanisms for energy transfer in the inertial subrange or all of the impacts of the largest energy containing circulations. Exact understanding of the mechanisms that allows energy transfer within the cascade is still unknown. Available energy in the spectrum does scale as a function of η and k (wave number) when the turbulent kinetic energy distribution among the various scale eddies is described in wave number space. The energy density is given by

$$E(k) \sim \epsilon^{2/3} k^{-5/3}, \tag{2.16}$$

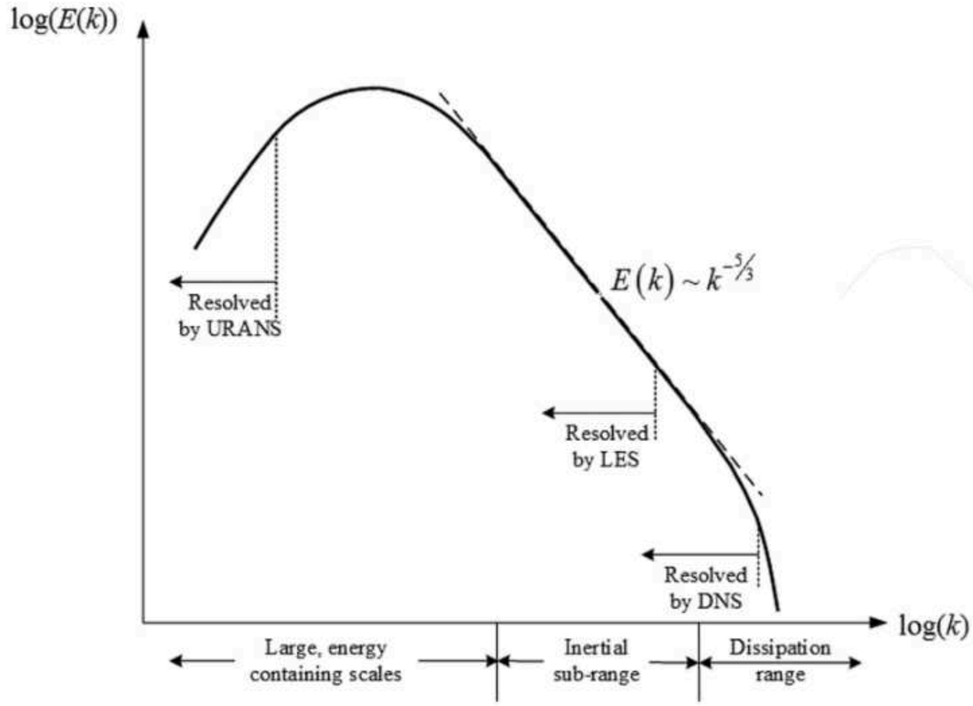

Figure 2.1: Energy spectra plotted as a function of wave number (k) (Thompson et al., 2015).

where the power on the wave number, k, underpins Kolmogorov's famous -5/3 law and is used in assessments of whether or not a flow is turbulent. The energy density contains the high spectra above the inertial subrange bandwidth defined by $k^{-5/3}$ and is low below and so defines the separation between energy production and dissipation. Figure 2.1 shows a plot of the energy cascade.

2.3 Numerical Methods

In turbulent flows eddies are defined by a range of spatial and temporal scales interacting dynamically. The non-linearity of the flow means that a full analytical solution to the Navier-Stokes equations are not possible. Approximate solutions are obtained using numerical methods. Reynolds averaged Navier-Stokes (RANS), large eddy simulations (LES) and direct numerical simulations (DNS) are the three main methods utilized for obtaining a numerical approximation to fluid flow by approximating solutions the Navier-Stokes equations. Each of the methods resolve different temporal and spatial scales of turbulent motion. Each of these methods employ the use of a computational grid. Flow quantities are calculated directly at the grid points or in some cases at an intermediate location between the nodes of the grid. The choice of the computational fluid dynamics (CFD) model from those above is also influenced by the structure and resolution of the computational grid.

2.3.1 Reynolds-Averaged Navier-Stokes (RANS)

A Reynolds decomposition of velocity (U), pressure (p) and density (ρ) are given by Eq. (2.17), Eq. (2.18) and Eq. (2.19), respectively,

$$U(x,t) = \langle U(x,t)\rangle + \mathbf{u}(x,t), \tag{2.17}$$

$$p(x,t) = \langle p(x,t)\rangle + p'(x,t), \tag{2.18}$$

$$\rho(x,t) = \langle \rho(x,t)\rangle + \rho'(x,t). \tag{2.19}$$

Each parameter is "decomposed" into the sum of two components, where $\langle\rangle$ denotes a temporal averaged quantity and $\mathbf{u}$, p' and prime on a quantity (i.e. ρ') gives the turbulent fluctuations of the quantities around the mean. Substitution of these decompositions into Eqs. (2.10)-(2.12) gives the Reynolds-Averaged Navier-Stokes equations (RANS) in summation notation, Eqs. (2.20)-(2.22)

$$\frac{\partial U_i}{\partial x_i} = 0, \tag{2.20}$$

$$\frac{D\langle U_i\rangle}{Dt} = -\frac{1}{\rho_0}\frac{\partial\langle\rho\rangle}{\partial x_i} - \frac{\langle\rho\rangle}{\rho_0}g\delta_{i3} + \frac{\partial}{\partial x_j}\left[\nu\frac{\partial\langle U_i\rangle}{\partial x_j} - \langle u_i u_j\rangle\right], \tag{2.21}$$

$$\frac{D\langle\rho\rangle}{Dt} = \frac{\partial}{\partial x_j}\left[\kappa\frac{\partial\langle\rho\rangle}{\partial x_j} - \langle\rho' u_j\rangle\right], \tag{2.22}$$

where the indices i and j are used to denote the directional components using summation notation and δ_{i3} is the Kroenecker delta function ($\delta_{ij} = 1$ if $i = j$ and $\delta_{ij} = 0$ if $i \neq j$). RANS equations are analogous to Eqs. (2.10)-(2.12) except that they include the additional turbulent fluctuation terms. These components of the equation are termed the Reynolds stress tensor $-\langle u_i u_j \rangle$ and turbulent density flux $-\langle u_j \rho' \rangle$ in Eq. (2.21) and Eq. (2.22), respectively. These terms can be thought of as the stress on the mean flow from the turbulent transfer of momentum. These terms also represent additional unknowns in this formulation of the Navier-Stokes and create what is known as the turbulence closure problem where there are more unknowns than there are available equations. For the large majority of engineering applications detailed information about turbulent fluctuations of the flow are not needed and information about time-averaged properties is sufficient. A turbulence model is needed to parameterize the fluctuating terms when solving turbulent flow using RANS simulations. Common RANS turbulence models apply a set of transport equations that are solved in addition to the flow equations. Application of the turbulent-viscosity and gradient diffusion hypotheses describe the turbulent transport terms in an analogous manner to molecular transport and provides additional equations that reduce the nine additional unknown terms in the Reynolds stress tensor and the scalar flux vector, resulting in two equations

$$-\langle u_i u_j \rangle = K_m \left(\frac{\partial \langle U_i \rangle}{dx_j} + \frac{\partial \langle U_j \rangle}{dx_i} \right) - \frac{1}{3} \langle u_i u_j \rangle \delta_{ij}, \tag{2.23}$$

$$\langle u_j \rho' \rangle = K_d \frac{\partial \langle \rho \rangle}{\partial x_j}, \tag{2.24}$$

where K_m is the turbulent (eddy) viscosity and K_d is the turbulent diffusivity of density. In order to close the system of equations these two terms must be prescribed. This creates a simple way to obtain a solution to the RANS equations but it is important to note that both K_m and K_d are flow, not fluid properties like kinematic viscosity and molecular diffusion, and therefore can be directionally dependent.

2.3.2 Large Eddy Simulations (LES)

In most cases small turbulent eddies tend to be isotropic and behave similarly to the other small eddies in a given flow. Large eddies are more likely to be anisotropic and can be greatly influenced by flow direction. They also extract energy from the mean flow and can conform to the geometry/bathymetry of the region surrounding the flow being anlayzed. Application of the RANS equations necessitates the condition that all eddies are described by the same turbulence model. A large eddy simulation (LES) simulation calculates, and directly resolves, the large anisotropic eddies using a time-dependent simulation. A simple model is used for the anisotropic eddies that are smaller than the computational grid (subgrid-scale, or SGS, turbulence closure model) and can not be resolved as a result. Spatial filtering is used to sort the eddies at a pre-determined threshold resolving the unsteady computations of the flow field above that threshold. LES modeling has resulted from concerted efforts to develop a general model applicable to a variety of practical applications (Malalasekera & Versteeg, 2007) and is generally considered the middle ground between RANS based CFD models (Section 2.3.1) and direct numerical simulations (DNS), discussed in the following Section (Section 2.3.3). As available computational power and resources have increased the use of LES CFD models have also become more prevalent, and will likely become a more viable option for general CFD modeling in the near future.

2.3.3 Direct Numerical Simulations (DNS)

Direct numerical simulations, or DNS, give instantaneous and time-resolved solutions to the unsteady Navier-Stokes equations, Eqs. (2.10)-(2.12), including the mean flow and the turbulent velocity fluctuations. The computational grid must have sufficiently fine resolution in order to capture the smallest turbulent eddies at the Kolmogorov scale η. Additionally the time steps used in the DNS must be smaller than the period of the fastest fluctuations in the flow field. Instantaneous observations of the flow field can be generated by DNS that are not observable or measurable in the field or laboratory setting making them a very useful and powerful tool for understanding turbulent flow (Malalasekera & Versteeg, 2007). Turbulent transport and energy budgets can be accurately calculated from DNS results and can be useful to compare to estimated budgets from the field and laboratory experiments.

The computational costs associated with DNS simulations are extremely high and see more limited application than LES or RANS. Resolving the full range of length and time scales present in a turbulent flow creates limitations based on the currently available computational resources. As discussed in Section 2.2 the Reynolds number is a commonly used to define the level of turbulence in a flow. If the largest eddy in a flow is defined by l than $l/\eta \approx Re^{3/4}$. If a DNS is three-dimensional then $l/\eta \approx Re^{9/4} \approx N$, where N is the number of grid points. This scaling shows that an increased Reynolds number leads to an increase the number of grid points needed for a DNS controlled by the power $9/4$. As a result DNS is generally limited to moderately turbulent flows. Pseudo-spectral methods, hyper viscosities and low wave number forcing are all methods that can be used in DNS to increase the Reynolds number of the flow. DNS presented in Chapter 4 and Chapter 5 apply pseudo-spectral methods in order to decrease the number of computations needed to resolve the flow. Using this method the velocity field $u(x,t)$ is represented by a fast Fourier series $u(x,t) = \Sigma e^{ik,x}\hat{u}(x,t)$, where k is the wave number in N^3 wave number space.[2] This can then be used to determine the maximum possible Reynolds number for a simulation give the limits of the available computational resources by application of $N \sim 1.6Re^{3/4}$ scaling (Pope, 2000). N^6 computational operations are reduced to $N^3 logN$ operations by solving the linear terms in the Navier-Stokes equations in wave space and the non-linear terms in physical space using this method.

[2]In the fast Fourier series equation k denotes the wave number. Elsewhere it has been used to denote the turbulent kinetic energy. Hereafter assume that the symbol k denotes the turbulent kinetic energy unless specifically noted to signify a different quantity.

Chapter 3

Literature Review

3.1 Stratified Flow & Internal Waves

When in referenced in the context of the atmospheric or oceanic setting, the term “stratified fluid" is generally referring to a body of fluid that is layered by variations in density. The density variation can be continuous, isolated at discontinuous interfaces, or a combination of both. Under most conditions the density generally varies in reference to a vertical position from a bottom boundary at $z = 0$. The equation of state for density variation from a reference density ρ_0 in the oceanic context as a function of changes in temperature T and salinity S is given by

$$\rho = \rho_0(1 - \alpha T + \beta S), \tag{3.1}$$

where coefficients α and β are the coefficients of thermal expansion and contraction of salinity, respectively (Thorpe, 2005).

When a fluid parcel of certain density is displaced into a region of a higher density in a continuously stratified fluid, there is a resulting buoyancy force that works to establish an equilibrium. This unforced movement and transfer of momentum resulting from the buoyancy force can result in the parcel passing its equilibrium position and lead to an oscillation at a specific frequency, referred to as the buoyancy or Brunt-Väisälä frequency, N.

$$N = \sqrt{-\frac{g}{\rho_0}\frac{d\bar{\rho}}{dz}}, \tag{3.2}$$

where g is gravitational acceleration and $d\bar{\rho}/dz$ is the background mean density gradient. If $N^2 > 0$, the fluid is stably stratified as a result of lighter fluid overlying denser fluid (i.e. $d\bar{\rho}/dz < 0$).

When $N^2 < 0$, the fluid is considered unstably stratified and subject to convective motion and turbulent mixing as a result of a light fluid plume rising through denser fluid (i.e. $d\bar{\rho}/dz$>0). In the case where $N^2 = 0$ the fluid is considered to be neutrally stratified. Motions result in the generation of a field of internal waves when the perturbations are less than the background frequency. Internal waves propagate in any direction within a continuously stratified flow.

The relation shown in Eq. (3.3) is the range of possible internal wave frequencies ω

$$f < \omega < N, \tag{3.3}$$

where f denotes the inertial or Coriolis frequency of rotation and is a result of the rotating motion of the earth. Internal waves in the range near to f are referred to as inertial gravity waves and are strongly influenced by the earth's rotation. In the oceanic or atmospheric setting, wave period of internal waves $(2\pi/\omega)$ vary between minutes and hours depending on the location and the degree of stratification where it is assumed that $N > f$, which is the case for the majority of the atmosphere and ocean (Kundu et al., 2008).

Equation (3.4) shows the linearized non-hydrostatic Boussinesq equations solved for the vertical velocity w as a partial differential equation (Thorpe, 2005; Kundu et al., 2008)

$$\frac{\partial^2}{\partial t^2}\nabla^2 w + N^2\nabla_H^2 w + f^2\frac{\partial^2 w}{\partial z^2} = 0, \tag{3.4}$$

where ∇^2, Eq. (3.5), is the Laplacian operator and ∇_H^2 in Eq. (3.4) denotes the horizontal Laplacian operator.

$$\nabla^2 = \frac{\partial^2}{\partial x^2} + \frac{\partial^2}{\partial y^2} + \frac{\partial^2}{\partial z^2}. \tag{3.5}$$

Assuming a wavelike solution to Eq. (3.4) for the vertical velocity as follows:

$$w(x, y, z) = W(z)e^{i(kx+ly-\omega t)}, \tag{3.6}$$

results in an ordinary differential equation in terms of W, Eq. (3.7). Solutions to Eq. (3.7) become exponential in z when $\frac{N^2-\omega^2}{\omega^2-f^2} < 0$ and are trapped by the surface of the fluid and represent surface waves propagating in the horizontal plane. When $\frac{N^2-\omega^2}{\omega^2-f^2} > 0$, the solutions to the ordinary differential equation are trigonometric in the z direction and results in waves propagating in three dimensions (Kundu et al., 2008)

$$\frac{d^2W}{dz^2} + \left(\frac{N^2 - \omega^2}{\omega^2 - f^2}\right)(k^2 + l^2)W = 0. \tag{3.7}$$

Deduction of the dispersion relation, Eq. (3.8), comes from the simplification of Eq. (3.7),

$$\omega = \left(f^2 sin^2\theta + N^2 cos^2\theta\right)^{1/2}. \tag{3.8}$$

If the Coriolis rotation of the earth is neglected the dispersion relation reduces to Eq. (3.9)

$$\omega = N cos\theta = N sin\beta, \tag{3.9}$$

where θ denotes the angle between the horizontal and the phase velocity defined as $\mathbf{c_p} = \omega/\mathbf{k}$. This quantity also denotes the wavenumber vector. Here β denotes the angle between the horizontal direction and the wave group velocity, $\mathbf{c_g} = \nabla_\mathbf{k}\omega$ (Lighthill & Lighthill, 2001). The phase and group velocity vectors are by definition perpendicular to each other where energy of an internal wave propagates in the direction and speed of the group velocity, as shown in Figure 3.1.

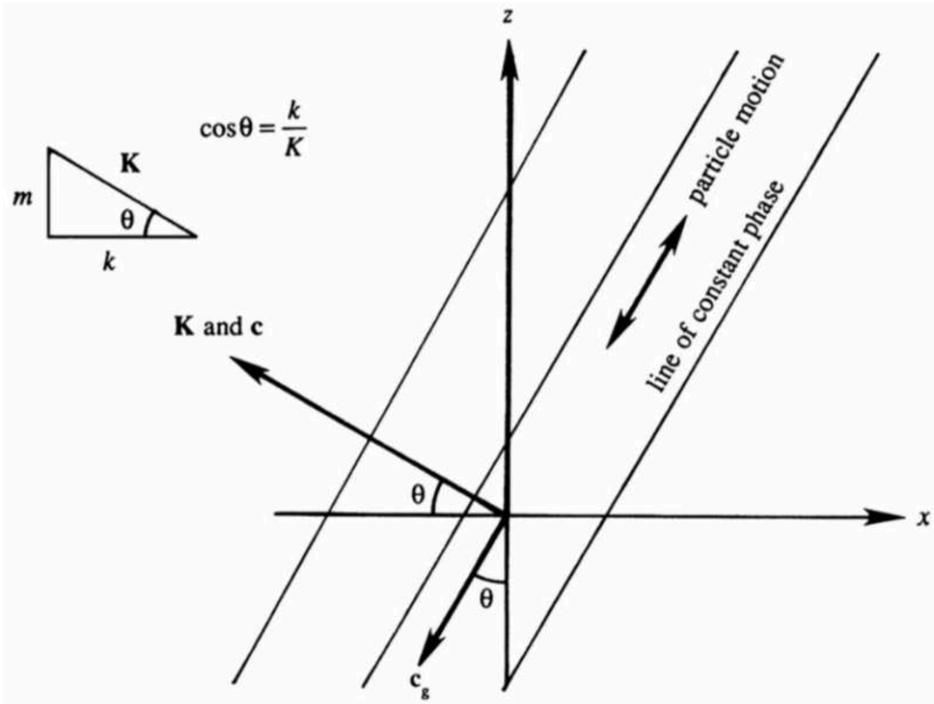

Figure 3.1: Illustration from Kundu et al. (2008) showing the propagation angles of internal waves where $\mathbf{K} = (k, l, m)$ is the wave number vector.

Energy from the source follows lines of constant phase and particles move perpendicular to the wavenumber vector.

When a propagating internal wave interacts with a boundary, it will reflect following a unique set of laws. In acoustics and optics, the classic theory of Snell's Law shows that the angle of the incident wave to the normal direction of the reflecting surface is preserved. In the case of internal wave reflection, the angle with respect to the gravity vector is preserved (Thorpe & Umlauf, 2002; Phillips, 1977). Enhanced boundary layer mixing occurs when the angle β is equivalent to the angle of the topographic bottom slope boundary, α. Classification of a critical slope in the case of internal wave boundary interaction depends both on the slope of the boundary and the angle of the group velocity vector to the horizontal. Topographic bottom slopes with $\alpha > \beta$ are considered subcritical, “transmissive" slopes where the wave energy is forward reflected. In cases where $\alpha < \beta$, internal waves reflect back with beams in both the upward and downward direction and

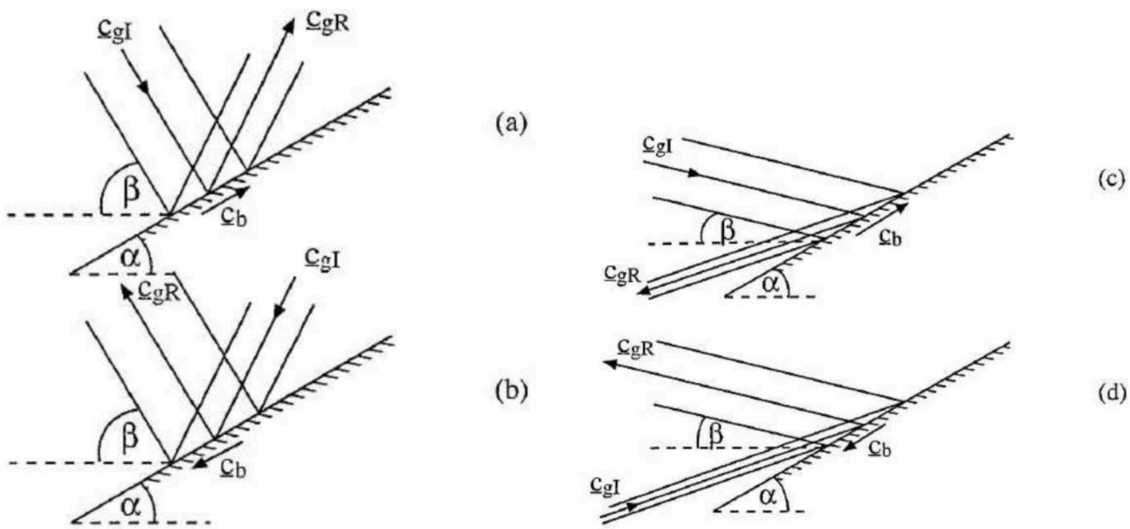

Figure 3.2: Illustration depicting the “transmissive", (a) & (b), and “reflective", (c) & (d) cases of internal wave interaction with a rigid topographic boundary based on the characteristic angles α and β (Thorpe & Umlauf, 2002). $\mathbf{c_{gI}}$ and $\mathbf{c_{gR}}$ are the group velocities of the waves incident and reflective from the slope, respectively.

is considered the “reflective case" (Venayagamoorthy, 2006). Different cases illustrating internal wave angle reflections relative to the bottom slope angle are shown in Figure 3.2.

3.1.1 Scales of Stratified Turbulence

Various length scales can be defined for stably stratified geophysical flows that incorporate the effects of buoyancy. The buoyancy length scale gives a measure of the maximum possible displacement for a given N at which all kinetic energy is converted to potential energy against the stratification. This length scale is defined by

$$L_b = \frac{\left(\langle w'^2 \rangle\right)^{1/2}}{N}, \tag{3.10}$$

where w' is the vertical velocity fluctuation. At a smaller scale Ozmidov (1965) defined a length scale, L_O, to represent the largest vertical isotropic scale of motion in a stratified flow where buoyancy influences turbulence,

$$L_O = \left(\frac{\epsilon}{N^3}\right)^{1/2}. \tag{3.11}$$

The turbulent vertical motions defined by buoyancy and Ozmidov length scales are often associated with turbulent overturning motion. The Ellison length scale is also used to define the size of turbulent overturning motions in stratified flow and is defined as

$$L_E = \frac{\langle \rho'^2 \rangle^{1/2}}{\partial \langle \rho \rangle / \partial z}, \tag{3.12}$$

where $\partial \langle \rho \rangle / \partial z$ is the mean background density gradient and $\langle \rho'^2 \rangle^{1/2}$ is the root-mean-square density fluctuation (Ellison, 1957). The lengths of the overturns can be derived from measured density profiles and the resorting method proposed originally by Thorpe (1977) where if an overturn exists an instantaneous density profile will not be in equilibrium when compared to the background density profile. Thorpe sorting takes the instantaneous profile and re-sorts it in ascending order restoring a gravitationally stable profile that is then used to determine magnitudes of vertical displacements δ_T. If an overturn is detected in a measurement the Thorpe scale is calculated by

$$L_T = \langle \delta_T^2 \rangle^{1/2}, \tag{3.13}$$

where $\langle \delta_T^2 \rangle^{1/2}$ is the root-mean-square displacement. The Thorpe and Ellison length scales are considered equivalent in linearly stratified fluid (Smyth & Moum, 2000) but it has been noted that the Thorpe length scale may have a time dependence and so may not be equivalent in measurements with insufficient time resolution (Cimatoribus et al., 2014).

3.2 Physical Measurement

Understanding the turbulence and dynamics of oceanic flows requires physical measurement. The complexity, size and transience of the three-dimensional structures that are inherent to oceanic turbulence create significant barriers to flow measurements being resolved in either time and/or space. Grant et al. (1962) first made direct measurement of oceanic turbulence using hot film anemometry in 1950. Free falling profilers have become popular since their introduction in the 1960's as a result of not being influenced by a ship or buoy motion (Lueck et al., 2002). Measurements made by instruments connected by a cable to ship or buoy can be influenced both by surface wave motion as well by the vibrations created by the connective cable (Lueck et al., 2002). Widely used instruments for oceanic measurements include the acoustic Doppler current profiler (ADCP), the conductivity-temperature-depth (CTD) probe and the vertical microstructure profiler (VMP). Each instrument is designed to create a stable platform that contains the necessary measurement probes, and circuits to supply power to the instrumentation as well as collect and store the signal from the probe. The VMP is typically employed as a free falling instrument while the ADCP and the CTD are typically mounted to a ship, buoy or sea floor. Examples of each type of these instruments is shown in Fig. 3.3.

3.2.1 Acoustic Doppler Current Profiler (ADCP)

The ADCP is used to measure the velocity field using between 4 and 5 acoustic transducers and the Doppler shift principle. Transducers on the probe emit an acoustic frequency in multiple directions in order to measure the different components of the velocity field simultaneously. The emitted acoustic 'pings' of sound are emitted at a constant frequency and bounce off of particles suspended in the water column, which are reflected back to and measured by the instrument. Sound waves returning to the instrument have a different frequency as a result of the Doppler shift. If the acoustic wave emitted by the ADCP is reflected by a particle traveling toward the instrument the returning frequency will be higher than the emitted frequency. Conversely, if the the emitted sound wave is reflected from a particle traveling away from the instrument the returning frequency will

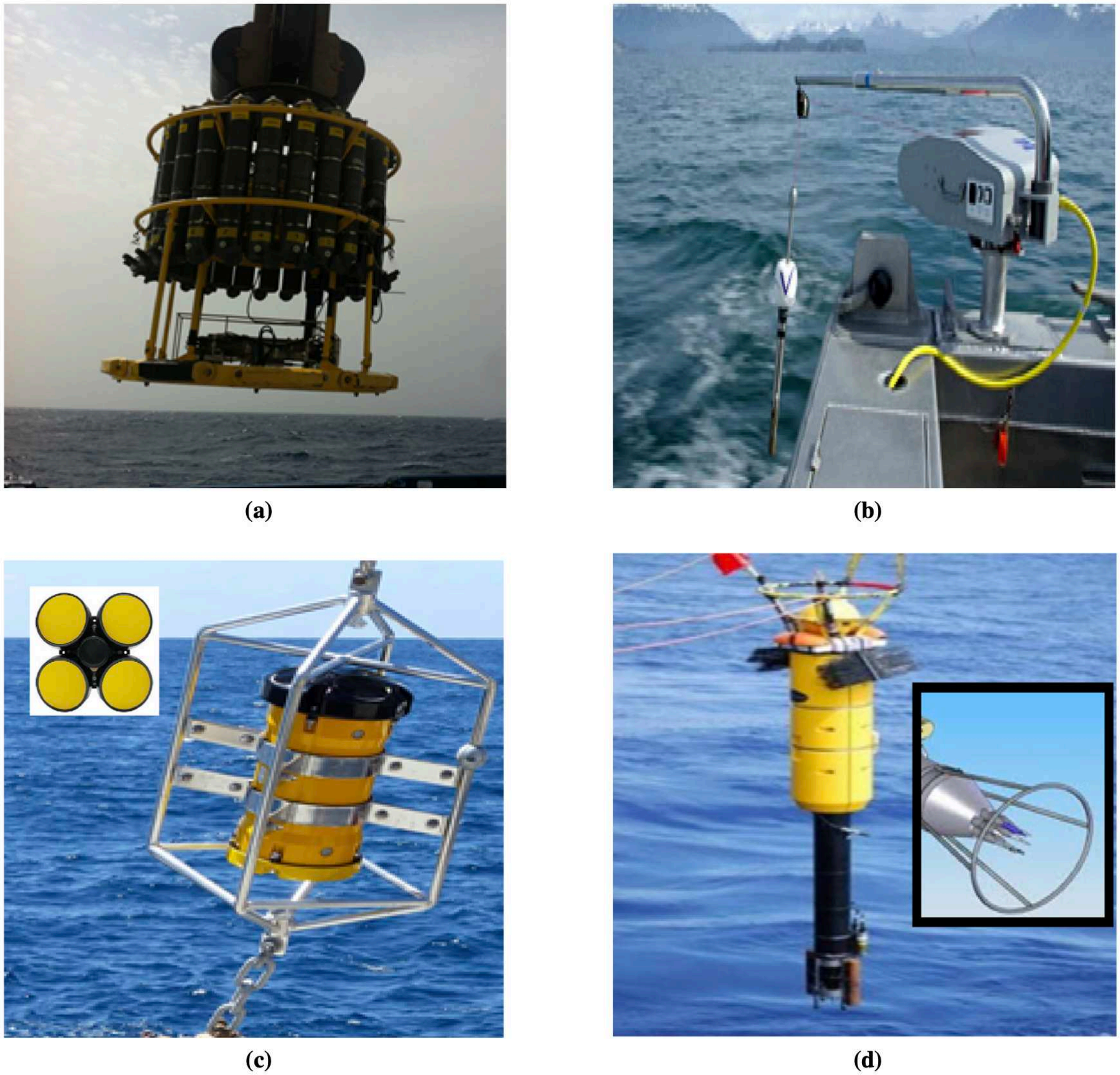

Figure 3.3: Images of commonly used oceanic measurement instrumentation (Garanaik, 2018). (a): CDT rosette, (b): UCTD, (c): ADCP and (d): VMP

be lower than the emitted frequency. The difference in frequency between the two acoustic waves is called the Doppler shift and can be used to determine the velocity of particles in the water column. By proxy the velocity of the water column can be determined from the calculated particle velocities. In the oceanic setting the ADCP is primarily used to measure the horizontal velocities and can collect data at rates between 50 and 200 Hz. ADCPs are typically mounted instruments, attached to a ship or the seafloor up to 1000 m in depth.

3.2.2 Conductivity-Temperature-Depth (CTD) Probes

This instrument is primarily used to measure chemical, physical and biological properties in oceanography. Examples of quantities measured by a CDT probe most commonly include, but are not limited to, temperature, pressure, salinity, pH and dissolved oxygen. CTD probes are typically deployed by being lowered from a stationary ship up to the maximum desirable depth (up to multiple thousands of meters) and then pulled up through the water column collecting samples at specified intervals using the samplers displayed in Fig. 3.3a, known as the sampling rosette. The UCDT (underway CDT) shown in Fig. 3.3b is an instrument that is used to measure temperature, pressure, and salinity from ships moving up to 13 nautical miles per hour. As a result of making measurements from a ship that is underway this instrument typically is used to make measurements only a few hundred meters from the surface of the ocean (Rudnick & Klinke, 2007). Measurement of the temperature, salinity and pressure are needed for understanding and quantification of stratified turbulence and determination of the stratification.

3.2.3 Vertical Microstructure Profiler (VMP)

The VMP instrument is deployed unattached to a ship or mooring. When the instrument is released it falls under its own weight through the water column to a predefined depth collecting measurements of shear, temperature and other CTD quantities using high resolution sensors. When the instrument reaches the predefined depth of measurement it releases ballast weight in order to become positively buoyant and return to the ocean's surface for retrieval. The high-resolution, state-of-art sensors on this instrument allow for the concurrent measurement of turbulence and hydrographic data. VMPs are much more expensive than a normal CDT probes or ADCPs but allow collection of concurrent hydrographic and turbulence data and more direct estimation of oceanic states of turbulence when compared to quantities derived from measurements made by the other instrumentation. Even though this instrument is able to collect shear data it typically can only measure one or two components in the three-dimensional field. As a result an assumption of isotropic turbulence is typically made, where the dissipation rate of turbulent kinetic energy, ϵ, and thermal dissipation, χ, are considered equivalent in all three coordinate directions. As will be discussed in Chapter 4 and Chapter 5 in stratified flow this assumption has an impact on our understanding of oceanic turbulence.

Due to the difficulty and operational risk measurements in the deepest part of the ocean and near to boundaries are extremely limited. The majority of oceanic turbulence measurements estimate a value for the vertical eddy diffusivity of $10^{-5}\ m\ s^{-2}$ (Gregg, 1989). This value is an order of magnitude less than the canonical value that has been estimated for the vertical eddy diffusivity needed in order to maintain global thermohaline circulation (Munk, 1966). Microstructure measurements from below $1000\ m$ depth show a global average diffusivity on the order of $10^{-4}\ m\ s^{-2}$ (Waterhouse et al., 2014). These field measurements combined with CFD simulations of stratified flow and careful consideration of the governing physics are needed to further understand these processes due to the limitations of physical measurement and observation.

3.3 Dimensionless Parameters

Use of dimensionless parameters is common in the analysis of fluid mechanics problems (Tennekes et al., 1972; Pope, 2000). They allow for the comparison of different scales of flow as well as translation between physical, computational and theoretical studies of turbulence. The following parameters provide useful tools for analyzing stratified turbulence (Brethouwer, Billant, Lindborg, & Chomaz, 2007). Many of these parameters can be defined in more than one way. The definitions presented here are either the most accepted/common definitions in the field or are definitions that are used within a specific context where the working definition is illustrative of a certain concept or physical phenomena.

3.3.1 Reynolds Number

The Reynolds number is perhaps the most widely used dimensionless parameter in fluid mechanics. It is commonly applied as a proxy for the degree of turbulence. By the definition the Reynolds number expresses a ratio of inertial forces to viscous forces

$$Re = \frac{UL}{\nu}, \tag{3.14}$$

where U is the characteristic velocity scale, L is the characteristic length scale and ν is the kinematic viscosity of the fluid. When $Re >> 1$, the fluid's motion is not affected by its viscosity and the inertia creates turbulence that is triggered via hydrodynamic instabilities. The larger the value for the Reynolds number the higher the degree of turbulence. The Reynolds number is also used when analyzing wake dynamics and boundary layer separations (Pope, 2000; Spedding et al., 1996).

3.3.2 Turbulent Reynolds number

A ratio measure of the turbulent viscosity to molecular viscosity is given by the turbulent Reynolds number

$$Re_t = \frac{k^2}{\epsilon\nu} = \nu_t\frac{1}{\nu}, \tag{3.15}$$

where k is the turbulent kinetic energy, ϵ is the rate of dissipation of turbulent kinetic energy. The ratio of k^2 to ϵ scales as the turbulent viscosity ν_t. This dimensionless parameter is particularly useful as one tool in analysis of the degree of turbulence in computational simulations and turbulent mixing studies.

3.3.3 Froude number

Non-dimensional steepness of an internal wave can be defined by a Froude number,

$$Fr = \frac{U_0}{C_{ph}}, \tag{3.16}$$

where U_0 is the maximum velocity amplitude and C_{ph} is the linear first-mode internal wave celerity in a stratified fluid. This is an important non-dimensional parameter for characterizing an incoming internal wave in numerical simulations as defined by Kundu et al. (2008).

3.3.4 Vertical Froude number

Rather then a strict ratio of inertial to gravitational forces given by the normally defined Froude number, the vertical Froude number defined by Equation 3.17 (Aguilar et al., 2006) is a measure of the inertial and buoyancy forces in the case of stratified flow interacting with topography

$$Fr_v = \frac{U}{Nh}, \tag{3.17}$$

where U is the fluid velocity, h is the maximum height of the topography and N is the buoyancy frequency. If $Fr_v << 1$ the effects of stratification impact the non-linear turbulence. This ratio has been called different names by a variety of authors, such as "Long's number" by Aguilar & Sutherland (2006), but most definitions preserve the same defining ratio.

3.3.5 Horizontal Froude number

Also defined by Aguilar et al. (2006), the horizontal Froude number incorporates the horizontal extent of the along-stream length of the topographic obstacle, A. When $Fr_h < 1$, the vertically propagating internal waves are created along the face of the topography and can be an important parameter for evaluation of stratified flow interaction with three-dimensional obstacles.

$$Fr_h = \frac{U}{NA}. \tag{3.18}$$

3.3.6 Turbulent Froude number

In stratified flows the turbulent Froude number is a ratio of buoyancy effects to turbulence effects. The definition of this parameter also introduces the definition of turbulent time scale ($T_L = k/\epsilon$), which is a timescale measure of the largest isotropic, or turbulent, eddy (Pope, 2000). Depending on the order of magnitude of this number, it can be used to evaluate the degree stratification is inhibiting turbulence.

$$Fr_t = \frac{\epsilon}{Nk} = \frac{1}{NT_L}. \tag{3.19}$$

3.3.7 Turbulent Rossby number

All internal waves are in the frequency spectrum between the Coriolis frequency f and the buoyancy frequency N. The turbulent Rossby number is a ratio of the rotational effects, as compared to the buoyancy effects in the turbulent Froude number, to turbulent effects. This dimensionless parameter is used to evaluate the effects of rotation on turbulence

$$Ro_t = \frac{\epsilon}{fk} = \frac{1}{fT_L}, \tag{3.20}$$

and similarly to Eq. (3.19) it can be defined in terms of the turbulent time scale T_L, as shown in Eq. (3.20).

3.3.8 Mixing Efficiency

When considering mixing a stratified flow, the mixing efficiency can be defined (Ivey & Imberger, 1991) by the flux Richardson number given by

$$R_f = B/(B + \epsilon), \tag{3.21}$$

where B is the buoyancy flux ($B = g/\rho_0(\rho' w')$, ρ' is the density fluctuation and w' is the fluctuations in the vertical velocity). $B + \epsilon$ gives the net mechanical energy that is required to sustain the motion of turbulence and includes the turbulent kinetic energy coming from production, advection and transport. By this definition it is not possible to separate the flux due to wave action (reversible mixing) and the flux that results only due to turbulent motions (irreversible mixing). In order to define the local rate of the irreversible transfer of kinetic energy and density, the flux Richardson number is defined as

$$R_f = \frac{\epsilon_{PE}}{\epsilon_{PE} + \epsilon}, \tag{3.22}$$

where ϵ_{PE} is the rate of dissipation of turbulent potential energy. From the definition presented in Equation 3.22, the irreversible mixing coefficient (Γ) is defined and is also used as a measure of irreversible energy loss,

$$\Gamma = \frac{\epsilon_{PE}}{\epsilon}. \tag{3.23}$$

3.3.9 Buoyancy Reynolds number

The buoyancy Reynolds number, Eq. (3.24), is commonly used for the evaluation of the mixing efficiency (and by proxy turbulence) from field data. As discussed in Mater & Venayagamoorthy

(2014a), it has the advantage of being explicitly defined, as compared to the gradient Richardson number, as a measure of mixing efficiency

$$Re_B = \frac{\epsilon}{\nu N^2}, \tag{3.24}$$

where the equation gives the ratio of kinetic energy dissipation to buoyancy force. It should be noted that Re_B is an ambiguous parameter in that for a given value of the buoyancy Reynolds, the mixing efficiency can vary by an order of magnitude (Mater & Venayagamoorthy, 2014a). However, using the buoyancy Reynolds number is a useful, but not unique, diagnostic tool for evaluating mixing efficiency and turbulence in stratified flows.

3.3.10 Diffusivity Ratio

The ratio of turbulent diffusivity to molecular diffusivity, Eq. (5.4), can be used to evaluate the degree of turbulence, particularly in DNS simulations, and is defined by

$$\hat{\kappa} = \frac{K_\rho}{\kappa} = \frac{\epsilon_{PE}}{N^2 \kappa}, \tag{3.25}$$

where rate of potential energy dissipation is denoted as ϵ_{PE}, molecular diffusivity by κ and turbulent diffusivity by K_ρ. If $\hat{\kappa} < O(10)$, then there is not a sufficient separation of scales in the flow and it is therefore likely that mixing is dominated by molecular effects.

3.3.11 Topographic steepness parameter

Steepness of the bottom topography is classified as “critical" ($\epsilon = 1$), “supercritical" ($\epsilon > 1$) or “subcritical" ($\epsilon < 1$) by Phillips (1977) using the topographic steepness parameter ϵ defined as

$$\epsilon = \frac{\gamma}{s}, \tag{3.26}$$

where topographic slope is denoted by γ and the slope of the internal wave beam, s, is given by

$$s = tan\alpha = \frac{k}{m} = \left(\frac{\omega^2 - f^2}{N^2 - \omega^2}\right), \tag{3.27}$$

where the definition of the angle between the internal wave characteristic and the horizontal plane is denoted by α, and k and m are the horizontal and vertical wave-numbers respectively. The topographic steepness parameter is a fundamental parameter to the study of wave-topography interaction (Venayagamoorthy, 2006) and the generation of internal tides (Klymak et al., 2012).

3.3.12 Tidal excursion parameter

The tidal excursion parameter defines the difference between the “internal tide" regime and the “quasi-steady" lee wave regime

$$Ex = \frac{U_0 \kappa}{\omega}, \tag{3.28}$$

where U_0 is the amplitude of the barotropic tidal current and ω is the frequency (St. Laurent & Garrett, 2002). Differences between these two regimes based on observed timescales has been proposed by Dohan (2004). “Internal tides" regimes are considered dominant when Ex is less than 1 and tidal excursion scale is less than the topographic scale. When the tidal excursion scale is greater than that of the topography and Ex is greater than 1, the stratified flow is considered to be a “quasi-steady lee wave".

3.4 Continuously Stratified Flow Past Topography

Stratified flow past topography gives rise to a variety of turbulent and flow phenomena. These phenomena have been studied using field scale observations (e.g. Munk & Wunsch, 1998; Vosper et al., 1999; Jarosz et al., 2014; Wijesekera et al., 2014), numerical simulations (e.g. Suzuki & Kuwahara, 1992; Di Lorenzo et al., 2006; Winters & Armi, 2012) as well as theoretical and mathematical analyses (e.g. Drazin, 1961; Smith, 1988; Voisin, 1991). There are a variety of different flow patterns, the most common of which have been studied and classified. The following section describe a brief history of early observational and theoretical analyses. Brief descriptions of important flow phenomena and a summary of recent research is also presented.

3.4.1 Observational/analysis history

As early as the 1940s, analytical studies, using linear theory, have shown that obstacles interacting with a continuously stratified fluid create small amplitude disturbances (Lyra, 1943; Queney, 1947). Observations of topographically trapped lee-waves were made by Scorer (1949) and applications of linear theory have shown consistent results (Vosper et al., 1999; Smith et al., 2002) when analyzing these types of phenomena. Seminal work by Long (1953) showed an extension of linear theory to the non-linear flow fields that arise under certain conditions. This research created a breakthrough in understanding and analysis of these flows. Field observations have shown that the vertical mixing resulting from breaking internal waves near the ocean boundaries can explain vertical advection-diffusion balances (Munk & Wunsch, 1998; Thorpe, 2004). The transfer of turbulent energy from these locations near the boundary to the ocean interior help explain mixing processes measured far from boundaries and close global energy budgets. Baines (1998) provides the most comprehensive early review of stratified flow past obstacles but others have provided other reviews of stably stratified flow past obstacles (e.g. Long, 1972; Smith, 1979, 1989; Baines, 1987).

3.4.2 Experimental background

Cacchione & Wunsch (1974) used laboratory experiments of stratified first-mode waves shoaling to show that at critical slope angles, shear generated instabilities generate periodic vortices that mix the local fluid. This mixed fluid flows along isopycnals to mix the interior of the fluid. An extension of this work by Ivey & Nokes (1989) quantified the efficiency of the mixing observed in these processes. Here the mixing efficiency is defined as the ratio of the increase in potential energy to the loss of kinetic energy due to the mixing created by incident waves. An upper bound of 0.2 for the mixing efficiency was proposed and has seen widespread use as a result. Laboratory work by Dauxois et al. (2004) was conducted in order to generate more clearly defined incident wave beams interacting with a sloping boundary. The authors used plunging cylinders made of polyvinyl chloride (PVC) to generate planar, parallel wave patterns that were studied using classical Schlieren imaging techniques. Time series images in Figure 3.4 show a wave front propagating up a supercritical slope ($\gamma/s = 1.28$) where the isopycnal surface lines concentrate, collapse and overturn leading to mixing of density.

3.4.3 Wave instability & breaking

Instabilities leading to the breaking of internal waves due to interaction with topography transfers energy to higher wave numbers. This leads to turbulent mixing near the boundary. St. Laurent & Garrett (2002) have estimated that up to 30% of the energy can be dissipated near the boundary while the remaining energy radiates in the form of low-mode internal waves that interact with other internal waves or other topographic boundaries remote from the initial source (Polzin et al., 1997). An in depth discussion of this process based on topographic characteristics, density stratification and the tidal forcing is presented by Polzin (2009). Nikurashin & Legg (2011) and Nikurashin & Ferrari (2013) have simulated these processes using numerical modeling. Static and dynamic instabilities are the two most likely causes of internal wave breaking (Thorpe, 2005) and the type of instability impacts the mixing efficiency (Linden & Redondo, 1991). A static instability is also referred to as a convective instability where generally heavier, more dense fluid, overlies light, less dense, fluid leading to overturning motions. A static instability can occur when $N^2 < 0$ or the ratio of the local fluid velocity U to the wave speed c is greater than 1. Dynamic instabilities are also known as shear instabilities, a classic example is the formation of Kelvin-Helmholtz billows, when the fluid velocity overcomes damping effects of the density stratification as shown in Figure 3.5. This type of instability is common in atmospheric shear layers and the oceanic thermocline and is an important factor in internal wave mixing (Smyth & Moum, 2012). As shown in Venayag-

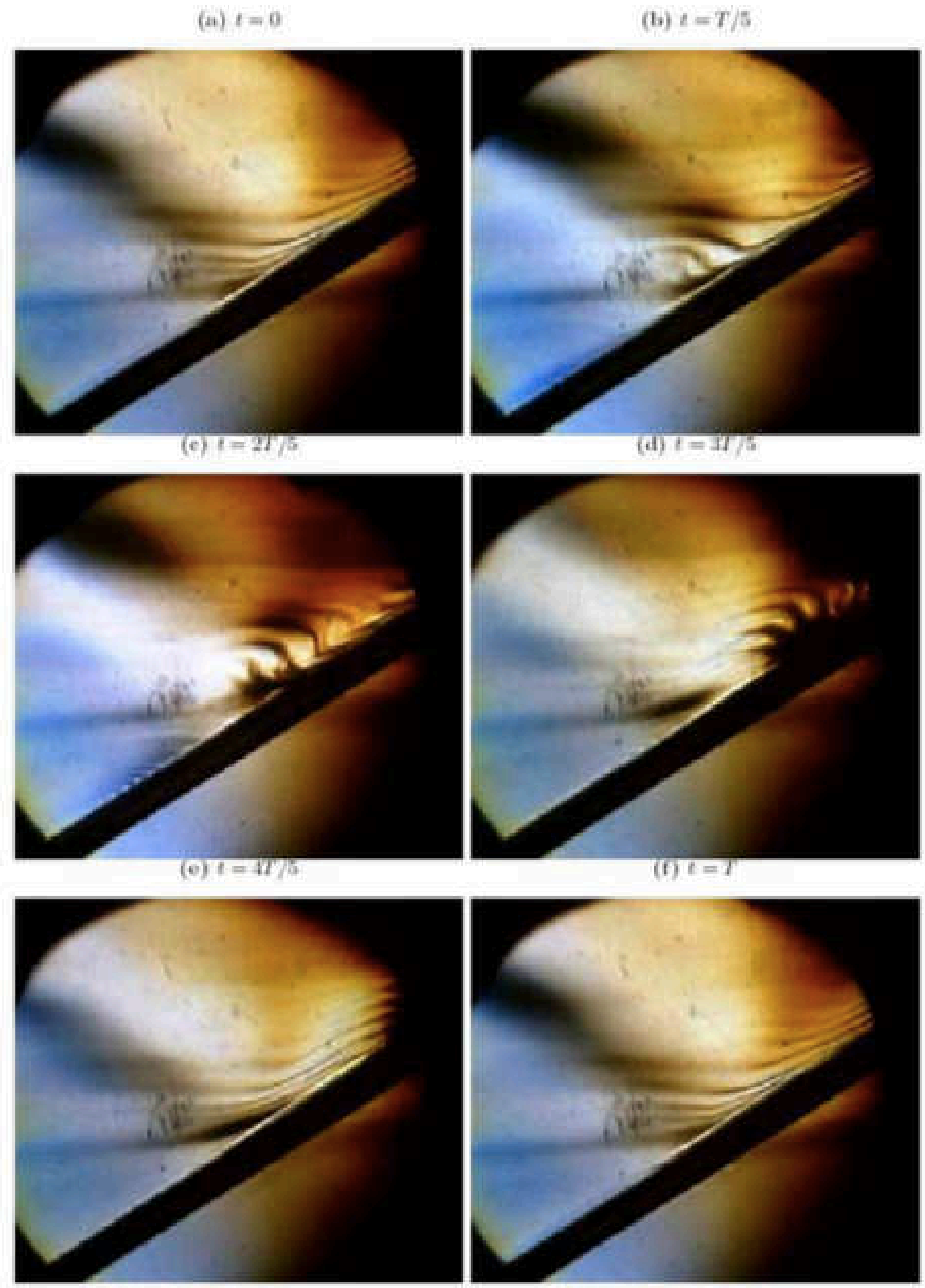

Figure 3.4: Images from the experiments of Dauxois et al. (2004) showing the Schlieren images of the isopycnal surfaces as they propagate and overturn while moving up a super-critical slope ($\gamma = 35°$) over one incident wave period.

amoorthy & Fringer (2012), when the gradient Richardson number (Equation 3.29) less than 0.25 the occurrence of dynamic instabilities is possible.

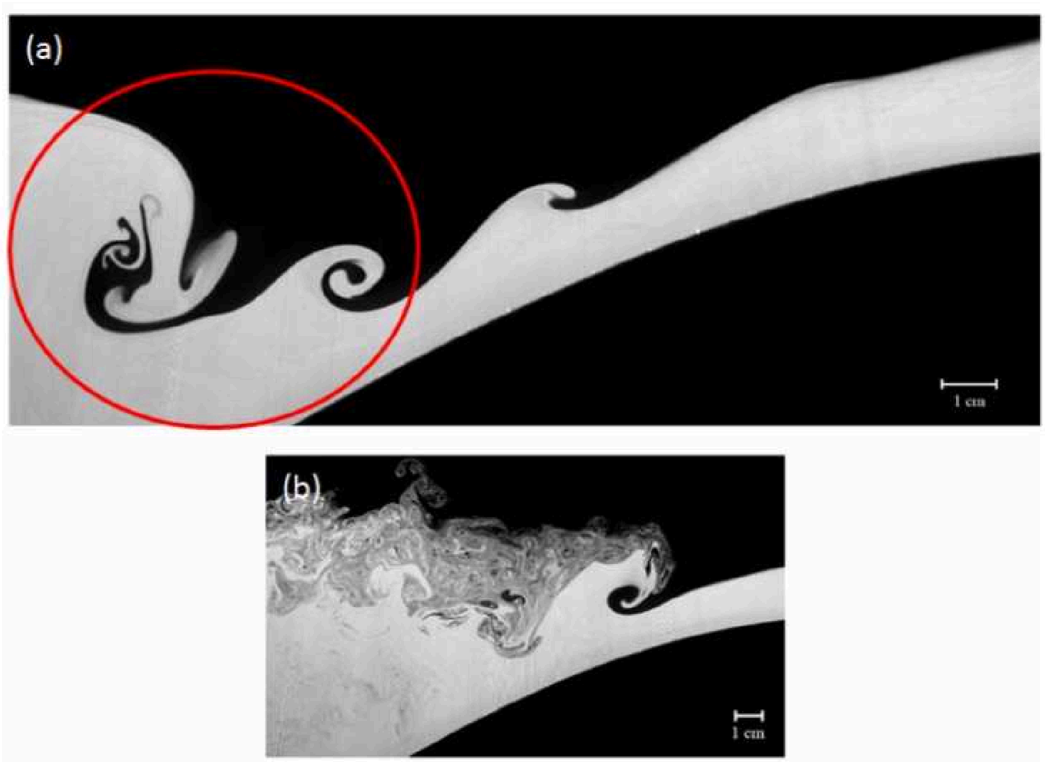

Figure 3.5: Two layer density stratified flow showing a dynamic (shear) instability in the form of Kelvin-Helmholtz billows. The irreversible turbulent mixing is seen in panel (b) where the sharp interface has been mixed (from Hult et al., 2009).

$$Ri_g = \frac{N^2}{\left(\partial U/\partial z\right)^2} \tag{3.29}$$

3.4.4 Internal tides

Internal waves in the ocean that have the same daily frequency as the global surface (barotropic) tides are called internal tides. Internal tides are also referred to as baroclinic tides and are generated by the interaction of stratified flow currents with mid-ocean ridges, continental shelves, seamounts and other bottom topographies (Wunsch, 1975). Shifts in the direction of the internal tide can significantly alter the dynamics of the flow field around bottom topography and as a result the degree of turbulent mixing (Jalali et al., 2017). Reviews of internal tides by Garrett & Kunze (2007) and Vlasenko et al. (2005) discuss the relevant experimental, analytical, and numerical study findings pertaining to their generation, transformation, dissipation and fate. Interaction between an internal tide and bottom topography is commonly characterized by the topographic steepness parameter, Eq. (3.26), the tidal excursion parameter, Eq. (3.28) and a ratio of the topographic height to the total fluid depth ($\delta = h/d$). Tidal energy conversion to turbulent mixing increases monotonically with the topographic obstacle height (h) and decreases monotonically as a function of obstacles horizontal length scale in cases with supercritical or critical topography (Pétrélis et al., 2006). For subcritical topography, various analytical solutions have been proposed for the amount of energy converted (Bell Jr, 1975; Bell, 1975; Llewellyn Smith & Young, 2002; Khatiwala, 2003). Numerical studies of internal tides by King (2010) and Nikurashin & Legg (2011) have been able to incorporate the non-linear term in the governing equations to provide a further insight into the dynamics. Studies by Legg & Huijts (2006) and Legg & Klymak (2008) focused on flow features leading to increased local mixing when an internal wave field was analyzed using the MITgcm (Marshall et al., 1997) model with physically realistic topography.

In the abyssal ocean, barotropic tidal currents radiating away from topographic or solid boundaries likely play a major role in the meridional overturning current (MOC) and maintaining global stratification and energy mixing (Munk & Wunsch, 1998; Wunsch & Ferrari, 2004). The eventual fate of internal tides in the oceanic environment is still poorly understood (Gerkema et al., 2006). Propagation away from boundaries is observed as both high and low-wave frequency modes where horizontal low-modes travel much more quickly then the vertical higher modes. Low-mode internal waves have been observed to travel $O(1000)km$ away from generation sites on the Aleutian Ridge or the Hawaiian Islands. Interaction between multiple internal tides is important for understanding the global ocean circulation and how the earth's oceans are mixed (Thorpe, 2005).

3.4.5 Lee waves

Lee waves form on the back side of a topographic obstacle when stably stratified fluid flows over the obstacle and accelerations resulting from the vertical displacement of the fluid create waves. These types of lee waves can be observed in the atmosphere when stratified flow encounters a mountain range or other obstacles and the fluid motion upward generates condensation and cloud formation (Kundu et al., 2008). Lee waves can be considered stationary relative to a solid boundary because the wave phase propagation is cancelled by the mean flow movement and the wave becomes phase-locked with the topography. Applications of linear theory usually consider steady flow conditions over a small obstacle of finite amplitude. As the inverse of the vertical Froude number, Fr_v, increases, the streamlines also steepen until they are vertical where the limit of applicability of the theory is reached. In cases where there is high value for the inverse vertical Froude number, there is non-linear wave breaking and overturning. As these waves become more and more non-linear, the flow field can transform itself into a spilling and plunging flow behind the obstacle (Smith, 1985). Lee waves have been extensively studied and modeled using experimental (e.g. Vosper et al., 1999; Dupont et al., 2001) and numerical methods (e.g. Huppert & Miles, 1969; Lilly & Klemp, 1979; Smith, 1985; Muraki, 2011) including variations in the shape of the topographic obstacle.

3.4.6 Flow splitting

Flow splitting occurs when a stratified flow encounters a topographic obstacles and splits to travel around the obstacle rather than working against the stratification to flow over the obstacle. In some cases the stratification can help force a flow into this type of separated two-dimensional flow. Explanation of conditions where this type of flow is generated by an obstacle, rather than a lee wave, relies on the analysis using vertical Froude number Fr_v and a theoretically formulated critical height given by the Sheppard formula, Equation 3.30, which is a function of the vertical Froude number (Drazin, 1961),

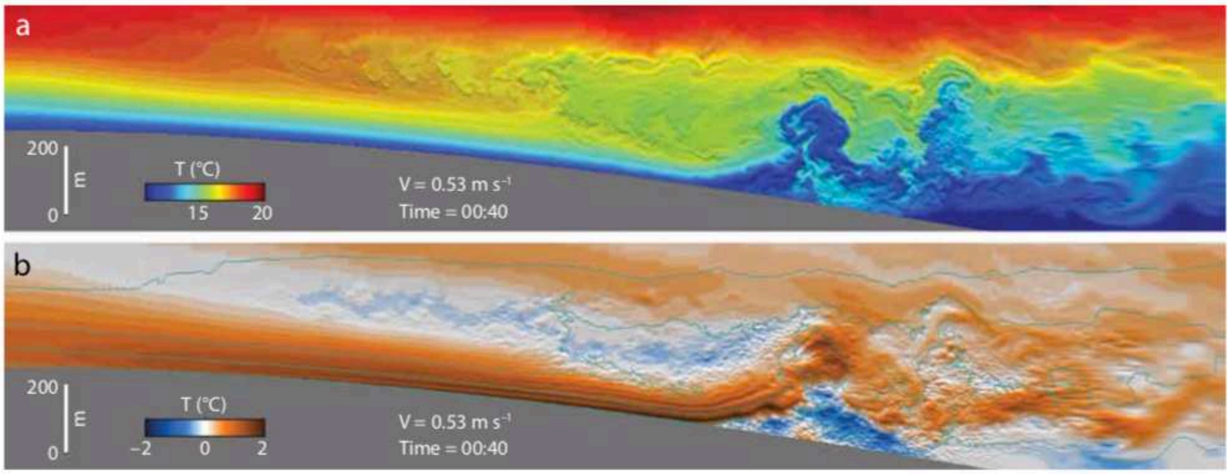

Figure 3.6: Breaking lee waves from a detailed simulation of off ridge flow where the size of the breaking wave is $\approx 200m$. Panels are colored by temperature and show off-ridge (a) and cross-ridge (b) flow (from Klymak et al., 2012).

$$z_c = h\left(1 - \frac{U}{nh}\right), \tag{3.30}$$

where z_c is the height when the flow will have sufficient energy to overcome the topographic obstacle and form lee waves. Figure 3.7 shows the effect of stronger stratification on the development of separated flow regimes. Flow splitting regimes can also combine and interact with lee wave formation. Hunt & Snyder (1980), Snyder et al. (1985), Vosper et al. (1999), and Ding et al. (2003) have all shown analysis of flow splitting as a function of z_c.

3.4.7 Boundary layer separation

Separation of the boundary layer in stratified flow over obstacles is the result of non-linear dynamics where the flow rapidly decelerates and creates an adverse pressure gradient. The product of the aspect ratio of the topographic obstacle (h/A_d, where A_d is defined as the lee-side half width) and the inverse of the vertical Froude number is commonly used to define degrees of boundary layer separation into three regimes: (1) boundary-layer separation ($NA_d/U < \pi$); (2) attached boundary

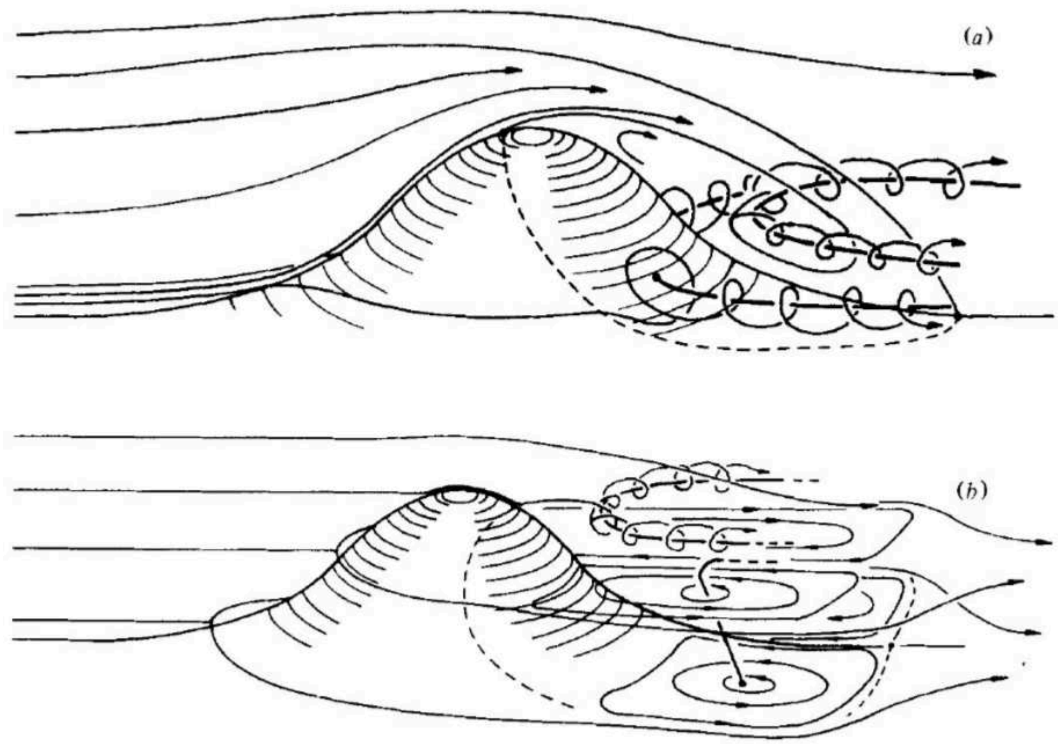

Figure 3.7: Depiction of flow encountering a three-dimensional topographic obstacle with (a) neutral stratification and (b) stable stratification ((Hunt & Snyder, 1980)).

layer ($NA_d/U \geq \pi$); and (3) possible post-wave (lee or internal) separation where the separation occurs beneath the first lee-wave crest. Ambaum & Marshall (2005) showed that the degree of stratification impacts the location of the boundary layer separation. Boundary layer separation can result in a separate (second) internal wave generation mechanism then the encountered topography (Sutherland, 2002; Aguilar & Sutherland, 2006; Aguilar et al., 2006). Hunt & Snyder (1980) use a possible boundary layer separation to explain eddies circulating around vertical axes in stratified wake structures.

3.4.8 Internal hydraulic jump

Like hydraulic jumps observed in open channel flow, internal hydraulic jumps are a function of flow accelerations creating wave steepening and breaking. Internal hydraulic jumps are not well understood but have been observed as a result of flow interaction with topography (Armi

& Mayr, 2011), straits, fjords and sills (Wesson & Gregg, 1988; Cummins et al., 2006; Moum & Smyth, 2006; Gregg & Pratt, 2010) and in the abyssal ocean (Alford et al., 2013). Hydraulic jumps can lead to significant amounts of turbulent mixing. Thorpe (2010) and Thorpe & Li (2014) present the only significant research on internal hydraulic jumps in a continuously stratified fluid. Formation and structure of internal hydraulic jumps is theorized to be increasingly complex with their formation as a result of interaction with three-dimensional topography (Baines, 1998). More observations and studies of these types of waves would help quantify and understand their impact on mixing, turbulence and the distribution of energy.

3.4.9 Gravity Currents

When there is a current of fluid that has a higher density than the surrounding horizontal fluid, it is classified as a gravity current. The two main types of gravity currents are intrusive gravity currents (IGC) that travels through an ambient fluid at the level of neutral buoyancy and bottom boundary gravity currents (BBGC) that travel along a solid boundary. These types of gravity currents can result from the mixing and turbulence generated by internal wave and stratified flow interaction with topographic obstacles and create significant mixing and entrainment of sediments on their own. Most studies of gravity currents on sloping bottom topography have been conducted within a homogenous fluid. Simpson (1999) provides a comprehensive treatment of gravity currents in his book on the subject.

3.4.10 Recent analysis

The vast majority of research on internal waves interacting with topography concentrates on the continental slope/shelf. A comprehensive review of the laboratory, numerical and field work analyzing internal waves near the continental slope is presented by Lamb (2014). Research has shown that some of the energy contained in internal tides/waves dissipates through turbulence and mixing at continental slopes, however, it is also recognized that a significant portion of this energy is radiated away from the continental margins (Venayagamoorthy & Fringer, 2006). Some research has focused on the interactions of internal waves in a continuously stratified fluid with isolated or ridge-like topography. Wessels & Hutter (1996), Sveen et al. (2002), Chen et al. (2008) and Chen (2009) showed results from experiments of internal solitary waves in two-layer flows interacting with gaussian hills and triangular topography. Numerical simulations by Legg & Adcroft (2003) investigated the interaction of internal waves with concave and convex slopes, on corrugated slopes with cross-slope (Legg, 2004a) and along-slope barotropic forcings (Legg, 2004b) and with an isolated gaussian ridge (Legg, 2014). Works by Jalali et al. (2017), Jalali & Sarkar (2017), Musgrave et al. (2016), Nikurashin & Legg (2011), Legg & Klymak (2008), and have evaluated numerical results (sometimes in combination with field data) of internal wave interactions with rough topography, isolated idealized ridges, single triangular ridges and a cross-section of actual topography. Results from Jalali & Sarkar (2017) and Jalali et al. (2017) are shown in Figure 3.8 and Figure 3.10, respectively. There are no studies in the current literature comprehensively analyzing the interaction between internal waves and multiple ridges or multiple isolated structures especially at scales below the field scale and above the laboratory scale. Research on the physics of internal waves interacting isolated and multiple ridges remains an open line of inquiry. The analysis presented herein aims to start filling in a portion of this knowledge gap.

Application of numerical simulations to help understand the physics of internal waves and interpret observational measurements is an increasing useful tool for engineers and scientists. Direct numerical simulation (DNS) has become a useful tool for analysis of small domains where an isolated set of waves can be analyzed and all turbulent scales can be resolved under various forcing and stratification conditions. Behavior of these waves can inform simulations and observations where the turbulent scales can not be fully resolved. Work by Garanaik & Venayagamoorthy (2019), Pouquet et al. (2018), Maffioli et al. (2016b), Mater & Venayagamoorthy (2014b), Mater et al. (2013) and Lindborg & Brethouwer (2008) are examples of periodic box DNS simulations that have been used to help understand the turbulence and mixing in stratified fluids. Due to the constraints put on DNS simulations by the limits of computational resources, large eddy simulations (LES) have become a popular alternative for more realistic replication of the flow physics then Reynolds-Averaged Navier-Stokes (RANS) models (Chow & Street, 2004). LES allows for

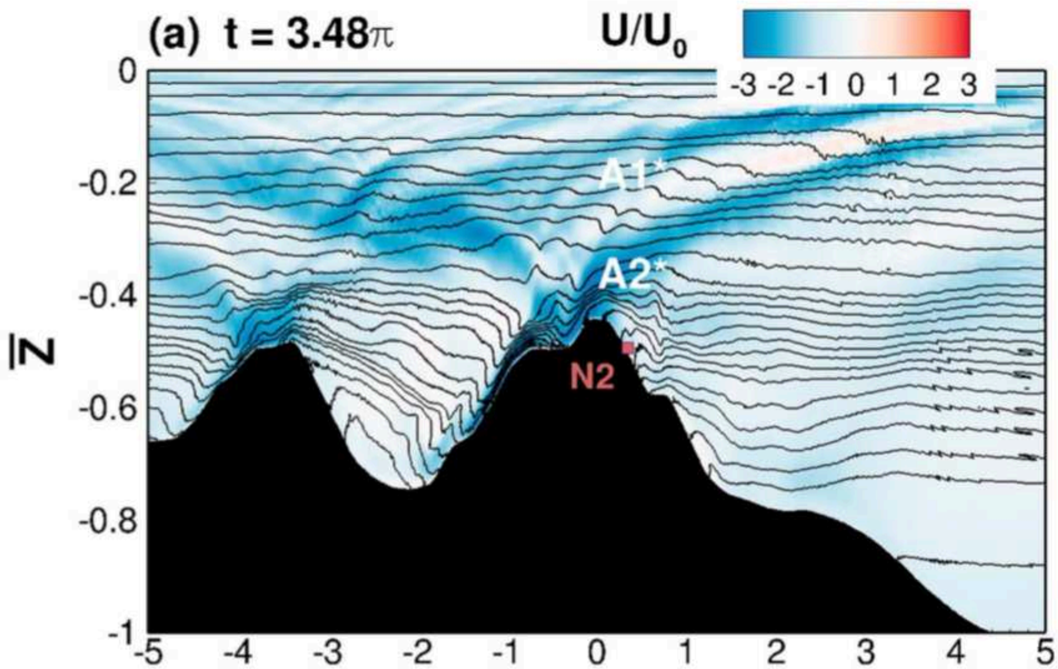

Figure 3.8: Snapshot from LES of a cross-section of topography of the Luzon Strait in the South China Sea. Figure shows normalized zonal velocity and density isopycnals (from Jalali & Sarkar 2017).

the small scales to be represented using small, subgrid-scale (SGS) parameterized turbulence closure models while the large energy containing scales are resolved. Division between the resolved and parameterized scales is done through either implicit or explicit filtering. Accuracy of LES can depend on how well the subfilter-scales have been modeled. Various SGS closure models have been proposed but the dynamic mixed model (DMM) (Zang, 1994; Zang et al., 1993) is commonly used in turbulent mixing analyses seen in environmental flows and has been used for a wide variety of applications (e.g. Fringer & Street, 2003). Other LES codes have been used to study internal waves (e.g. Slinn & Levine (2003), Skyllingstad & Wijesekera (2003)), which include the Stanford Unstructured Non-hydrostatic Terrain-Following Adaptive Navier-Stokes Simulator (SUNTANS) and MIT general circulation model (MITgcm). MITgcm has been used as a tool in this dissertation study to evaluate the scaling of internal wave-topography interaction at different scales.

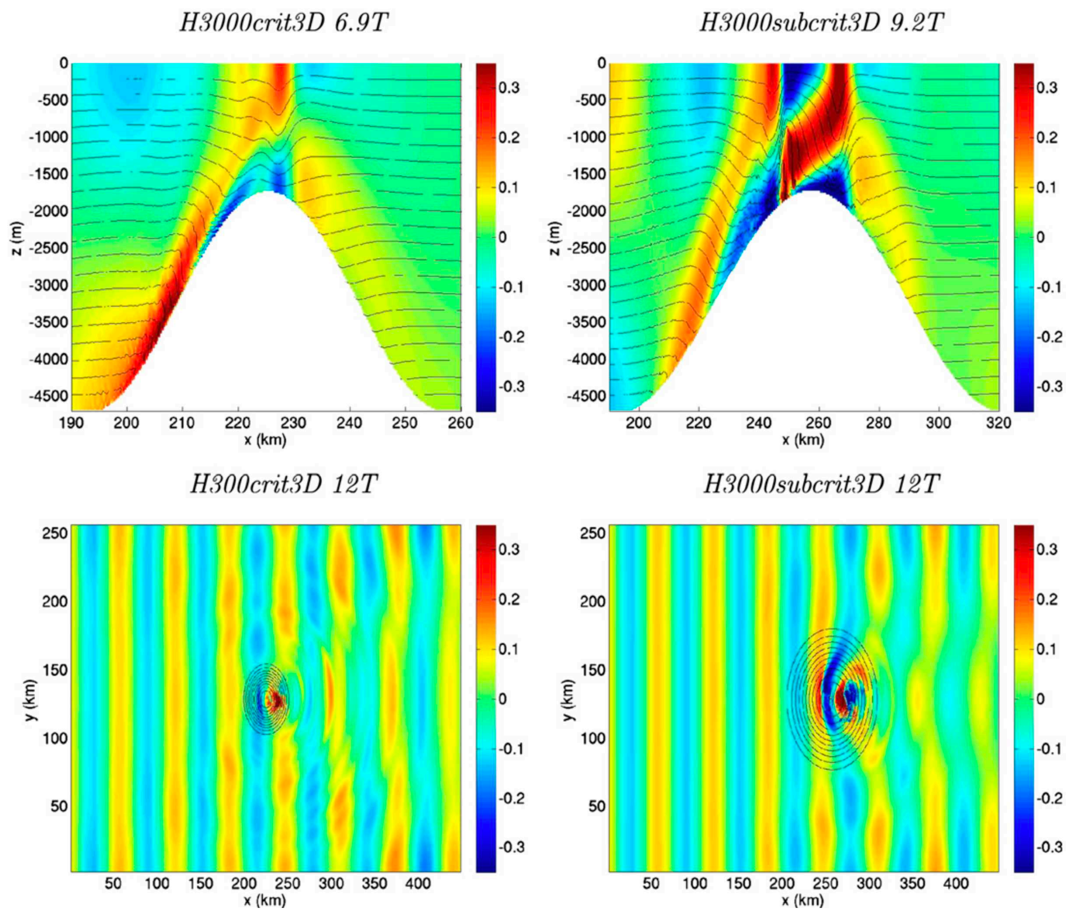

Figure 3.9: Field scales simulations in two and three dimensions by Legg (2014).

3.5 Summary

The four sections in this chapter present an introduction to stratified flows and internal waves, an overview of flow measurement instrumentation used in the field setting, dimensionless parameters relevant to the study of stratified flow interaction with topography and review of the past work on continuously stratified flow interacting with topographic obstacles. Relevant equations, parameters and terminology are all presented. A brief review of the main contributions from the theoretical, experimental, observational and numerical study of this topic is also covered as it pertains to this research. Understanding the basic turbulent mixing processes that arise as a result of the generation on the flow phenomena described in this chapter is the first step in being able to critically analyze numerical simulations of stratified flow interacting with topography. Dimensionless

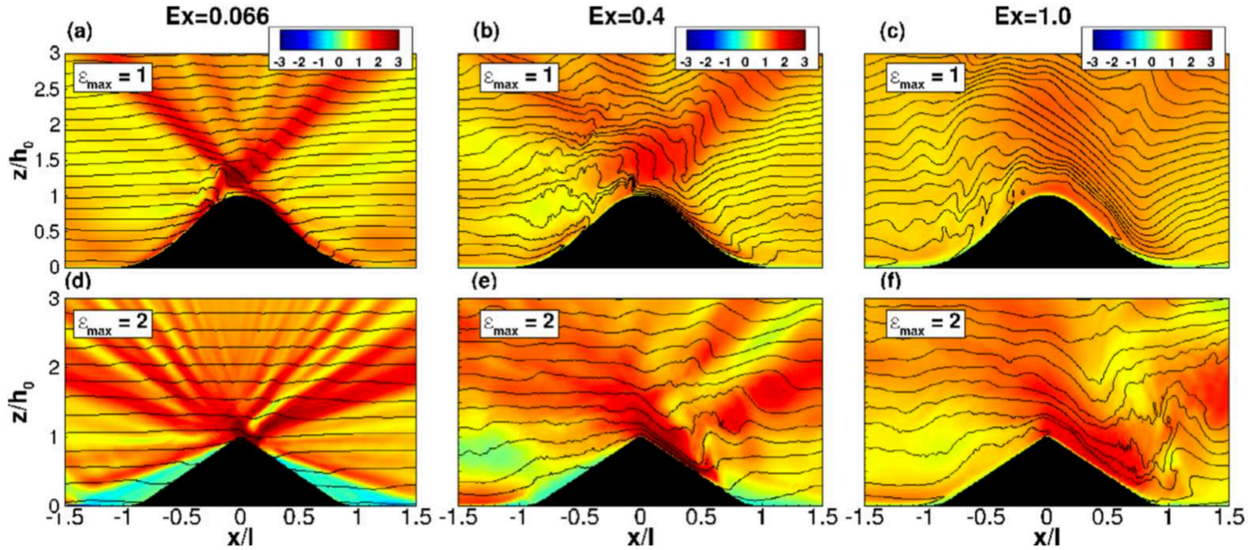

Figure 3.10: Velocity results of simulations by Jalali et al. (2017) of stratified flow over a single idealized ridge with variations in excursion number ($Ex = U_0/\Omega l$, where U_0 is the amplitude of the tidal velocity, Ω is the tidal frequency and l is the roughness half-length) in critical (a, b, c) and supercritical (d, e, f) cases.

parameters and scaling are used in the following section to analyze idealized stratified turbulence numerical simulations in the absence of boundary interactions.

Chapter 4

Revisiting the Osborn Model[3]

4.1 Introduction

Diapycnal mixing is the molecular diffusion of density across isopycnals (surfaces of constant density)(Osborn, 1980). In stratified flows, such as those found in the ocean, diapycnal mixing is essential for maintaining the circulation driving oceanic currents and the resulting overturning events, creating mixing of different fluid masses and transport of nutrients (Munk & Wunsch, 1998). However, there are numerous challenges for direct measurement of pertinent quantities needed to determine the diapycnal diffusivity K_ρ which provides the pathway for estimating turbulent heat/mass fluxes in oceanic flows. These include instrumentation that collects subsets of turbulence data, data collected in only the vertical dimension (as profiles) and an inability to make reliable measurements near boundaries (Osborn & Lueck, 1985; Hult et al., 2011; Venayagamoorthy & Koseff, 2016; Gregg et al., 2018). Widely used instrumentation for oceanic measurement that are directly mounted to a buoy or ship include ADCPs (acoustic Doppler current profilers) and CTD (conductivity-temperature-depth) probes. Another common autonomous instrument is the VMP (vertical microstructure profiler) which is released from the surface and collects data while free-falling through the ocean.

Thus, by necessity, a number of indirect methods are commonly used in oceanography for quantifying K_ρ. Of these, the model due to Osborn (1980) has found widespread use. Under the assumptions of statistical homogeneity and stationarity, the diapycnal diffusivity is obtained from

[3]The research presented in this chapter has been submitted to the *Journal of Fluid Mechanics* under the title “On the use and misuse of the Osborn model: Implications for improved estimates of ocean mixing rates" by M. R. Klema and S. K. Venayagamoorthy. This chapter is written to reflect and acknowledge the contribution of Dr. S. K. Venayagamoorthy.

the turbulent kinetic energy equation using the gradient diffusion hypothesis as

$$K_\rho = \Gamma \frac{\epsilon}{N^2}, \tag{4.1}$$

where $\Gamma = R_f/(1-R_f)$ is called the irreversible mixing coefficient, ϵ is the turbulent kinetic energy dissipation rate, and N is the buoyancy frequency associated with the background stratification. $R_f = \epsilon_{PE}/(\epsilon_{PE} + \epsilon)$ where ϵ_{PE} is the dissipation rate of turbulent potential energy, is known as the diapycnal mixing efficiency, or flux Richardson number (see Ivey & Imberger 1991, Peltier & Caufield 2003, Venayagmoorthy & Stretch 2010 and Venayagamoorthy & Koseff 2016, for detailed discussions on the flux Richardson number).

In the oceanic setting the irreversible mixing coefficient Γ is often assumed to have the constant value of $\Gamma_c = 0.2$ (Osborn, 1980; Bouffard & Boegman, 2013). Validity of assuming that this parameter has a constant value has been challenged and debated (Gregg et al., 2018; Ijichi & Hibiya, 2018; Mater & Venayagamoorthy, 2014a). Various parameterizations for the mixing efficiency have been proposed (Mater & Venayagamoorthy, 2014a; Monismith et al., 2018) but the constant value of 0.2 for Γ has received widespread acceptance and application for estimating diapycnal diffusivities using the Osborn model in oceanic flows. Assumption of a constant irreversible mixing coefficient oversimplifies diapycnal mixing as the turbulent diffusivity should depend on the magnitudes of turbulence and stratification in a flow. This is summarized by Maffioli & Davidson (2016) and Venayagamoorthy & Koseff (2016) who show the irreversible mixing coefficient as the ratio of the turbulent potential and kinetic energy dissipation rates, $\Gamma = \epsilon_{PE}/\epsilon$. This irreversible definition of the mixing coefficient is used for the present analysis. Garanaik & Venayagamoorthy (2019) (hereafter GV19) used direct numerical simulations (DNS) of homogeneous stratified turbulence to clearly show that the value of the irreversible mixing coefficient is not a constant but instead has a strong functional dependance on the magnitude of the turbulent Froude number, $Fr_t = \epsilon/Nk$, where k is turbulent kinetic energy.

The rate of dissipation of turbulent kinetic energy, ϵ, is often inferred in one of two ways. The first method is to directly infer ϵ from microstructure measurements that typically use shear probes to measure two out of the nine turbulent components of the fluctuating velocity gradient tensor of a three-dimensional velocity field (Osborn & Cox, 1972; Thorpe, 2005). To do this, the assumption of local isotropy is invoked (Danaila et al., 2017; Garanaik & Venayagamoorthy, 2018). This assumes that the kinetic energy and corresponding kinetic energy dissipation rate is equivalent with respect to all three coordinate dimensions (Thorpe, 2005). Whenever this assumption is made it is denoted ϵ_{1D} in the analysis presented in this paper. Gregg et al. (2018), Itsweire et al. (1993) and Garanaik & Venayagamoorthy (2018) show that the isotropy assumption for the kinetic energy dissipation rate is valid for stratified flows when the turbulent Froude number, $Fr_t \geq 1$. However, when the flow is strongly stratified (typically for $Fr_t < 1$), then the isotropy assumption starts to break down. Increased stratification limits the component of the velocity field in line with the stratification and results in a non-isotropic velocity field (Gargett, 1988; Holford & Linden, 1999; Lindborg & Brethouwer, 2008).

The second method indirectly infers a kinetic energy dissipation rate through an equivalency assumption between derived kinematic scales namely: the Ozmidov length scale (Ozmidov, 1965) and Thorpe length scale (Thorpe, 1977). The Ellison length scale (Ellison, 1957) has also been used as an alternative to the Thorpe length scale given that they have been found to track each other quite well (Itsweire et al., 1993; Mater et al., 2013). In oceanic flows, the Thorpe length scales are determined from instantaneous vertical density profiles (typically using CTD casts from a ship or mooring) or from VMP dropped from a ship. Using such one-dimensional profiles, both the Thorpe (L_{Th}) and Ellison (L_E) scales provide a statistical measure of the vertical distance travelled by fluid parcels in order to achieve a position of equilibrium (Thorpe, 2005; Ellison, 1957). Further details of these length scales can be found in the works of Dillon (1982), Winters et al. (1995), Ellison (1957) and Thorpe (1977). The Ozmidov length scale is a kinematic length scale that is often used to define the size of an isotropic large eddy scale that is unaffected by buoyancy in stratified turbulence. Thus, based on the grossly simplifying assumption that the Thorpe scale (L_{Th}) is equivalent to the Ozmidov scale ($L_O = (\epsilon/N^2)^{1/2}$), the rate of dissipation of turbulent kinetic energy is inferred (i.e. $\epsilon_{Th} = L_{Th}^2 N^3$). Mater et al. (2013) presented arguments that L_O

and L_{Th} are only equivalent for flow conditions with a turbulent Froude number of order 1. Smyth & Moum (2000) showed that the ratio of the Thorpe and Ozmidov length scales can be used to estimate the age or evolution of a turbulent event. The analysis of GV19 rigorously showed that the ratio of the Ellison (or Thorpe) and Ozmidov length scales can be used to infer both the local state of turbulence and the mixing efficiency in stably stratified turbulent flows. These three length scales see widespread application given that they can be readily calculated from measured field data.

Despite the numerous studies pertaining to these prevalent issues with the Osborn model, to the best of our knowledge, no systematic study has been done to pinpoint the consequences of these assumptions on mixing estimates. Thus, the main aim of this research is to bring to focus how these common assumptions and practices associated with the use of the popular Osborn model have a significant impact on estimates of the diapycnal diffusivities. In what follows, the key non-dimensional parameters that will be used for the analyses presented and that are pertinent in stratified turbulence are discussed in §4.2. This is followed by a short discussion on the direct numerical simulations that are used as testbed for the analyses presented is discussed in §4.3. Results that systematically show how these common assumptions cause the diapycnal diffusivities to vary by orders of magnitude compared to the exact true diffusivities directly obtained from DNS are presented in §5.4. Concluding remarks are made in §4.5.

4.2 Common dimensionless parameters

There are several dimensionless numbers that are important in the study of stratified turbulence of which two will be highlighted given their significance and use in the results presented. Perhaps the buoyancy Reynolds number $Re_B = \epsilon/\nu N^2$, where ν is the kinematic viscosity, is most popular mainly due the fact that it can be calculated readily from measured quantities in the ocean. However, Re_B is an ambiguous parameter in that for any given value, the mixing efficiency (or coefficient) can vary by an order of magnitude (Mater & Venayagamoorthy 2014 and GV19). Despite its ambiguity, it can be used as a diagnostic for evaluating the intensity of turbulence and mixing in stably stratified flows.

Another useful dimensionless parameter is the turbulent Froude number Fr_t. It has proved to be a robust parameter for determining the particular state of a stratified flow, i.e., at low values of Fr_t, the flow is strongly influenced by buoyancy effects and conversely at high Fr_t by turbulence. This is evident when its definition is cast as a competition of the buoyancy timescale (N^{-1}) to the turbulence decay time scale ($T_L = k/\epsilon$). As pointed out by GV19, Fr_t can be used a diagnostic indicator of the local state of evolution of a stably stratified flow. GV19 go onto to provide physically based scaling arguments to quantity Γ as a function of Fr_t. Here, we will use Fr_t as the primary non-dimensional parameter to assess the impact of each of the common assumptions used for calculating K_ρ via the Osborn model.

The ratio between the turbulent diapycnal diffusivity (K_ρ, as defined by Equation 4.1) and the molecular diffusivity (κ), denoted here as $\hat{\kappa}$ is defined by Equation 4.2. This is a useful non-dimensional way to represent K_ρ especially when applied to DNS data, to clearly show the magnitude of the diapycnal diffusivity relative to its molecular counterpart. We note that $\hat{\kappa}$ can be defined using ϵ_{PE}, N and κ and cast in terms of relevant non-dimensional parameters as shown in Equation 4.2 where $Pr = \nu/\kappa$ is the Prandtl number.

$$\hat{\kappa} = \frac{K_\rho}{\kappa} = \frac{\epsilon_p}{N^2 \kappa} = \Gamma Re_B Pr. \tag{4.2}$$

4.3 Simulations and Data

The direct numerical simulations for this analysis were completed using the pseudo-spectral code developed by Riley et al. (1981) and were initially presented in Garanaik & Venayagamoorthy (2018). The simulations solve the Navier-Stokes equations with the Boussinesq approximation for stably stratified homogeneous decaying homogeneous turbulent flows in a non-dimensional 2π cubic domain with 512^3 grid points and periodic boundary conditions. This DNS data was also used in the analysis presented in GV19. These types of simulations are used to study transient or episodic turbulent flow behavior such as breaking internal waves in the oceans. Initial turbulent kinetic energy in the simulations results from an imposed three dimensional Gaussian isotropic solenoidal velocity field. The initial velocity scale (u_0) and initial length scale were both set equal to 1. Characterization of the background stratification was set by an initial Richardson number $Ri_0 = (NL_0/u_0)$ with values of $Ri_0 = 0.01, 0.1, 1.0$ and 10 for each of the four respective simulations presented. This range of Richardson numbers cover flow conditions representative of weakly to strongly stratified conditions, respectively. All four simulations were run for a duration of $5L_0/u_0$. In all simulations the molecular Prandtl number $Pr = 1$ for all simulations to ensure accurate resolution of the dissipative scales of the density (scalar) field. Garanaik & Venayagamoorthy (2018) provide further details of these simulations.

4.4 Results

The goal of this section is to use the DNS results to illustrate how the common assumptions used with the application of the Osborn model individually impact estimates of turbulent diffusivities. Using the four DNS runs, implications of these assumptions are systematically investigated. Three parameters are used in the calculation of the diffusivity as presented in Equation 4.1. In Section 4.4.1 the assumption of a constant (irreversible) mixing coefficient $\Gamma_c = 0.2$ is discussed. Implications of estimates of the dissipation rates of turbulent kinetic energy, ϵ, using an assumption of local flow isotropy (as is done in the field when using microstructure data) and indirectly by inference from kinematic flow scales are examined in Section 4.4.2. The combined impact of the simplifications and assumptions made in quantifying K_ρ is discussed in Section 4.4.3. Section 4.4.4 provides a brief discussion on improving estimates of diapycnal diffusivity from available measurements. The third parameter in Equation 4.1 is N, the buoyancy frequency. Estimating the background density stratification against which turbulence must work to mix fluids of different densities in the field is not trivial. Investigation of this parameter is beyond the scope of the present analysis and is an area for further investigation. The interested reader is referred to Arthur et al.

(2017) for a detailed discussion on how the way N is computed can impact estimates of diapycnal mixing in stratified flows.

4.4.1 Implications of a constant irreversible mixing coefficient

Figure 4.1a shows the diffusivity ratio ($\hat{\kappa}$) plotted as a function of the turbulent Froude number (Fr_t and colored by the buoyancy Reynolds number (Re_B). Diffusivity ratios ($\hat{\kappa}$) of the four DNS was calculated two different ways. The first approach calculates diffusivity ratio using the irreversible definition for the mixing coefficient ($\Gamma = \epsilon_{PE}/\epsilon$) denoted $\hat{\kappa}_\rho$. The second set of data uses the assumed constant value of $\Gamma_c = 0.2$ to calculate the diffusivity ratio, denoted $\hat{\kappa}_c$. In both these calculations, values for the kinetic energy dissipation rate, ϵ, were taken directly from the DNS. This figure clearly shows that assuming a constant value of 0.2 for the irreversible mixing coefficient results in different values of diffusivities than those calculated using the irreversible definition. At higher turbulent Froude number ($Fr_t > 1$) the use of Γ_c over-predicts the true diffusivity. When the turbulent Froude number is close to unity, the diffusivities calculated using Γ_c are equivalent to those calculated using Γ (i.e., $\hat{\kappa}_c \approx \hat{\kappa}_\rho$). As the magnitude of the turbulent Froude number decreases ($Fr_t < 1$), buoyancy effects become more dominant and the diffusivity ratio $\hat{\kappa}_c$ under-predicts the true diffusivity ratio $\hat{\kappa}_\rho$.

In order to clearly highlight the implication of the constant $\Gamma_c = 0.2$ assumption, Figure 4.1b shows the data presented in Figure 4.1a normalized by $\hat{\kappa}_\rho$. Diffusivities calculated using this true turbulent definition necessarily collapses on itself and the impact of the constant assumption for Γ becomes striking. At higher turbulent Froude numbers, the assumption of $\Gamma_c = 0.2$ results in estimates for the diffusivity ratio up to two orders of magnitude greater than the diffusivity determined directly from the turbulent quantities. As the buoyancy effects increase, the difference between $\hat{\kappa}_c$ and $\hat{\kappa}_\rho$ decreases until they are equivalent as Fr_t approaches unity. Below $Fr_t < 1$, $\hat{\kappa}_c$ under predicts $\hat{\kappa}_\rho$ and reaches a constant value that is about 5 to 6 times less than the exact value $\hat{\kappa}_\rho$. It is clear from this data analysis that an assumption of a constant $\Gamma = 0.2$ is not accurate because the mixing efficiency is a dynamic variable that is strongly dependent on the

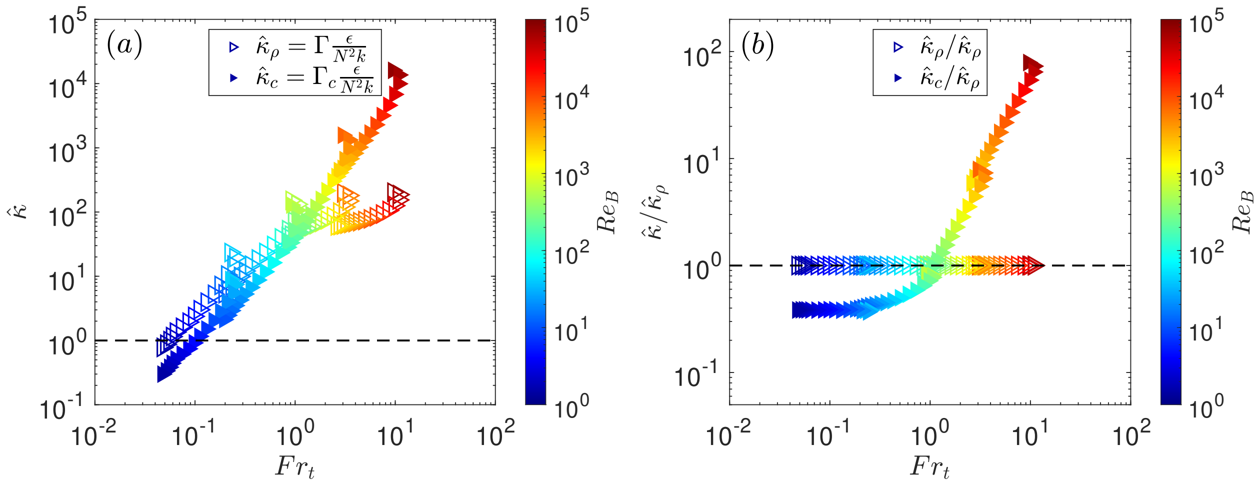

Figure 4.1: (a) Diffusivity ratios plotted as a function of the turbulent Froude number, Fr_t. Data plotted as open triangles apply the turbulent definition of the irreversible mixing coefficient ($\Gamma = \epsilon_{PE}/\epsilon$) in calculating the turbulent diffusivity. The data presented as filled triangles assumed $\Gamma = 0.2$ when calculating the turbulent diffusivity. (b) Diffusivity ratios normalized by $\hat{\kappa}_\rho$. All data is colored by the buoyancy Reynolds number, Re_B.

flow conditions as has been pointed out previously by a number of studies such as GV19. The agreement at $Fr_t \sim 1$ is somewhat not surprising given that the turbulence and buoyancy time scales are approximately equal. However, the constant value of $\Gamma = 0.2$ at $Fr_t \approx 1$ is coincidental and should not be considered a robust result. Regardless, what is clear is that the assumption of a constant Γ does have a significant and differing impact on estimates of turbulent diffusivity depending on competition between the stratification and turbulence in a given flow.

4.4.2 Implications of an inferred kinetic energy dissipation rate

Figure 4.2a shows the three inferred dissipation rates of turbulent kinetic energy, ϵ_{1D}, ϵ_{L_E} and ϵ_{Th} normalized by the exact dissipation rates ϵ obtained directly from the DNS, plotted as a function of the turbulent Froude number. Results calculated by indirect inference using the Ellison and Thorpe scales closely track each other confirming the analysis of Itsweire et al. (1993) and Mater et al. (2013). For low values of the turbulent Froude number, the inferred rates of dissipation of kinetic energy are 15-18 times larger than ϵ. Above $Fr_t \sim 1$, ϵ_{L_E} and ϵ_{Th} under-predict ϵ resulting in a ratio close to zero. Results show that an assumption of isotropy is less significant, over-predicting the kinetic energy dissipation rate by a factor of two for strongly stratified conditions

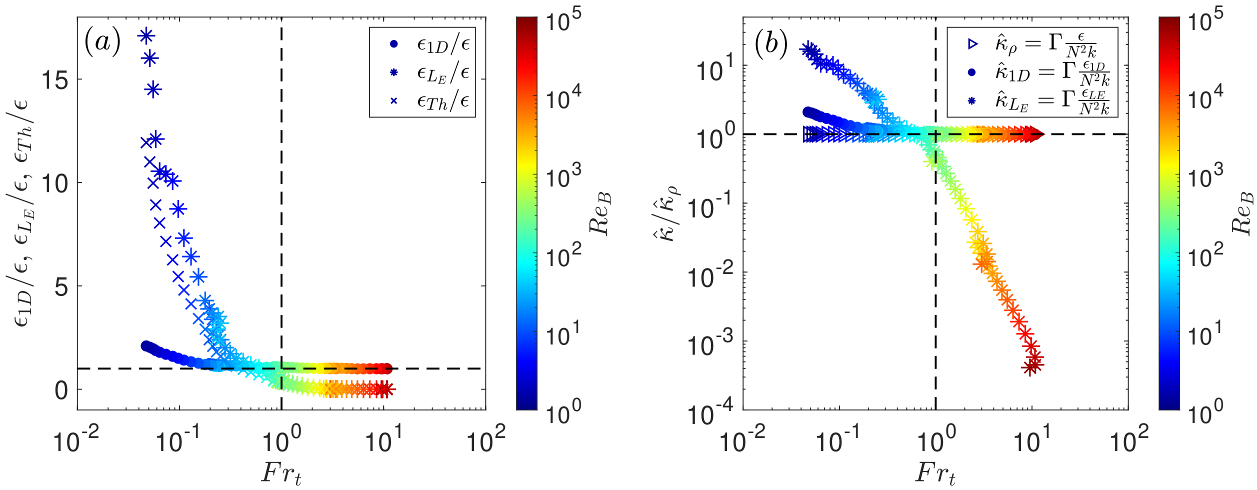

Figure 4.2: (a) Normalized rates of dissipation of turbulent kinetic energy inferred using an assumption of local isotropy (ϵ_{1D}) or derived from the Ellison length scale (ϵ_{L_E}) and Thorpe length scale (ϵ_{Th}), as a function of the turbulent Froude number, Fr_t. These are all normalized by the true dissipation rates ϵ obtained directly from the DNS. (b) Normalized diffusivity ratios using inferred rates of dissipation. All data is colored by values of the buoyancy Reynolds number, Re_B.

($Fr_t << 1$). This over-prediction decreases as Fr_t increases becoming functionally equivalent to the exact dissipation rates above $Fr_t > 1$, for weakly stratified flow conditions. Figure 4.2b shows the results of using ϵ_{1D} and ϵ_{L_E} in calculations of normalized turbulent diffusivity ratio. If ϵ_{1D} is used the over-predictions remain much less than an order of magnitude for flows at low Fr_t and becomes equivalent at high Fr_t which indicates that anisotropic effects of stratification are not dominant/important when $Fr_t > 1$. Using ϵ_{L_E} in calculations of the turbulent diffusivity amplifies the differences shown in Figure 4.2a. In the strongly stratified flow regimes ($Fr_t < \mathcal{O}(0.1)$) the turbulent diffusivity is up to one order of magnitude greater than $\hat{\kappa}_\rho$. For $Fr_t > \mathcal{O}(1)$ the turbulent diffusivity calculated using ϵ_{L_E} ($\sim \epsilon_{Th}$) results in an under-prediction of the turbulent diffusivity by up to three orders of magnitude for $Fr_t \approx 10$). This is a result of the inferred $\epsilon_{L_E/Th}$ having very small magnitudes compared to the true dissipation rates for weakly stratified flow conditions. This result has important implications in the field when only CTD profiles are used to infer mixing rates in a weakly stratified turbulent flow field since such profiles would hardly reveal any major overturning events even though the turbulence is strong.

4.4.3 Implications of a constant irreversible mixing coefficient combined with an inferred kinetic energy dissipation rate

As pointed out previously, it is common practice to use a constant mixing coefficient combined with an inferred kinetic energy dissipation rate in applications of the Osborn model. Figure 4.3 shows the differences in turbulent diffusivities calculated with these two combined assumptions. All data are plotted as a function of the turbulent Froude number. Figure 4.3a shows the magnitudes of the diffusivity ratio while Figure 4.3b shows the values normalized by $\hat{\kappa}_\rho$ as also used in Figure 4.1b and Figure 4.2b. The turbulent diffusivity is over-predicted in flows dominated by buoyancy effects (low Fr_t) by up to one order of magnitude and under-predicted by almost two orders of magnitude for flows with low stratification when Γ_c and $\epsilon_{L_E/Th}$ are both used. These results show that while these assumptions may be acceptable for flow regimes with $Fr_t \sim \mathcal{O}(1)$, for flow regimes that are characterized by a turbulent Froude number outside this narrow intermediate range, the combination of these two assumptions will lead to predictions of turbulent diffusivities that are much different than the actual flow diffusivities.

As could be predicted based on observing the data trends in Figure 4.1 and Figure 4.2 the combination of Γ_c and ϵ_{1D} results in an estimate of turbulent diffusivity for flows with $Fr_t < O(1)$ that is not significantly different from the true magnitude. under-prediction of the turbulent diffusivity created by Γ_c is mostly offset by the over-prediction created by using ϵ_{1D} in strongly stratified flow regimes. Above $Fr_t > \mathcal{O}(1)$ the assumption of Γ_c dominates the estimates creating an over-prediction that reaches up to two orders of magnitude. The nearly constant turbulent diffusivity shown in Figure 4.3b for the more strongly stratified flows is simply a result of combining the two different assumptions and is not a physical characteristic of the flow. We have used data and analysis driven by the physics of the controlling equations applied in the DNS to show that while these common assumptions may be acceptable when using microstructure measurements ($\sim 2-3$ times difference) it has been traditionally made for the wrong reasons. Such a systematic analysis that breaks down and analyzes the impact of each of these parameters has not been shown previously.

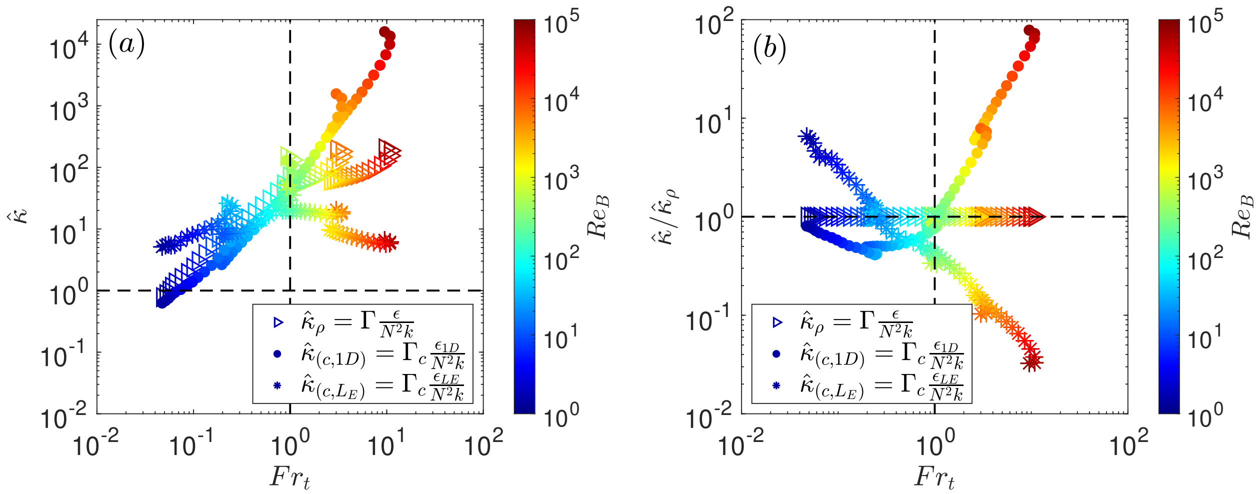

Figure 4.3: Plots illustrating the combined impact of a constant mixing coefficient and inferred rates of dissipation of turbulent kinetic energy as a function of turbulent Froude number, Fr_t. (a) Diffusivity ratios calculated using (i) isotropic assumption in conjunction with a constant $\Gamma_c = 0.2$; (ii) inferred dissipation rates from Ellison scale in conjunction with a constant $\Gamma_c = 0.2$; and (iii) true diffusivity ratio from DNS. (b) Diffusivity ratios shown in (a) normalized by $\hat{\kappa}_\rho$. All data is colored by the Buoyancy Reynolds number, Re_B.

4.4.4 Implications for improved estimates of ocean mixing

In the light of these issues, the question then is how to move forward? Here we briefly discuss how best to leverage these insights to improve estimates of ocean mixing even when only limited physical field measurements are available. Use of scaling insights developed from physically based arguments in combination with careful consideration of the assumptions made will directly incorporate consideration of the relevant flow physics and limit unnecessary approximations. The turbulent Froude number as used in this analysis is a useful parameter for indicating the local state of turbulence (GV19) and as a measure of the competition between the turbulence and buoyancy time scales in stratified flows (Mater et al., 2013). While the parameter is useful for flow classification and theoretical analysis, it is difficult to calculate from field measurements but it turns out that it does not need to be explicitly determined for improved estimates. For example, GV19 show that the Fr_t can estimated using the ratio between L_E and L_O (see their Figure 3). Analysis in Section 4.4.1 clearly corroborates the assertion that the irreversible mixing coefficient can not be assumed constant. Determination of the best estimate of the irreversible mixing coefficient can be determined using the scaling analysis (e.g. such as those presented in GV19 using the ratio of L_O

and L_E). In particular, the scaling results presented in Figure 4 of GV19 allows for determination of a value of Γ that is best for the measured flow conditions given a ratio of L_E to L_O. Analysis in Section 4.4.2 clearly shows that an assumption of local isotropy for the estimation of the rate of dissipation of kinetic energy dissipation using microstructure measurements may be reasonable. Using ϵ_{1D} only will bias turbulent diffusivity estimates by factor of 2-3 times as compared to multiple orders of magnitude if $\epsilon_{L_E/Th}$ is used. This again underscores how the common assumption of the equivalency between the Thorpe and Ozmidov scales to infer dissipation rates of turbulent kinetic energy is fundamentally flawed.

4.5 Concluding Remarks

The analyses presented here provide a systematic evaluation of the most common assumptions used in applications of the Osborn model. DNS data of homogeneous stratified turbulence have been used in manner that takes into direct consideration how the data from field measurements are used. Use of a constant value for the irreversible mixing coefficient combined with indirect inference of the kinetic energy dissipation rate from either the Thorpe (or Ellison) scale results in significant error in the estimations of the turbulent diffusivity. When compared to values calculated directly from the DNS data an assumption of local isotropy from microstructure measurements combined with a determination of a irreversible mixing coefficient value from suitable parameterizations should result in more accurate estimates of the turbulent diffusivity and hence a more appropriate way to use the Osborn model.

4.6 Summary

The Osborn model is widely used for quantifying diapycnal diffusivity K_ρ in oceanic flows. There are two main simplifications that are routinely made when using this model. First, a constant value of 0.2 is assumed for the mixing coefficient Γ. Second, the dissipation rates of turbulent kinetic energy ϵ are inferred using either the Thorpe (or Ellison) length scales or from microstructure measurements using the isotropy assumption. Data from direct numerical simulations of homogeneous stratified turbulence are used as a testbed to highlight impacts of these assumptions on estimates of K_ρ. A systematic analysis comparing inferred diffusivities to exact diffusivities as function of the turbulent Froude number Fr_t show that the use of a constant Γ results in an under-prediction of K_ρ by up to a factor of 5 for strongly stratified conditions (low Fr_t) and an over-prediction of K_ρ by up to two orders of magnitude in weakly stratified conditions (high Fr_t). The use of inferred dissipation rates ϵ derived from Thorpe/Ellison scales result in significant errors in estimates of K_ρ ranging from an over-prediction of one to two orders of magnitude in the low Fr_t regime to an under-prediction of several orders of magnitude for high Fr_t. However, the use of the isotropy assumption for estimating ϵ results in an over-prediction of K_ρ by no more than a factor of 2 for low Fr_t and converges on the exact K_ρ for $Fr_t \geq 1$. The implications of these findings for improved estimates of ocean mixing rates are discussed.

Chapter 5

Effect of Coriolis rotation on mixing efficiency[4]

5.1 Introduction

The amount of energy available for mixing at small scales has many important implications for oceanic and atmospheric flows. Mixing in geophysical flow helps to maintain the meridional overturning circulation and are used in estimations of the small scale fluxes that are used in mass budgets, heat budgets and the mixing of nutrients (Munk & Wunsch, 1998). Parameterizations of the eddy diffusivities of momentum (ν_t) and the scalar density (K_ρ) are commonly used in large scale models, but models can be sensitive to the accuracy of the parameterization (Garanaik & Venayagamoorthy, 2018). In order to be as accurate as possible these model parameterizations must account for all significant factors influencing mixing.

Density stratification is necessary for the existence of internal waves in the Earth's ocean and atmosphere but the degree of stratification has a direct impact on the amount of diapycnal mixing (Aguilar & Sutherland, 2006). A large body of work has analyzed turbulence and mixing in the presence of stratification (see Riley & Lindborg, 2013, Riley & Lelong, 2000 and references therein). Another important factor in the analysis of geophysical flows is the impact of planetary rotation. It is less clear what the impact this rotation has on small scale turbulent mixing, especially in a role that is coupled with stratification (Praud et al., 2006). The inclusion of rotation has led to increased study of inertial gravity waves and what is classified as rotating stratified turbulence (RST) (Pouquet et al., 2018; Rosenberg et al., 2017, 2016; Marino, Pouquet, & Rosenberg, 2015; Marino, Rosenberg, et al., 2015). An important question that has not been answered clearly is whether or not the inclusion of rotation will impact the existing parameterizations for the ir-

[4]The research presented in this chapter has been submitted to the Journal *Environmental Fluid Mechanics* under the title "Effect of rotation on mixing efficiency in homogeneous stratified turbulence using unforced direct numerical simulations" by M. R. Klema, S. K. Venayagamoorthy, A. Pouquet, D. Rosenberg and R. Marino. This chapter is written to reflect and acknowledge the contribution of the other authors.

reversible mixing efficiency in unforced stably stratified flows that mostly do not account for the rotation.

Direct numerical simulations (DNS) have been an important avenue for understanding stratified turbulence both with and without the influence of rotation (de Bruyn Kops, 2019; Pouquet et al., 2019, 2018; Rosenberg et al., 2017; Maffioli & Davidson, 2016; Rosenberg et al., 2016; Rorai et al., 2015; Marino et al., 2014, 2013; Brethouwer, Billant, Lindberg, & Chomaz, 2007; Waite & Bartello, 2006; Riley & de Bruyn Kops, 2003). Recent work using DNS has led to both some insights into and actual parameterizations of small-scale mixing (Garanaik & Venayagamoorthy, 2019; Maffioli et al., 2016a; Mater & Venayagamoorthy, 2014b; Lindborg & Brethouwer, 2008) by trying to answer questions about turbulent mixing in geophysical flows and demonstrating how DNS can be utilized in the broader study of geophysical flows. Some analysis of DNS with RST assert that there is an observable effect of rotation on the magnitude of potential energy available for mixing (Pouquet et al., 2018). Analysis of RST DNS has also shown that rotation and stratification are complementary in determining the relative strength of the direct and inverse energy cascades. Here, we use DNS simulations with rotation to help gain insight into irreversible (diapycnal) mixing and whether its inclusion in larger scale parameterizations of diapycnal mixing in stably stratified geophysical flows is needed for robust models.

Information and insights derived from numerical simulations is most useful when analyzed with thought to the complexity of laboratory and field observations. Applicability of any theoretical or numerical analysis is limited when it cannot be realistically tested or measured in a physical setting. However, making direct measurements of turbulent mixing in the field (in particular) is limited due to instrumentation capability and complications from internal wave motions that contaminate flux measurements (Gregg et al., 2018; Venayagamoorthy & Koseff, 2016). In oceanography, this has necessitated the use of indirect techniques to infer momentum and heat fluxes. As an example, the diapycnal diffusivity in a homogeneous and stationary flow can be defined as (Osborn, 1980):

$$\kappa_{\rho t} = \Gamma \frac{\epsilon}{N^2}, \tag{5.1}$$

where $\Gamma = \epsilon_P/\epsilon$ is an irreversible mixing coefficient, ϵ_P is the rate of potential energy dissipation, ϵ is the rate of kinetic energy dissipation and $N = \sqrt{(-g/\rho)(d\langle\rho\rangle/dz)}$ is the buoyancy frequency. All of the parameters in Eq. 5.1 are quantities that are readily available from a DNS. Determination of N and ϵ in the field requires simplifying assumptions such as local isotropy and choices on how the background density stratification is computed (Garanaik & Venayagamoorthy, 2018; Arthur et al., 2017), but it can generally be assumed that both N and ϵ are measurable in the physical setting. Γ has been assumed to have a constant canonical value of 0.2 (Osborn, 1980), but its constancy has been reviewed and challenged repeatedly (Gregg et al., 2018). Based on arguments in Venayagamoorthy & Koseff (2016), the irreversible definition of the mixing coefficient will be used exclusively herein.

Parameterizations for the mixing efficiency in geophysical flows are commonly based on one of three fundamental dimensionless parameters: the gradient Richardson number Ri (Venayagamoorthy & Koseff, 2016); the buoyancy Reynolds number Re_B (Salehipour & Peltier, 2015; Shih et al., 2005); and the turbulent Froude number Fr_t (Garanaik & Venayagamoorthy, 2019; Maffioli et al., 2016a). Rotational effects have not been included explicitly in the majority of mixing parameterizations of geophysical flows. The ratio of the buoyancy frequency N to the Coriolis rotational frequency f has been used to classify types of expected turbulent behavior and mixing and the importance of this ratio on geostrophic lateral mixing has been stressed by various researchers in RST (Lelong & Sundermeyer, 2005; Praud et al., 2006; Waite & Bartello, 2006; Kurien & Smith, 2014). N/f has been thought to dictate the behavior of flow development, as for example the orientation of shear layers, but neither the Rossby number nor N/f control the amount of kinetic and potential dissipation in stably stratified flows. The limited effects of rotation on turbulence in stably stratified flows has been noted (e.g. see Galperin et al. (1989); Kantha et al. (1989)), where effects of rotation impact regimes with convective or unstable flow dynamics. Despite this fact, scaling arguments using N/f and Ro_t see continuous application and use in the literature in conjunction with parameterizations of turbulence and turbulent mixing. Establishing a clear picture of whether irreversible mixing is impacted by rotation in stably stratified geophysical flows, drives this study. In what follows, a theoretical discussion on the key non-dimensional numbers is presented in section 5.2. Details of the numerical simulations and data are presented in section 5.3 followed by the results in section 5.4 and conclusions in section 5.5, respectively.

5.2 Theoretical Analysis

The amount of irreversible mixing in turbulent flows is a result of the dissipation of turbulent kinetic energy. The diapycnal (irreversible) mixing coefficient Γ is an instantaneous measure of how much of the turbulent kinetic energy is converted to background potential energy through dissipation (Garanaik & Venayagamoorthy, 2019). The buoyancy Reynolds number Re_B (also referred to as the Gibson number) is one of the most commonly used parameters for evaluating turbulent mixing since it can be calculated from field measurements (under certain assumptions such as isotropy at small scales) made in the atmosphere or ocean. Re_B is defined as

$$Re_B = \frac{\epsilon}{\nu N^2}, \tag{5.2}$$

where ν is the kinematic viscosity. However, despite its popularity, it has been noted that Re_B may be useful but insufficient as a single parameter to characterize mixing (Gregg et al., 2018; Mater & Venayagamoorthy, 2014a). Definitional ambiguity comes from the possibility to achieve the same value for the buoyancy Reynolds through various combinations of its constituent parameters (Mater & Venayagamoorthy, 2014b). Note that the diapycnal diffusivity can be recast as a function of Re_B in non-dimensional form as

$$\frac{\kappa_{\rho t}}{\nu} = \Gamma Re_B. \tag{5.3}$$

Eq. 5.3 implies that Re_B needs to be sufficiently large for smaller-scale turbulence to exist (Riley & Lindborg, 2013). It also shows how using Re_B to parameterize Γ might be ill-posed given that both of these quantities together define the diapycnal diffusivity. Given that the molecular diffusivities of scalars (salt and temperature) can vary by several orders of magnitude, it might be more appropriate to use a different dimensionless parameter for analyzing the degree of turbulent mixing of scalars as follows:

$$\hat{\kappa} = \frac{\kappa_{\rho t}}{\kappa} = \frac{\epsilon_P}{N^2 \kappa} = \Gamma Re_B Pr. \tag{5.4}$$

where κ is the molecular diffusivities of scalars in a given fluid, Pr is the molecular Prandtl (or Schmidt) number. Values for this diffusivity ratio parameter $\hat{\kappa}$ are readily computable from the DNS results, but harder to obtain in the field.

The turbulent Froude number gives a ratio of buoyancy effects to turbulent effects:

$$Fr_t = \frac{\epsilon}{Nk} \equiv \frac{1}{NT_L}, \tag{5.5}$$

where k is the turbulent kinetic energy. Fr_t may be the dimensionless parameter best suited to parameterize mixing in stratified turbulence (Shih et al., 2005; Ivey & Imberger, 1991). Difficulty in computing this number from measured quantities has limited its application in the field setting but it has seen widespread use in numerical simulation analysis (Pouquet et al., 2018; Maffioli & Davidson, 2016). Recent work has shown a link between the mixing efficiency and Fr_t (Garanaik & Venayagamoorthy, 2019; Pouquet et al., 2018; Feraco et al., 2018). The work by Garanaik & Venayagamoorthy (2019) is specifically designed to show how the link between Γ and Fr_t can be used by researchers analyzing data measured in the field. The degree of stratification and turbulence are both contained in the definition of the turbulent Froude number and represent the two processes having the greatest influence on the evolution of the flow (Maffioli & Davidson, 2016; Lindborg & Brethouwer, 2008). In particular the definition of the turbulent time scale ($T_L = k/\epsilon$) is contained within this parameter, which is a measure of the decay time of turbulent kinetic energy (Venayagamoorthy & Stretch, 2010). In this light, Fr_t can also be viewed as the competition between the buoyancy time scale $\sim N^{-1}$ and the turbulent time scale T_L.

Analogous to the turbulent Froude number, the turbulent Rossby number defines the relative strength of rotational to turbulent effects, again, also in terms of time-scales:

$$Ro_t = \frac{\epsilon}{fk} = \frac{1}{fT_L}. \tag{5.6}$$

Using Fr_t and Ro_t as the two key parameters for the presentation of simulation results allows for evaluation of the relative impact of varied levels of stratification and rotation on the behavior of irreversible mixing in simulated geophysical flows. We will use Re_B and $\hat{\kappa}$ as the two key diagnostic parameters to both evaluate and ensure that small scale irreversible mixing does indeed exist in the data analyzed.

5.3 Simulations and Data

Direct numerical simulations of the non-dimensional Boussinesq equations with rotation, Eqs 5.7 and 5.8, were made using the Geophysical High-Order Suite for Turbulence (GHOST) code (see Mininni et al. (2011) for details). GHOST is a pseudo-spectral computational fluid framework that is parallelized using a hybrid MPI/OpenMP/CUDA scheme and has demonstrated excellent scalability and performance to over 130,000 computational nodes (Rosenberg et al., 2015). A new version of the code includes the possibility of non-cubic boxes and of non-periodic boundary conditions in one direction (Sujovolsky et al., 2018; Fontana et al., 2020).

$$\partial_t \mathbf{u} - \nu\Delta\mathbf{u} + N\theta\hat{z} + \nabla p - f\mathbf{u}\times\hat{z} = -\mathbf{u}\cdot\nabla\mathbf{u} \tag{5.7}$$

$$\partial_t\theta - \kappa\Delta\theta - Nw = -\mathbf{u}\cdot\nabla\theta \tag{5.8}$$

All simulations were made using 1024^3 grid points in a triply periodic box. Simulations 1-10 in Table 5.1 all have velocity initialized at large scales with a superposition of Taylor-Green vortices, as has been done for stratified flows in other studies (Sujovolsky et al., 2018; Hebert & de Bruyn Kops, 2006). Initialization with Taylor-Green vortices primes the development of rotational flow structures within a simulation, rather then having rotational structures forced to develop from

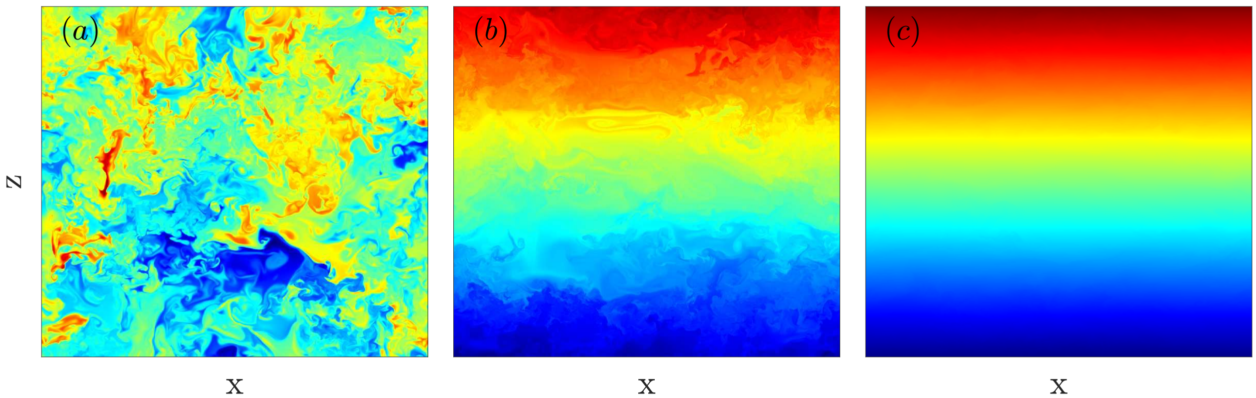

Figure 5.1: Vertical plane visualization of three simulations using the scalar field in the center ($y = \pi$) of the periodic box at or near the peak of dissipation rate of the turbulent kinetic energy. All three simulations have the same rotational frequency ($f = 0.04$) but the stratification increases from left-to-right, $N = 0.2$, $N = 1.6$ and $N = 5.5$ respectively. The corresponding turbulent Froude number also varies by an order of magnitude between the simulations as a result: $Fr_t = 2.035$, $Fr_t = 0.18$ and $Fr_t = 0.02$. The red-to-blue colors represents the continual change from lighter to heavier fluid.

random initial conditions. The impact of rotation on the irreversible mixing coefficient should be most apparent in these ten simulation if it is influencing scalings via Fr_t and Ro_t.

Simulations 11-30 are initialized with randomized phases in Fourier space. These twenty simulations are a subset of the randomly initialized runs previously presented and analyzed (Pouquet et al., 2018; Rosenberg et al., 2016). There are no initial scalar fluctuations with either initialization. This setup allows for the buoyancy fluctuations to develop from the internal dynamics of the Boussinesq equations (Rosenberg et al., 2016). Inputs to all simulations were varied by specification of the buoyancy frequency N, Coriolis rotation f, kinematic viscosity ν, molecular diffusivity κ (always maintaining a Prandtl number, $Pr = \nu/\kappa$, equal to 1) and the evolutionary time step. No mean shear or other forcing was imposed in the simulations; hence, the energy decays over the course of a simulation. A total of thirty DNS runs using the GHOST code are presented and evaluated to study the effect of rotation on irreversible mixing. Table 5.1 gives the details of all simulations in this analysis. Fig 5.1 shows a two-dimensional snapshot of three simulations at or near the peak of dissipation rate of turbulent kinetic energy in the vertical plane at the center ($y = \pi$) of the periodic box. This snapshot of the vertical cross-section show the instabilities of the flow using the scalar field for runs 14, 18 and 22. All three of these simulations have the

Table 5.1: Details of the 30 simulations, where the Froude, Rossby and buoyancy Reynolds numbers are calculated at the peak of dissipation rate of turbulent kinetic energy. The initial Reynolds number is given by $Re_0 = U_0 L_0/\nu$ where the initial characteristic length and velocity scales are given by $L_0 = 1$ and $U_0 = 1$ respectively. [1] denotes a data subset also analyzed in Pouquet et al. (2018), with reference identification ID.

Run	$N(s^{-1})$	$f(s^{-1})$	N/f	$\nu(m^2s^{-1})$	Fr_t	Ro_t	Re_B	Re_0	JFM ID
1	0.7	0.13	5	$4.50E{-}4$	0.78	3.87	791	2222	-
2	5.0	1.00	5	$3.00E{-}4$	0.06	0.31	10	3333	-
3	2.7	0.38	7	$2.50E{-}4$	0.13	0.91	59	4000	-
4	0.4	0.02	20	$1.00E{-}4$	1.54	30.75	12740	10000	-
5	0.5	0.40	1.25	$1.50E{-}4$	1.22	1.53	5004	6667	-
6	1.0	0.80	1.25	$1.75E{-}4$	0.49	0.62	894	5714	-
7	2.0	1.60	1.25	$1.25E - 4$	0.20	0.25	254	8000	-
8	1.0	1.00	1	$1.50E{-}4$	0.50	0.50	1057	6667	-
9	1.0	0.40	2.5	$1.50E{-}4$	0.60	1.50	1279	6667	-
10	2.5	0.25	10	$1.25E{-}4$	0.27	2.56	263	8000	-
11[1]	1.0	0.01	106	$5.50E{-}4$	0.28	30.03	110	1818	JFM54
12[1]	1.9	0.01	199	$5.50E{-}4$	0.11	22.39	27	1818	JFM37
13[1]	0.1	0.04	2.5	$2.70E{-}4$	4.25	10.62	48886	3704	JFM61
14[1]	0.2	0.04	5	$2.70E{-}4$	2.035	10.18	10851	3704	JFM60
15[1]	0.4	0.04	10	$1.54E{-}4$	1.034	10.34	4035	6494	JFM59
16[1]	0.8	0.04	20	$1.54E{-}4$	0.473	9.46	893	6494	JFM56
17[1]	1.2	0.04	30	$1.50E{-}4$	0.29	8.56	384	6667	JFM53
18[1]	1.6	0.04	40	$1.50E{-}4$	0.18	7.11	194	6667	JFM51
19[1]	2.0	0.04	50	$1.50E{-}4$	0.13	6.30	110	6667	JFM49
20[1]	2.4	0.04	60	$1.50E{-}4$	0.09	5.36	69	6667	JFM46
21[1]	3.8	0.04	94	$1.50E{-}4$	0.04	3.43	20	6667	JFM39
22[1]	5.5	0.04	138	$1.50E{-}4$	0.02	2.11	6	6667	JFM31
23[1]	3.8	0.05	69	$1.00E{-}4$	0.04	2.57	30	10000	JFM41
24[1]	2.0	0.04	25	$1.50E{-}4$	0.13	3.13	109	6667	JFM48
25[1]	4.0	0.08	50	$1.50E{-}4$	0.03	1.60	16	6667	JFM35
26[1]	0.7	0.27	2.6	$2.10E{-}4$	0.53	1.33	817	4762	JFM57
27[1]	1.3	0.54	2.5	$2.10E{-}4$	0.24	0.58	200	4762	JFM52
28[1]	2.7	0.54	4.9	$2.10E{-}4$	0.07	0.33	34	4762	JFM43
29[1]	3.8	0.75	5.0	$1.50E{-}4$	0.03	0.16	17	4762	JFM33
30[1]	2.7	1.07	2.5	$2.10E{-}4$	0.06	0.14	29	4762	JFM42

same imposed rotation ($f = 0.04$) but the stratification increases in the simulations presented from left-to-right. It is clear from these visualizations that the vertical motions decrease with increasing stratification.

5.4 Results

5.4.1 Energy and Dissipation

Influences of rotation are commonly visible in geophysical flows at the energy containing scales and these scales are thus influenced by rotation. Examples of the evolution of simulation integrated energy and dissipation rate are shown in Fig 5.2. Fig 5.2a shows this evolution of run 14 (dashed lines), run 18 (dash-dot lines) and run 22 (dotted lines), respectively. Dissipation rates from these simulations were indirectly calculated using simulation enstrophy, see (Pouquet et al., 2018; Rosenberg et al., 2016; Mininni et al., 2011) for details. These are the same simulations visualized in Fig 5.1. As the stratification increases there is a visible increase in the oscillatory transfer of energy between the kinetic (green) and potential (blue) modes. It is also clear that increases in the stratification lowers the turbulent dissipation rate (magenta). Fig 5.2b shows simulations runs 21, 25 and 29 where the buoyancy frequency of the simulations are similar ($N = 3.8 - 4.0$) between the runs and the value for f is varied. Unlike variations of N, variations of f do not significantly influence the behavior of energy or dissipation rate in the simulations. These results are consistent with the results of simulation runs 9, 6 and 8 (not shown here) where $N = 1$ in all three simulations but rotation of the runs is $f = 0.4$, $f = 0.8$ and $f = 1$ respectively. It is apparent from these simple diagnostics that f does not appear to have a noticeable influence on the energetics (especially on the dissipation rates) in stably stratified flows. Clearly the magnitude of the rotational parameter is an order of magnitude, or less, than the buoyancy parameter for the runs in Fig 5.2b. This likely limits the influence of f as compared to N on the flow. The relative magnitudes of these parameters in the simulations was chosen in order to maintain their relevance to N/f values seen in geophysical flows and will be explained in more detail in the following section.

5.4.2 Parametric Space

Fig 5.3 plots a portion of time series data from all 30 of the runs analyzed in this study as discrete values. Data plotted for each run shows parameter values at 12 different times starting at the

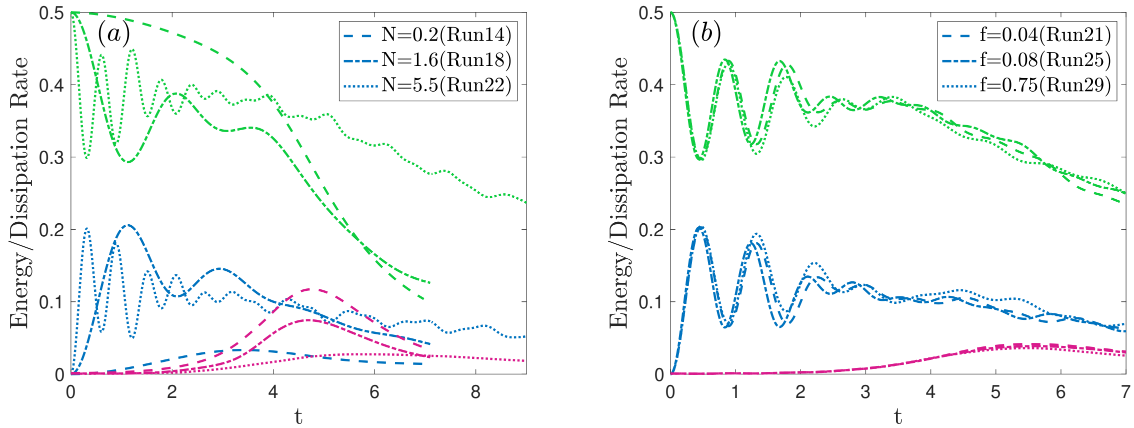

Figure 5.2: Temporal simulation evolution of volume integrated kinetic energy k (green), potential energy (blue), and the kinetic energy dissipation rate ϵ (magenta) for runs (a) at a constant rotation $f = 0.04$ and (b) at approximately constant stratification, $N = 3.8 - 4.0$ (see Table 5.1).

time of the peak of the dissipation rate of turbulent kinetic energy. These 12 data points are equally time-spaced values over this interval with the intermediate between each point simply removed for visualization. These sub-sets of the data are presented in a Fr_t-Ro_t parametric framework. The runs can be easily distinguished. They all evolve from a higher to a lower value of Re_B, because of self-similar energy dissipation (see Rorai et al. (2015) for the purely stratified case). Any given simulation, as expected, follows the lines of constant N/f. Also, the magnitudes of Fr_t and Ro_t evolve over the course of the simulations due to turbulent dissipation. As the magnitudes of Ro_t and Fr_t decrease, the increase in stratification will limit the amount of turbulence and mixing, especially vertically (see Fig 5.1).

Work presented by (Mater & Venayagamoorthy, 2014b) uses a multiple parameter framework evaluates the dominant flow regimes in stratified shear flows. This new parametric framework uses this same idea of using a multi-parameter framework but to define dominant flow regimes that include rotation but with an absence of imposed shear. Fig 5.3 clearly shows how the relative magnitudes of rotation and stratification are coupled in the geophysical context along lines of constant N/f. All flows in this parametric space evolve, as noted above, where values of $N/f \sim 100$ are commonly seen in the atmosphere and $N/f \leq 10$ is appropriate for the oceanic setting. The parametric space is divided into four different regions using O(1) magnitudes of Fr_t and Ro_t as delineations and the nomenclature of Aluie & Kurien (2011) for classification. In region 1 the magnitudes of the rotation and stratification are small and of comparable magnitude so this quadrant of the graph is denoted by rs. While there is an influence of stratification and rotation in this region the flow behavior likely approximates the behavior of classical turbulence since their effects are negligible (i.e. high Fr_t and high Ro_t). In region 2 the stratification is approximately an order of magnitude greater than the rotation and is denoted rS (low Ft_t, high Ro_t). Rotation and stratification are both significant and have similar magnitudes in region 3, RS. Region 4 denotes an area in the parametric framework where the rotation is a least an order of magnitude greater than the stratification, Rs. The majority of geophysical flows are classified as falling along one of the N/f lines denoted therefore none of the simulations fall into region 4 where $N/f < 1$. Flows that fall into this classification region may be relevant in astrophysics, for example for stars that are rotating rapidly, but are not seen except in specific isolated cases in the geophysical setting. The magnitude of rotation in these simulations ($Ro_t \geq 0.1$) would be considered weakly rotating except in certain specific contexts (i.e. Ecke & Niemela (2014)). Increasing the amount of rotation to reach an order of magnitude where $Ro_t \leq 0.01$ and maintaining N/f relevant to the geophysical setting would also necessitate an increase in N, which would lead to simulations results with Reynolds numbers too low to be considered turbulent.

Data in Fig 5.3a is colored by the buoyancy Reynolds number in order to illustrate one of the common measures of turbulent mixing. In the plots, values for the buoyancy Reynolds number are limited to $O(1)$ or greater, which eliminates inclusion of viscosity affected (low Reynolds number) flows. From these results, it can be easily seen that the ratio of N/f is not a useful diagnostic tool for explicitly determining levels of turbulent mixing. Re_B values vary by up to three orders of magnitude on multiple N/f lines. Additionally, the turbulent Froude number can also be observed to take almost any value in the rS and RS regimes for any given N/f. These observations point to the fact that while both N and f influence the flow, it is clear from this framework that their ratio does not provide a diagnostic signature for the levels of irreversible mixing in RST in the absence of forcing.

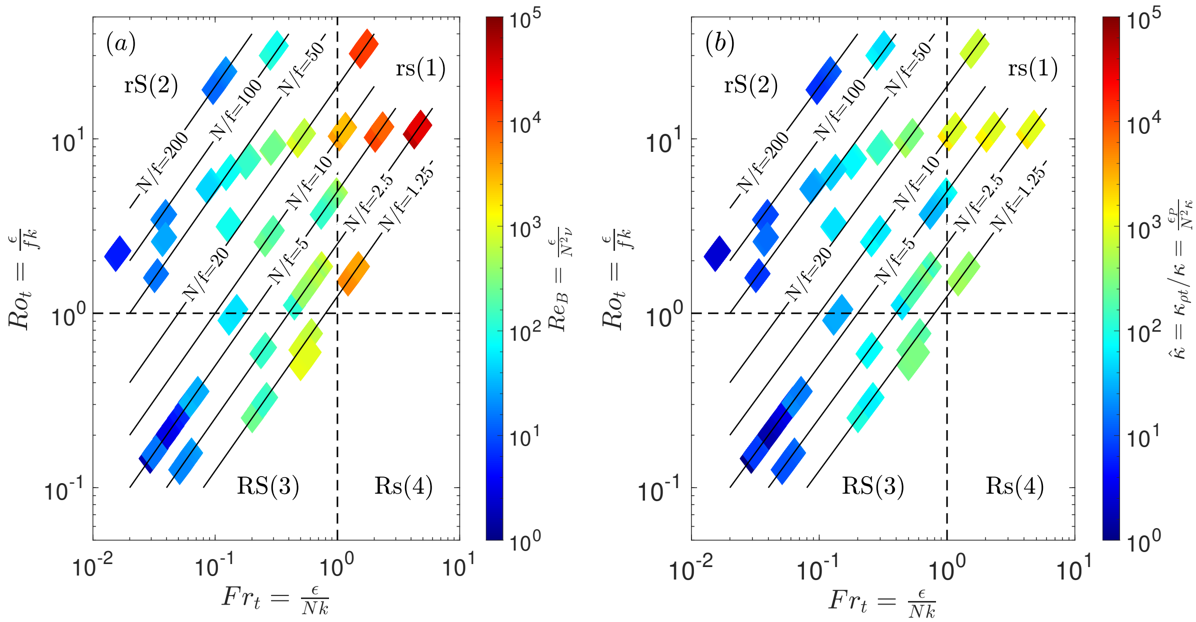

Figure 5.3: Time series plots of the runs in a parametric framework using Fr_t and Ro_t. Data is colored by Re_B (a) and by the diffusivity ratio $\hat{\kappa}$ (b), see Eqs. 5.2 and 5.4, respectively.

Fig 5.3b shows the same data as in Fig 5.3a, but the data is now colored by the diffusivity ratio $\hat{\kappa}$ whose values are also constrained to $O(1)$ or greater to exclude data dominated by molecular mixing effects. DNS results that do not report a value for $\hat{\kappa}$ that is at least $O(1)$ have mixing mostly, if not exclusively, due to molecular diffusion. It has been shown that the background mixing in the ocean is of $O(10)$(Munk & Wunsch, 1998) and these simulations have been designed to be comparable to physically realistic flows. DNS data where $\hat{\kappa} < O(1)$ may introduce non-physical data where the molecular diffusion is the same order of magnitude, or larger, than the turbulent diffusion. Run 22 is an example of a run that is near this threshold. Overall, the same observations and conclusions can be made about the ambiguity of N/f as a diagnostic tool. Some of the results in this plot show values for $\hat{\kappa}$ that would suggest limited amounts of mixing when compared to the data evaluated using Re_B that suggest more significant levels of mixing. This illustrates the importance of using multiple parameters and criteria for the evaluation of mixing in DNS data. This theoretical framework (Fr_t, Ro_t) provides a useful diagnostic for classifying RST DNS for geophysical flow regimes and could also be applied to measured data if parameterizations to determine Fr_t from measurable quantities are used as proposed by (Garanaik & Venayagamoorthy, 2019).

5.4.3 Irreversible Mixing

Fig 5.4 presents the parameterization of Γ as function of Fr_t for the RST runs plotted together with the non-rotating DNS data presented in Garanaik & Venayagamoorthy (2019): sheared unstratified Shih et al. (2005), forced stratified (Maffioli et al., 2016a) and unforced stratified runs (Garanaik & Venayagamoorthy, 2019).The remarkable feature is that the scaling relationship between Γ and Fr_t presented in (Garanaik & Venayagamoorthy, 2019) holds well despite the fact that f does not appear evidently in Fr_t. An increase in the irreversible mixing efficiency for $Fr_t \sim 0.1$ seen in some studies is not observed. While the presence of rotation may provide additional energy at scales comparable to and larger than the energy-containing scales in a stratified flow, it does not appear to have any discernible effect on the scaling of the diapycnal (small-scale) irreversible mixing coefficient. It can also be seen in Fig 5.4 that the distribution of Re_B covers six orders of magnitude and more importantly, Re_B can vary by over an order of magnitude for any given value of Γ, reinforcing previous research showing the ambiguity of Re_B. As previously noted in Garanaik & Venayagamoorthy (2019) it is clear that a unique scaling of Γ with Re_B is not possible. These results extend that observation to data that includes the influence of rotation.

5.5 Concluding Remarks

This paper analyzes scaling properties of homogeneous, decaying and rotating stratified turbulent mixing through the irreversible mixing parameter Γ. A new parametric framework using Fr_t and Ro_t is used to show how the relative magnitudes of rotation and stratification present in geophysical flow regimes of the Earth's ocean and atmosphere affect flow statistics. DNS data is plotted within the framework using Re_B and $\hat{\kappa}$ as diagnostics of the degree of irreversible turbulent mixing. The diffusivity ratio $\hat{\kappa}$ in the simulations are realistic to physical values and is suggested as a more robust parameter than Re_B for evaluating the degree of mixing in DNS. Variations in Re_B

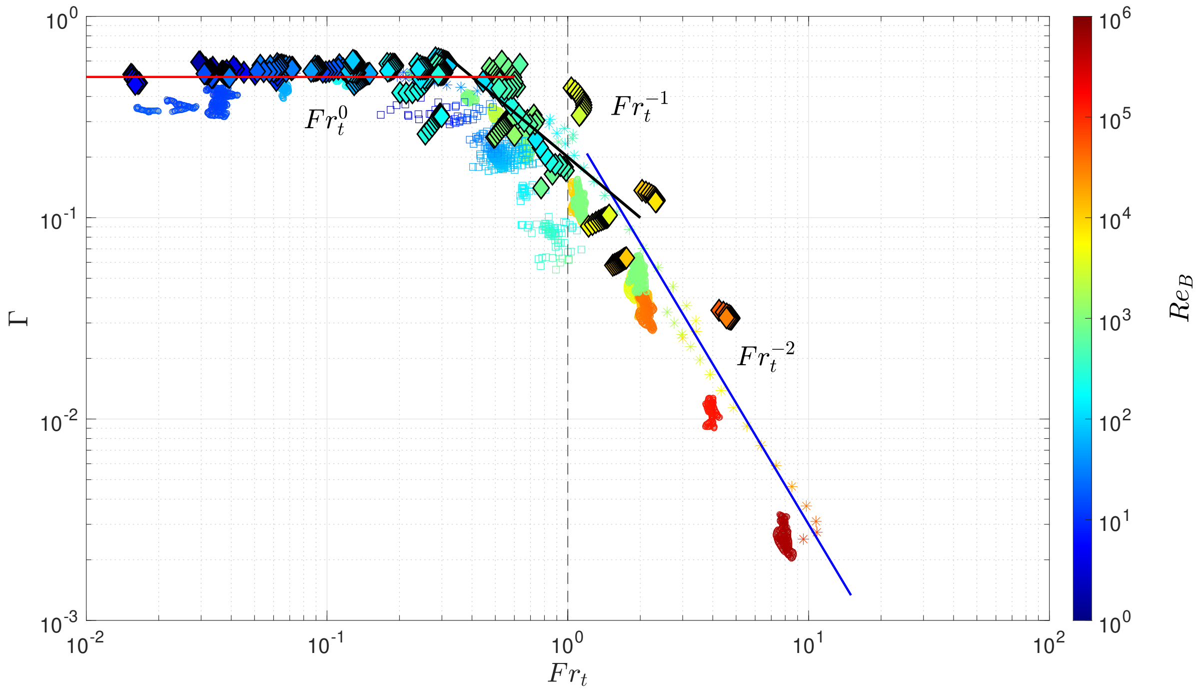

Figure 5.4: Irreversible mixing coefficient Γ as a function of turbulent Froude number Fr_t. The color bar at right indicates values of Re_B. Diamond: decaying RST DNS; star: decaying stratified turbulence (Garanaik & Venayagamoorthy, 2019); circle: forced DNS (Maffioli et al., 2016a); square: sheared DNS data (Shih et al., 2005)

and $\hat{\kappa}$ for any given value of N/f clearly show that N/f does not have any unique relationship to the amount of diapycnal mixing in stable decaying RST. Significant variations in the magnitude of both Fr_t and Ro_t for any given N/f are also observed, supporting this conclusion. RST data from this study plotted with non-rotating but stratified DNS data show remarkable agreement in the scaling relationship between the irreversible mixing coefficient and the turbulent Froude number.

Rotation has been clearly observed to influence the large scale flow structures that develop in some geophysical flows and simulations. The inclusion of rotation may also influence kinetic and potential dissipation rates individually. However, rotation does not appear to have a direct influence on their ratio, the irreversible mixing efficiency parameter in the absence of forcing (at the intermediate scale). Additionally, it is clear from this analysis that existing parameterizations between the irreversible mixing coefficient Γ and the turbulent Froude number Fr_t are applicable to unforced RST.

5.6 Summary

Diapycnal (irreversible) mixing is analyzed using thirty high resolution direct numerical simulations of homogeneous rotating stratified turbulence (RST) in the absence of imposed shear or forcing. The influence of varied rotation and stratification on the energetics (in particular the dissipation rates of kinetic and potential energies) is presented. Data is also presented in a new parametric framework using the turbulent Froude and Rossby numbers $Fr_t = \epsilon/Nk$, $Ro_t = \epsilon/fk$, where k is the turbulent kinetic energy, ϵ its rate of dissipation, N the buoyancy frequency and f the Coriolis parameter. This framework is used to illustrate relative magnitudes of the stratification and rotation in geophysical flows and provide a useful tool for explicating the relationship between Fr_t and Ro_t. Results indicate that unforced rotation does not impact the magnitude of the irreversible mixing coefficient ($\Gamma = \epsilon_P/\epsilon$) when compared to results without rotation, where ϵ_P is the rate of potential energy dissipation. Moreover, it is shown that the recent scaling laws for mixing efficiency in stably stratified turbulence in the absence of rotation, as exemplified in Garanaik & Venayagamoorthy (*J. Fluid Mech.* 867, 2019, pp. 323-333), are applicable as well for homogeneous and decaying RST. Results also highlight the ambiguity of the ratio N/f as a control parameter for the classification of small-scale RST, and thus for evaluating diapycnal mixing.

Chapter 6

Numerical simulations of internal wave interactions with topographic ridges[5]

6.1 Introduction

In oceanography the study of the interactions of internal waves with topography is an area of research that sees continual attention. Thought to be one of the main sources of sustained ocean mixing, understanding the process and flow structures that develops as a result of this interaction remains important (Munk & Wunsch, 1998). Surface tides and wind create sources of mechanical energy that can convert to internal waves (St. Laurent & Garrett, 2002; Wunsch & Ferrari, 2004; Garrett & Kunze, 2007). Field measurements have confirmed the significant amounts of turbulent mixing occurs as a result of the internal wave field interacting with oceanic ridges and seamounts (Munk & Wunsch, 1998; Kunze & Smith, 2004; Polzin, 2009; Ledwell et al., 2011). The dynamics resulting from this interaction converts energy from the internal wave field and may be the main source available for vertical mixing of the water column, resulting in flow gradients that drive global oceanic circulation. Understanding of these processes has been bolstered by an increasing knowledge of baroclinic tide generation (Althaus et al., 2003; Nash et al., 2004; Carter et al., 2005; Garrett & Kunze, 2007) where low first-mode internal waves allow for propagation of energy far from the source (Ray & Mitchum, 1996; Alford et al., 2007) as well theoretical modeling (Bell, 1975; Balmforth et al., 2002; Llewellyn Smith & Young, 2002; St. Laurent & Garrett, 2002; Khatiwala, 2003).

Non-linear internal waves (NLIWs) have been observed and measured near topographic features (Scotti & Pineda, 2004; Carter et al., 2005; Klymak et al., 2006). Internal waves can be

[5]The research presented in this chapter is under preparation to be submitted to the Journal *Journal of Fluid Mechanics* under the title “Numerical simulations of internal wave interactions with topographic ridges" by M. R. Klema and S. K. Venayagamoorthy. This chapter is written to reflect and acknowledge the contribution of the other author.

generated from wave-wave interactions (Nikurashin & Legg, 2011), lee-wave release resulting from a changing internal tide (Gayen & Sarkar, 2011) and from the interaction of these first-mode internal tides with topography (Klymak et al., 2006; Levine & Boyd, 2006). Despite having observations and measurement of these features questions remain about the development, evolution and fate of internal waves due to the difficulty of field measurement and making direct observations (Vlasenko & Hutter, 2002). Furthering our understanding of non-linear internal wave dynamics has implications for our understanding of the processes that drive energy transport and mixing in oceanography.

Theory describing NLIWs is almost entirely derived from weakly nonlinear wave formulations based on the Korteweg-de Vries equation and asymptotic expansions (Thorpe & Haines, 1987; Dauxois et al., 2004). Large amplitude turbulent overturns produced by internal wave interaction with topography are not well represented by this approach. Breaking non-linear internal waves occur when topography is encountered that has a slope that matches the internal wave group velocity as described by Phillips (1977). In addition to field observations, numerous laboratory studies have been performed to observe and measure the interaction of an internal wave with topography (Cacchione & Wunsch, 1974; Ivey & Nokes, 1989; Ivey et al., 2000). This process has also been studied using computational fluid dynamics (CFD), direct numerical simulations that resolve the turbulent processes (Slinn & Riley, 1998; Javam et al., 1999; Venayagamoorthy, 2006) and large field scale simulations (Klymak et al., 2012; Legg, 2014; Jalali & Sarkar, 2017) that focus on the bulk flow behavior.

Overturning that can result from such interactions in stratified flows lead directly to mixing and the dissipation of energy. Studies using CFD to study the internal wave-topography interactions are increasingly prevalent. Venayagamoorthy (2006) considered the generation of upslope propagating bores leading directly to dissipation and mixing for a variety of wave forcing and slope steepness. Legg & Adcroft (2003) completed Reynolds-averaged Navier-Stokes (RANS) simulation of field scale topography with slopes of various monotonic shapes. Study using numerical modeling of this interaction has be completed for subcritical and critical slope cases (Legg, 2014) as well as for critical and supercritical cases (Klymak et al., 2012; Hall et al., 2013). The majority of the numerical simulations studying this interaction process have been completed at the field scale, a scale that often does not directly produce the turbulent quantities or resolve the structure of the flow.

This research presents the results of two-dimensional numerical simulations of the interaction of a first-mode internal wave field with a topographic ridge meant to emulate oceanic ridges found around the globe and are recognized hot-spots for turbulent mixing (Munk & Wunsch, 1998). The emphasis is to investigate the partition and flux of energy from internal wave interaction with a series of topographic ridges with varying height and slope steepness. Additionally these simulations are completed at an intermediate simulations scale that allow for some flow structures that develop as a result of the interaction to be resolved but at a much larger scale than they have been simulated. This analysis aims to provide a needed bridge between the highly resolved direct numerical simulations (DNS) of flows at the laboratory scale and the Reynolds-averaged Navier-Stokes (RANS) simulations generally used for simulation of internal waves at the field scale. The numerical method and simulations setup is discussed in Sec. 6.2, the energetics of the topography-wave interaction in Sec. 6.3 and the conclusions in Sec. 6.4.

6.2 Formulation and Numerical Methods

The Navier-Stokes equations with the Boussinesq approximation and a constant kinematic viscosity ν are given by

$$\frac{\partial \mathbf{u}}{\partial t} + \mathbf{u} \cdot \nabla \mathbf{u} = -\frac{1}{\rho_0} \nabla p + \nu \nabla^2 \mathbf{u} - \frac{g}{\rho_0} \rho \mathbf{k}, \tag{6.1}$$

where $\mathbf{u} = (u, v, w)$ is the three dimensional velocity field, ρ_0 is a reference density, p is the pressure, g is gravitational acceleration and $\mathbf{k}$ is the unit normal vector in the vertical direction. Solutions to Eq. (6.1) are subject to the continuity constraint given by Eq. (6.2),

$$\nabla \cdot \mathbf{u} = 0. \tag{6.2}$$

In stratified flow the density field is coupled to the flow field and therefore Eqs. (6.1) and Eq. (6.3), the scalar (density) transport equation, must be solved simultaneously

$$\frac{\partial \rho}{\partial t} + \nabla \cdot (\rho \mathbf{u}) = \kappa \nabla^2 \rho, \tag{6.3}$$

where κ is the thermal diffusivity (constant). Equations (6.1), (6.2) and (6.3) are computed using Massachusetts Institute of Technology's General Circulation Model (MITgcm) code within the two-dimensional (x, z) domain depicted in Figure 6.1. This CFD code has been extensively used and validated for simulations of stratified geophysical flows (e.g. Legg & Adcroft, 2003; Klymak et al., 2012; Legg, 2014; Musgrave et al., 2016). The depth of the domain is 10m and the length of the domain 100m. This size domain was chosen in order to fill a gap between the laboratory scale, $O(10\ m)$, and full field scale simulations, $O(1000\ m)$, most often completed. Domain resolution of $\Delta x = \Delta z = 0.05\ m$ in the horizontal and vertical directions, respectively, result in a total of $nx \times ny = 2800 \times 200$, or $560,000$ total grid points. This resolution, while not resolving all turbulent structures, allows for realistic turbulent flow structures to develop.

Initial stratification for all simulations is defined using a linear background distribution ρ_b given by

$$\frac{\rho(z, t=0)}{\rho_0} - 1 = \frac{\rho_b(z)}{\rho_0} = -\frac{\Delta \rho}{\rho_0} \left(\frac{z}{d}\right), \tag{6.4}$$

where $\Delta \rho / \rho_0 = 0.002$ results in a buoyancy frequency $N = 0.01\ s^{-1}$. At the left boundary of the computational domain simulations are forced with a first-mode internal wave given by

$$u(0, z, t) = U_0 cos(mz) sin(\omega t), \tag{6.5}$$

where U_0 is the velocity amplitude of forcing, m is the vertical wave number corresponding to a mode-1 baroclinic wave with $m = \pi/d$, ω is the forcing frequency, and u is the velocity component. An Orlanski radiative boundary condition is applied at the right hand boundary to allow the propagation of the internal wave energy out of the domain. Free slip boundary conditions are applied on both sides of the computational domain. On the bottom boundary a no-slip boundary condition is applied. At the top of the domain a linearized free surface boundary condition is applied that allows nonzero vertical motions (denoted η), which results in a contribution to the pressure from the boundary displacement. A Prandtl number of $Pr = 1$ for all simulations is set by prescribing a kinematic viscosity of $\nu = 10^{-5}\ m^2\ s^{-1}$ and a thermal diffusivity of $\kappa = 10^{-5}\ m^2\ s^{-1}$. Setting these values for the kinematic viscosity and thermal diffusivity near to the accepted magnitude allow for the large energy containing flow structures to resolve similar to a CFD large eddy simulation (LES).

6.3 Energetics

Internal waves contain phase-locked downward and upward propagating wave beams that are characterized by both vertical and horizontal wave numbers, m and k respectively, where the wave modes propagate horizontally. When an internal wave encounters topography the upward and downward beams decouple and the beam individually interact with the topography and change the dynamics of the flow. The dynamic interaction of the internal waves and topography is impacted by both the slope of the topography, γ and the slope of the wave beam, s, defined by

$$s = tan\theta = \frac{k}{m} = \left(\frac{\omega^2 - f^2}{N^2 - \omega^2}\right)^{1/2}, \tag{6.6}$$

where θ is the angle of the internal wave characteristic, ω is the wave frequency, f is twice the sine of the latitude Coriolis parameter and N is the buoyancy frequency. It is common to see bottom slope define by the ratio of γ and s (Phillips, 1977). When the topographic slope is steeper than the wave characteristic slope $\gamma/s > 1$ and the slope is classified as supercritical. Subcritical slopes correspond to $\gamma/s < 1$ and $\gamma/s = 1$ define critical slopes. Critical slopes mean that the wave's angle of propagation matches the slope of the topography.

In a uniformly stratified fluid linear first-mode internal waves propagate horizontally at the speed defined by

$$c_{ph} = \frac{\omega}{k} = \frac{d}{\pi}\left(N^2 - \omega^2\right)^{1/2}, \tag{6.7}$$

where d is the fixed depth. Table 6.1 give the details of the simulations completed for the this analysis, where different values of the topographic slope for different simulations allowed for variation of γ/s from 0 to 1.5 while holding N, ω and s at fixed values. The range of subcritical-to-supercritical slopes was achieved by variation of γ using the topographic ridge height, h_t, resulting in a change to the corresponding width, W_t. Velocity amplitudes is varied between $0.3\ cm\ s^{-1}$ and $2.5\ cm\ s^{-1}$ resulting in Froude numbers ($Fr = U_0/c_{ph}$) between 0.1 and 0.84. This parameter space represents a wide range of wave energy conditions and allows for assessment of various conditions resulting from linear to highly non-linear internal waves interacting with topography. A schematic of the computational domain and the relevant parameters associated with the simulation domain are shown in Fig. 6.1.

6.3.1 Temperature/Density And Velocity Fields

Time series snapshots of internal wave propagation through the computational domain is shown in Fig. 6.2. Three simulation cases are shown in this figure, $Fr = 0.1$, $Fr = 0.5$ and $Fr = 0.84$. Values for the relative slope $\gamma/s = 1$ and topography-to-depth ratio h_t/d are consistent for the simulations depicted. Also for all three simulations the frequency of the incoming internal wave is

Table 6.1: Details of the 40 simulations, including the parameter space covered.

Runs	γ/s	$Fr = U_0/c_{ph}$	$U_0T/(\pi L_s)$	ht/d	$Comments$
1-5	0	0.1-0.84	-	-	No-slope cases
6-8	0.25	0.1-0.84	0.03-0.27	0.5	Subcritical cases
9-11	0.5	0.1-0.84	0.06-0.52	0.5	Subcritical cases
12-16	1	0.1-0.84	0.12-1.03	0.5	Critical cases
17-19	1	0.25-0.84	0.62-2.06	0.25	Critical cases
20-23	1	0.5-0.84	0.24-0.67	0.75	Critical cases
24-26	1.25	0.1-0.84	0.29-2.43	0.25	Supercritical cases
27-29	1.25	0.1-0.84	0.15-1.21	0.5	Supercritical cases
30-32	1.25	0.1-0.84	0.1-0.81	0.75	Supercritical cases
33-35	1.5	0.1-0.84	0.33-2.78	0.25	Supercritical cases
36-38	1.5	0.1-0.84	0.17-1.39	0.5	Supercritical cases
39-40	1.5	0.5-0.84	0.56-1.39	0.75	Supercritical cases

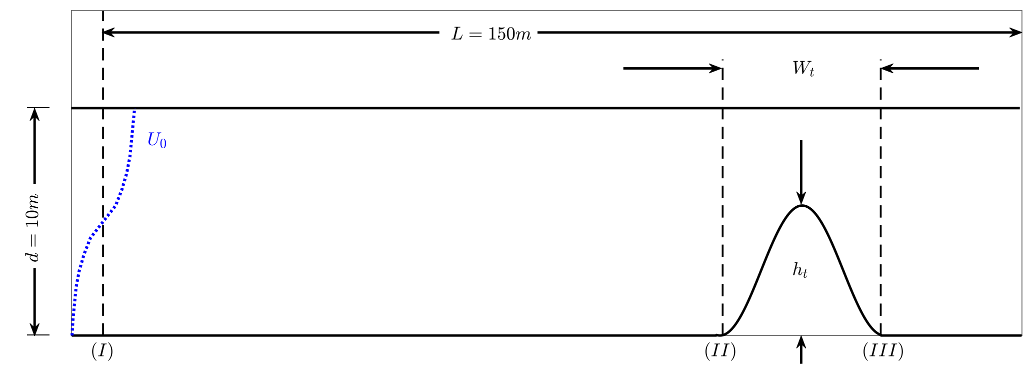

Figure 6.1: Schematic of the computational domain for the simulations presented. Lines (I), (II) and (III) are the transects where the energy flux was calculated. The height, h_t, and width, W_t, of the topography varied between the simulations dependent on the topography-to-depth ratio, h_t/d and the slope-wave criticality, γ/s.

$\omega = 0.0035\, rad\, s^{-1}$ and the wave period is defined by $T = 2\pi/\omega = 1800\, s$. Forcing of the internal wave is modified by imposing varied velocity amplitude of forcing U_0 at the inlet of the domain. Each of the three cases in Fig. 6.2 show six snapshots of internal wave developing and propagating over the topographic ridge, all normalized by the wave period T. The domain depicted starts at $x = 60\, m$, ends at the computational domain outlet $x = 150\, m$ and is colored by the stratification, depicted using the temperature anomaly.

With $Fr = 0.1$ the six panels in Fig. 6.2a show the propagation of an internal wave forced by $U_0 = 0.003\ m\ s^{-1}$. The dynamics of this simulation are dominated by linear oscillations of the flow field as the internal wave propagates to the ridge. Some minimal magnitude displacement is visible in the flow field on the upstream side of the ridge as well as above the peak in topography. While some dissipation and mixing is occurring most of the energy is either being reflected off the topography or transmitting past the topography.

Fig. 6.2b shows a simulation with $Fr = 0.5$ set by $U_0 = 0.015\ m\ s^{-1}$. Presence of non-linear dynamics are visible in the snapshots of this simulation with dense fluid from the base of the stratified profile propagating up and over the ridge. These flow structures have been both simulated (Venayagamoorthy, 2006; Venayagamoorthy & Fringer, 2007) as well as observed (Cacchione & Wunsch, 1974) and are know as tidal bores, or solibores. These flow structures generate as a result of the internal wave creating a vortex core that advects dense fluid from low in the water column up onto a continental shelf or over the top of topography. In addition to the advection of dense fluid by bores larger magnitude displacements of fluid are visible relative to the case with $Fr = 0.1$. Displacements of fluid, both on the upstream side of the ridge as well as above the topographic peak, increase in magnitude. The drawdown of fluid on the upstream side of the ridge as the internal wave advects toward the ridge, as well as the propagation of the bore to the downstream side of the ridge creates regions of unstable stratification where denser fluid overlies less dense fluid. Visible in the snapshots are the overturning structures that result from unstable stratification and the advection of the bolus.

A velocity amplitude of forcing $U_0 = 0.025\ m\ s^{-1}$ sets a simulation with $Fr = 0.84$, depicted in Fig. 6.2c. It is clear from the series of snapshots that the dynamics become highly non-linear and unstable with the increase in energy. Fluid displacements, the size of the bore transporting mass over the ridge as well as the magnitude of overturns resulting from unstable stratification are all of greater magnitude when compared to the other two cases. In the previous case the bore is ejected off the ridge creating an overturn and mixing. In this case the mass/magnitude of the bore is sufficiently large that it returns down the backside of the ridge. This downslope advection of the bore generates an overturning structure that is in the opposite direction as the ejected bore depicted in Fig. 6.2bv. This final time series clearly show the complex dynamics that result from high wave energy interaction with topography in a stratified flow.

Fig. 6.3 shows the normalized zonal velocity u, normalized vertical velocity w and normalized density profiles for the same three cases discussed for Fig. 6.2. Fig. 6.3a shows profiles for $Fr = 0.1$, Fig. 6.3b from $Fr = 0.5$ and 6.3c for $Fr = 0.84$. The profiles are from simulation iteration $t/T = 6.27$ in case (a) or $t/T = 6.25$ for cases (b) and (c). Each row of normalized plots correspond to section I, section II and section III as depicted in Fig. 6.1, respectively. The zonal velocity, vertical velocity and density profiles at profile section I in the first row for each of the cases shows a similar distribution but normalization of the velocities by U_0 results in varied magnitudes due to the differences in the velocity amplitude of forcing.

For the lowest energy case the profiles at section II show a zonal velocity distribution with increased values near the bed as the the wave approaches the ridge. The vertical velocity magnitude at section II has also increased as would be expected with the zonal flow being redirected vertically over the ridge. The density profile steepens near the bed likely due to the energy of the internal wave pushing the dense fluid near the bottom of the computational domain against the base of the ridge and creating a slight increase in the density near the bottom of the profile. Row 3 of panel (a) shows the distributions at section III, the downstream side of the ridge. Both the zonal and vertical velocity magnitudes have decreased. On the lee side of the ridge the zonal velocity should decrease

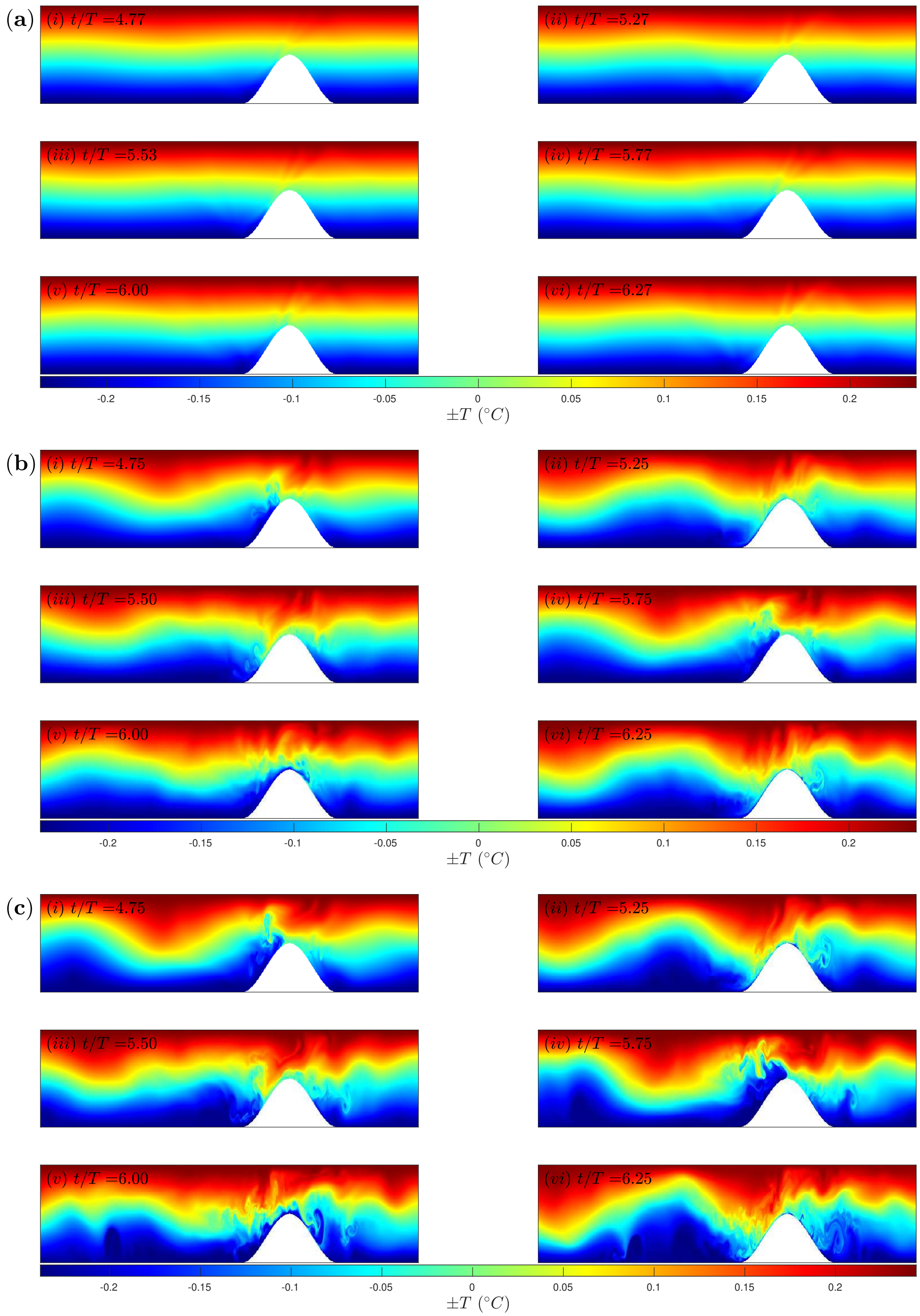

Figure 6.2: Time series snapshots of the fifth internal wave building and passing over the topographic ridge. Color spectrum denotes the temperature gradient of the simulations.$\gamma/s = 1$, $h_t/d = 0.5$ for (a) $Fr = 0.1$, (b) $Fr = 0.5$ and (c) $Fr = 0.84$. As the the Froude number increases the dynamics of the internal waves' interaction with the topographic ridge becomes more complex with more overturning and transport of high density fluid from near the bottom boundary up and over the ridge when $Fr = 0.84$.

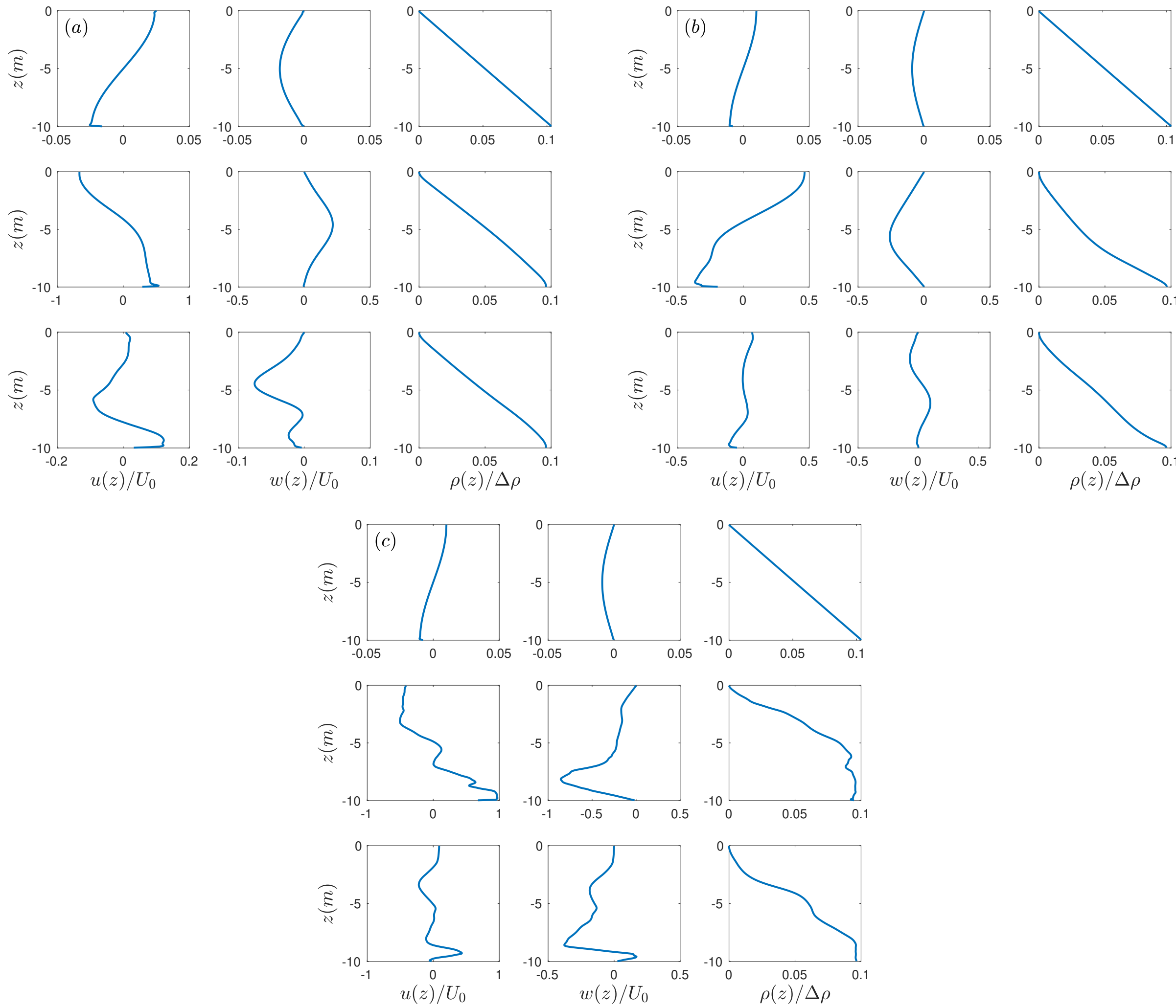

Figure 6.3: Normalized zonal velocity (u), vertical velocity (w) and density (ρ) profiles for $t/T = 6.25$. Grouping (a) is for simulation where $Fr = 0.1$, grouping (b) $Fr = 0.5$ and (c) $Fr = 0.84$. $\gamma/s = 1$ and $h_t/d = 0.5$ are consistent between all three simulations. Within each grouping row 1 denotes profile from transect I, row 2 profile from transect II and row 3 from transect III on the downstream side of the topographic ridge.

as it is sheltered from the incoming internal wave and the vertical velocity switches direction as some of the flow moves down the back side of the ridge.

Figure 6.3b shows the normalized velocity and density profiles at sections I, II and II for simulation with $Fr = 0.5$ at $t/T = 6.25$. At section II the normalized zonal velocity shows a velocity distribution representative of the drawdown on the upstream side of the slope just before the arrival of an internal wave. This distribution is corroborated by the corresponding image from Fig. 6.2b(vi) showing the fluid being drawn downslope during the simulation at this instant, resulting in the negative vertical velocity. The density profile also show the impact of the drawdown of lighter fluid from higher in the stratified fluid column.

In Fig. 6.3c many of the same trends are observable for the simulation defined by $Fr = 0.84$ at $t/T = 6.25$. The increased velocity of this simulation results in a zonal velocity distribution that is already propagating up the ridge at section II. It had not yet arrived at the ridge in the previous case resulting in the drawdown profile discussed above. The density profiles from section II and section III show the result of the increase in energy of this simulation with more varied distributions of density due to turbulence and mixing. Regions of unstable stratification are also observed in the profile at section II.

6.3.2 Energy Flux

The governing equation for the energetics is derived by taking the dot product of Eqs. (6.1) with $\mathbf{u}$ and adding the resulting equation to the product of Eq. (6.3) and gz to obtain

$$\frac{\partial}{\partial t}(\rho_0 q + \rho g z) + \nabla \cdot \mathbf{f} = -\rho_0 \epsilon_k - 2\kappa \frac{\partial}{\partial z}(\rho g), \tag{6.8}$$

where $q = \mathbf{u} \cdot \mathbf{u}/2$ is the kinetic energy per unit mass, $\epsilon_k = \nu \partial u_i/\partial x_j \; \partial u_j/\partial x_i$ is the viscous dissipation rate of kinetic energy and the local energy flux is given by

$$\mathbf{f} = \mathbf{u}(\rho_0 q + p + \rho g z) - \mu \nabla q - \kappa(\rho g z), \tag{6.9}$$

with μ denoting the dynamic viscosity. The change in time-integrated energy flux is given by

$$\Delta E_\tau + (E_\tau)_{III} - (E_\tau)_{II} = -\epsilon + \phi_i, \tag{6.10}$$

where ϵ is the integrated kinetic energy dissipation rate and ϕ_i is the time-integrated energy flux through the upper and lower domain boundary surfaces ($\phi_i = -2\kappa g \int_0^t \int_0^{L_2} (\rho_{top} - \rho_{bottom}) dx d\tau$, see Winters et al. (1995)). Change of total energy (units of $J\ m^{-1}$) within the control volume is

$$\Delta E_\tau = \int_0^{L_2} \int_{-d}^{0} \left[\rho_0 q + g(\rho - \rho_b)z\right] dz dx, \tag{6.11}$$

and the time integrated energy flux (also units of $J\ m^{-1}$) is given by

$$E_\tau = \int_0^t F_E(\tau) d\tau, \tag{6.12}$$

where the depth-integrated energy flux (units of $W\ m^{-1}$) is given by

$$F_E = \int_{-d}^{0} \left[u(\rho_0 q + \rho g z + p) - \mu \frac{\partial q}{\partial x} - \kappa \frac{\partial}{\partial x}(\rho g z) \right] dz. \tag{6.13}$$

Assuming that at $t = 0$ the density field is given by the imposed background density field ρ_b and that the contribution of the diffusive terms to the energy flux is negligible the change in total energy can be computed using the simplified depth-integrated energy flux

$$F_E = \int_{-d}^{0} p' u dz \tag{6.14}$$

where $p' = \rho_0 q + \rho g z + p$. The pressure term, p can be split into two terms denoting its hydrostatic (p_H) and non-hydrostatic (p_{NH}) components gives $p' = \rho_0 q + \rho g z + p_H + p_{NH}$. If the total density is defined by $\rho = \rho_0 + \rho_b + \rho'$ Eq. (6.13) can be simplified to become

$$F_E = \underbrace{g\int_{-d}^{0} u \int_{z}^{0} \rho' dz' dz''}_{(a)} + \underbrace{\rho_0 \int_{-d}^{0} u \int_{z}^{0} \frac{Dw}{Dt} dz' dz''}_{(b)} + \underbrace{\rho_0 \int_{-d}^{0} uq dz'}_{(c)} + \underbrace{\int_{-d}^{0} u\rho' gz dz'}_{(d)} + \underbrace{\int_{-d}^{0} u\rho_b gz dz'}_{(e)} + \underbrace{g\int_{-d}^{0} u \int_{z}^{0} \rho_b dz' dz''}_{(f)} . \quad (6.15)$$

where each term in Eq. (6.15) can be described as follows:

(a) Energy flux due to the rate of work done by the hydrostatic pressure fluctuations.

(b) Energy flux due to the rate of work done by the nonhydrostatic pressure.

(c) Energy flux due to the advection of kinetic energy.

(d) Energy flux from the advection of potential energy due to density fluctuations.

(e) Energy flux from the advection of potential energy due to the mean background density field.

(f) Energy flux from the rate of work done by the hydrostatic pressure due to the mean background density field.

Using each term above the energy flux contributions can be determined from the numerical simulation data. As discussed by Venayagamoorthy & Fringer (2006) over 50% of the energy flux should result from hydrostatic pressure anomaly while approximately 30% of the energy flux should be contributed by the nonhydrostatic pressure term, the two largest contributors to the energy flux budget. Figure 6.4 shows both the depth integrated flux (solid blue lines) as well as the cumulative energy flux (dashed magenta lines) for each of the terms in Eq. 6.15 for simulation where

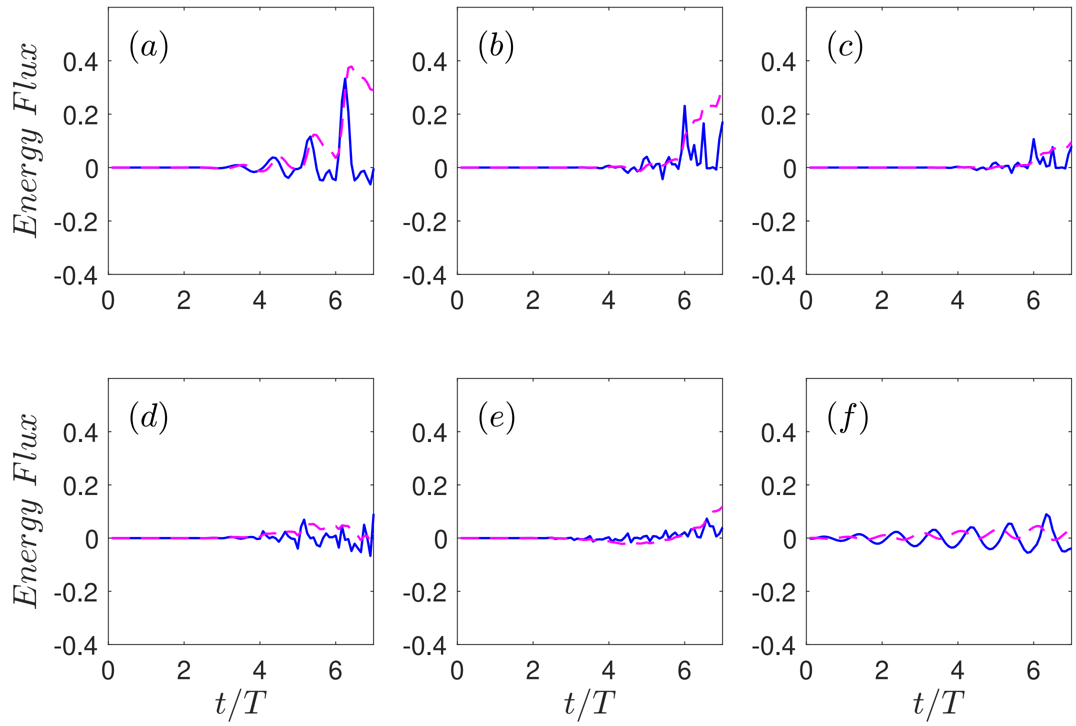

Figure 6.4: Normalized depth integrated (blue solid line) and time integrated energy (magenta dashed line) fluxes as a function of t/T at $x = 105m$ for simulation with where $Fr = 0.5$, $\gamma/s = 1$, and $h_t/d = 0.5$ showing each of the terms in depth integrated energy flux equation.

$Fr = 0.5$, $\gamma/s = 1$ and $h_t/d = 0.5$. For this particular simulation the hydrostatic pressure anomaly term accounts for 56%, the nonhydrostatic pressure term 34% of the energy flux budget. Terms (c), (d), (e) and (f) in Eq. 6.15 contribute 4%, 1%, 5% and 0% respectively. Each energy flux term plotted in Fig. 6.4 is normalized using a base estimate of the energy flux of the incoming internal wave computed using linear wave theory (Kundu et al., 2008)

$$F_L = \frac{\rho_0 \omega U_0^2}{2k} d, \tag{6.16}$$

where ρ_0 is the reference density, ω is the forcing frequency, U_0 is the velocity amplitude of forcing, d is the full flow depth, m is the vertical wave number and k is the horizontal wave number obtained from the dispersion relation for internal waves. This energy flux is the integral of the product of the velocity and pressure perturbations. The evident contribution of the nonhydrostatic pressure work term show the impact of vertical inertia and instantaneous importance of the nonhydrostatic pressure.

If the slope of the internal wave group velocity characteristic, defined by Eq. (6.6), an absence of Coriolis rotation is assumed, it can be shown

$$\frac{F_L}{\rho_0} = \frac{1}{2}U_0^2 c_1 d \frac{1}{(1+s^2)^{1/2}}, \tag{6.17}$$

where c_1 is the mode-1 baroclinic wave speed for a linear hydrostatic ($\omega << N$) internal wave, and can be derived from Eq. (6.7) to be Nd/π. In non-dimensional form Eq. (6.17) becomes

$$\frac{F_L}{F_0} = \frac{Fr_h^2}{(1+s^2)^{1/2}}, \tag{6.18}$$

where $F_0 = \frac{1}{2}\rho_0 c_1^3 d$ is constant for all simulations and $Fr_h = U_0/c_1$ is the Froude number derived using the hydrostatic linear wave speed c_1. This equation points to the fact that incident linear flux grows quadratically with the Froude number for a given characteristic wave group velocity, s. Conversely, for a given Froude number as the characteristic wave slope s increases the energy flux should decrease.

In Eq. (6.10) the contribution from ϕ_i is commonly neglected (Fringer & Street, 2003) leading to an energy budget approximated by

$$E_I = E_R + E_T + E_D, \tag{6.19}$$

where E_I is the incident energy, E_R is the energy reflected back toward the inlet of the computational domain from the topography, E_T is the energy transmitted past the topography and E_D is the energy dissipated in the control volume bounding the topography. Figure 6.5 shows a schematic depiction of the components of the energy flux budget with the control volume centered over the

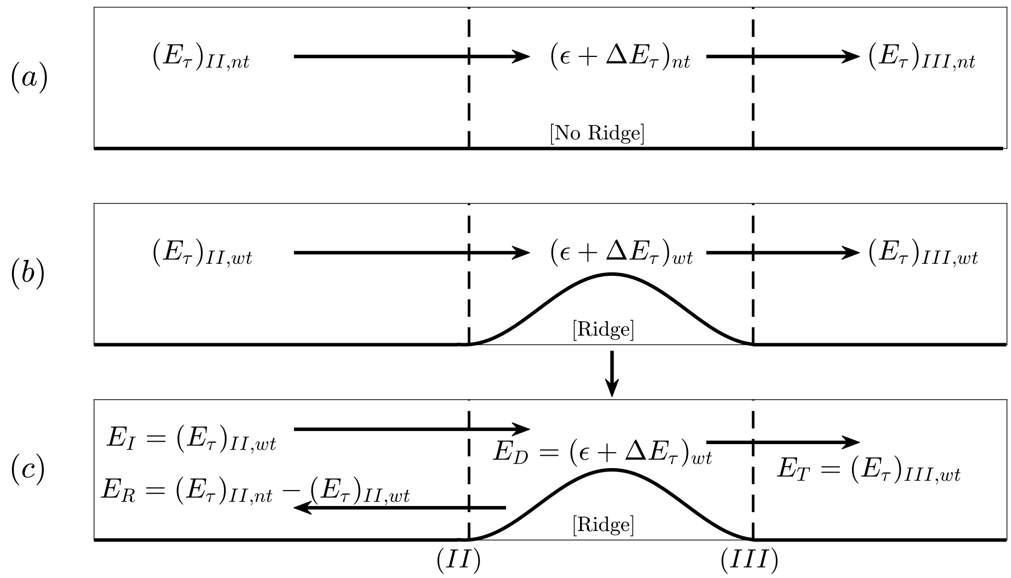

Figure 6.5: Depiction of the energy budget for the control volume centered over the topographic ridge between vertical transects II and III. Panel (a) shows the base case where no topography is present ($\gamma/s = 0$): panel (b) shows the typical topographic ridge case ($\gamma/s > 0$). Schematic (c) shows how the fluxes determined from panel (a) and (b) to close the energy budget and determine the reflected and dissipated energy. Subscript 'nt' denotes the no topography case and 'wt' denotes the case with a topographic ridge.

topography between the dashed lines denoting sections II and III. The reflected energy flux is determined by taking the difference in the incident energy flux at section II of the simulation with no topography present $(E_\tau)_{nt,II}$ and the incident energy flux at section II in the simulation with the topographic ridge being evaluated $(E_\tau)_{wt,II}$. Dissipation of energy is determined by the difference between the cumulative energy flux incident at section II and the cumulative energy flux at section III.

Analysis of how energy is distributed differently between these three components given simulations across the wide range of parameters increases understanding of the dynamics. Figure 6.6 shows the cumulative transmitted, reflected and dissipated energy flux for each simulation as a function of γ/s. All the fluxes are normalized by the cumulative incident energy flux E_I. When the ridge height is only one quarter of the the total flow depth, $h_t/d = 0.25$, the majority of the incident wave energy is transmitted through the domain. When the slope is supercritical the amount of energy transmitted is reduced. The amount of energy reflected and dissipated is very small for

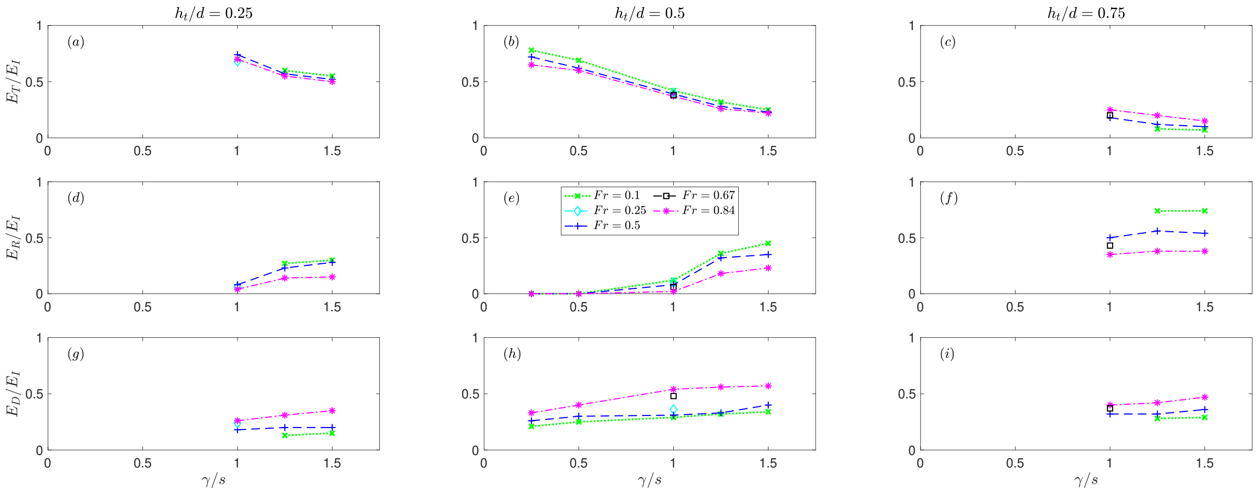

Figure 6.6: Normalized cumulative energy fluxes for all simulations runs as a function of the topographic steepness parameter. Rows denote the normalized transmitted energy flux, normalized reflected energy flux and normalized dissipated energy flux, respectively. Columns group the results by the topography height-total depth ratio, h_t/d.

the critical slope cases but increases slightly when the slope becomes supercritical offsetting the reduction in transmitted kinetic energy.

The second column of Fig. 6.6 shows the results with $h_t/d = 0.5$. Subcritical slope simulations allow for the majority of the energy to transmit up and over the topography but some energy is dissipated by turbulence in the flows with higher Froude numbers. Amounts of reflected energy is very small as would be expected as the internal wave beams forward reflect when the slope is subcritical. For critical slopes approximately half of the energy is transmitted. Amount of reflected energy remains the least significant of the three energy modes analyzed in the cases with critical slopes. Dissipation magnitude varies as a function of Froude number with dissipation accounting for approximately 50% percent of the energy difference at high Froude numbers but less than 25% for the lowest Froude number simulation, $Fr = 0.1$.

As the height of the ridge increases the amount of transmitted energy also decreases as shown in Fig. 6.6c. Approximately 25% of the energy is transmitted for a ridge defined by a critical slope and the majority of the energy is reflected. For the least energetic simulations defined by $Fr = 0.1$ the amount of energy transmitted through the domain is very low with over 75% of the energy being reflected off the topography and the majority of the difference being dissipated. Amounts

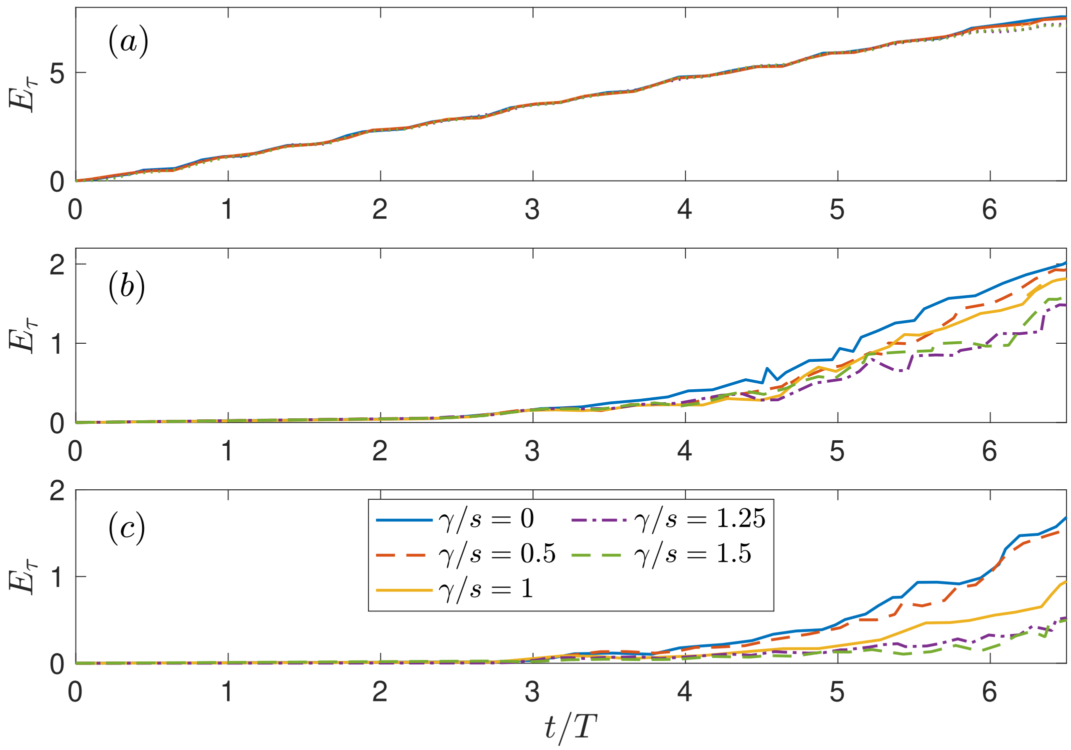

Figure 6.7: Normalized cumulative time integrated energy fluxes E_τ plotted as function of t/T at transects (a) I, (b) II and (c) III for $Fr = 0.5$, $h_t/d = 0.5$. The different lines represent a different degree of slope ratio criticality for the same Froude and depth ratio conditions. Solid blue lines: $\gamma/s = 0$ (no slope); dashed orange lines: $\gamma/s = 0.5$ (subcritical); yellow solid lines: $\gamma/s = 1$ (critical); dash-dot purple lines: $\gamma/s = 1.25$ (low supercritical); dashed green lines: $\gamma/s = 1.5$ (high supercritical); $T = 1800\ s$.

of reflected energy vary significantly with Fr decreasing as the Froude number increases. Flows defined by a larger Froude number lead to more non-linear dynamics and more of the energy being captured by dissipation and mixing. The plots in Fig. 6.6 show how the partition of energy flux is strongly dependent on all three non-dimensional parameters Fr, h_t/d and γ/s.

Figure 6.7 shows the cumulative time integrated energy flux plotted as a function of t/T for simulations with $Fr = 0.5$ and $h_t/d = 0.5$, normalized by F_L/ω. Each line in the figure represents a different slope γ/s condition as denoted in the legend. Fig. 6.7a shows the cumulative flux at section I, Fig. 6.7b at section II and Fig. 6.7c at section III. Observable from the time series is the delay in visible energy flux at section II and section III. The initial delay before any energy flux is noticed at section II and III is a function of the transit time of the internal wave energy from the domain inlet. Lower magnitude cumulative time averaged energy flux at section II and section III results from the dissipation of energy within the control volume as well as energy being back reflected from the ridge. The trends are similar to the trends observed in Fig. 6.6 where more energy is reflected for simulations with supercritical slopes, visible in the lower magnitude cumulative energy flux registered at section III.

6.4 Summary/Conclusion

This analysis presents the results of two-dimensional numerical simulations of internal waves encountering a topographic ridge. The parametric study analyzed covered variation in the relative slope ratio γ/s, the height of the topography to the total flow depth h_t/d, and magnitude of forcing by the internal wave by variation in the velocity amplitude of forcing U_0, creating a variation in the Froude number of the the simulation. The Froude number space explored covers a range of possible flow dynamics from conditions dominated by linear oscillations at low values to complex non-linear dynamics at the high values. Differences in the flow dynamics of the simulations are observable in plots of the domain stratification.

The majority of the internal wave energy available is transmitted for ridge topography with a subcritical slopes. Upon encountering the ridge, the internal wave beams are forward reflected for $\gamma/s < 1$. Differences in the amount of the energy transmitted is solely a function of the internal wave amplitude. More energy is lost to dissipation in simulations with large amplitude internal waves ($Fr = 0.67 - 0.84$) and the resulting dynamics then is lost in simulations with smaller amplitude internal waves ($Fr = 0.1 - 0.25$). Conversely, supercritical slope values where $\gamma/s > 1$, the majority of the available energy is back reflected rather than transmitted. In this case the internal wave beams are back reflected rather than forward reflected as in the subcritical case. Magnitude of dissipation has a similar dependence on the amplitude of the internal wave forcing. For low Froude numbers most of the wave energy is reflected though some is lost to dissipation. At high Froude numbers more of the energy is lost to turbulent kinetic energy dissipation during the wave-topography interaction process as the wave energy is back reflected. For both subcritical and supercritical cases more energy is transmitted when the ridge height is only 25% of the flow depth then when the ridge height is that of half or 75% of the flow depth.

For critical slope cases with $\gamma/s = 1$ the rates of energy transmission, reflection and dissipation are even more strongly correlated with the internal wave amplitude. The formation and propagation of bolus structures as result of internal wave interaction with the ridge helps maintain some energy transmission. Inherent flow instability at high Froude numbers leads to increased energy loss due to dissipation as the wave breaks onto the ridge. This loss of energy in the interaction process creates conditions where large masses of dense fluid is caught in the structure of the breaking wave and the kinetic energy advects this mass of fluid onto the ridge. In some cases the available energy is sufficient to move a large mass of fluid over the top of the ridge and back down the downstream side.

These results describe the distribution of energy fluxes as a result of interaction with a simulated topographic ridge under a range of flow simulation conditions. From the results the dynamics of the process show that there is significant mixing processes that occur near this type of topographic feature. These results reinforce that the structures simulated in laboratory scale DNS are retained/verified in this larger scale simulations. Locations with topographic ridges in the Earth's oceans have been identified as hot spots for dissipation and mixing. The partition of energy as a result of the ridge and analysis of the trends in energy flux are well described by these simulations completed in two-dimensions. Completion of this type of parametric study allows for future simulations in three-dimensions, that need significantly greater computational resources, to focus on cases that will be the most informative for the simulation of overturning structures and the resulting dissipation and mixing. Simulation in three-dimensions will allow investigation into different types of topographic structures, such as seamounts or discontinuous ridges, allowing for flow separation and more complex flow dynamics to be studied.

The final significant contribution of this analysis is the analysis at an intermediate scale. MITgcm and other CFD codes have been used to study internal wave interactions with continental slopes and mid-oceanic ridges. The majority of simulations completed using MITgcm have been completed for field scale topography. Computations domains can range from 1000 km to 10,000 km resulting in computational grid spacing of 100s or 1000s of meters. Useful information can be learned from field scale simulations as the topographic features and domain are realistic to the conditions being studied, but flow features smaller than the grid size can not be captured. This analysis uses MITgcm as a tool validated and trusted by field scientists for simulations that are much smaller in scale. DNS and LES simulations completed at the laboratory scales have a grid size that is sufficiently small to resolve turbulent scales in some cases but do not simulate flow realistic scales. In the simulations presented here the resolution is not fine enough to resolve the turbulent scales but by careful choice of the parameters, grid resolution and increases in computation power we are able to show results that corroborate findings of studies using DNS without resolving the finest of the flow scales. Flow structures such as overturns and bores are visible in visualizations of the simulation similar to those measured in the field or observed in laboratory scale DNS. As the availability and computational power of available resources increase theoretically a field scale simulations could be completed that resolves the turbulent scales. Simulations at the intermediate scale, as presented here, are a necessary step to "bridge" modeling scales until fully resolved field-scale simulations are realizable.

Chapter 7

Flow Structures From Simulations Of Internal Wave Interactions with Topography[6]

7.1 Introduction

Interaction of internal waves with bottom topographic features in the Earth's oceans is an area of study that has seen continual research over the past 20 years. Topographic features such as ridges, seamounts and continental shelves are known to be locations where internal waves break. The breaking of internal waves is thought to be one of the major sources of turbulence in the oceanic setting (Munk & Wunsch, 1998). Turbulence leads to the transport and mixing of a fluid, a critical process in the stratified ocean for the movement of nutrients, sediments and maintaining the gradients that drive global oceanic circulation currents (Aguilar & Sutherland, 2006). There are a variety of mechanisms that can generate turbulence as an internal wave interacts with topography such as internal wave scattering, wave-wave interaction, lee-wave generation and internal wave reflection (Kunze & Smith, 2004). Critical internal wave reflection and wave beam scattering have been shown to be efficient and prevalent mechanisms generating transfer of wave energy to turbulent dissipation (Nash et al., 2004; Kunze & Smith, 2004; Alford et al., 2013).

Internal waves in a linearly stratified fluid (i.e. constant buoyancy frequency, N) can be described by a pair of superimposed beams. If a wave is traveling in a domain with a finite depth the the beams are initially phase locked with one beam that is upwardly propagating and the other that is downwardly propagating. Each beam is characterized by a wave frequency ω and horizontal and vertical wave numbers k and m (Thorpe, 1999). When the the internal wave encounters bottom topography the beams decouple and are reflected based upon the criticality of the slope (Thorpe

[6]The research presented in this chapter is under preparation to be submitted to the *Journal of Physical Oceanography* under the title "Flow Structures from Simulations of Internal Wave Interactions with Topography" by M. R. Klema and S. K. Venayagamoorthy. This chapter is written to reflect and acknowledge the contribution of the other author.

& Haines, 1987). Acoustic and optical waves obey Snell's law and the angle of incidence and reflection is preserved with respect to the normal vector of the encountered surface. Upon reflection internal waves maintain their angle with respect to gravity not normal to the surface of reflection (Phillips, 1977). The angle of the internal wave characteristic from the horizontal is denoted by α and the slope of the internal wave beam is given by

$$s = tan\alpha = \frac{k}{m} = \left(\frac{\omega^2 - f^2}{N^2 - \omega^2}\right)^{1/2}, \tag{7.1}$$

where f denoted Coriolis rotation. Incident wave beams preserve their frequency ω when reflected off of topography. Both the slope of the internal wave beam and the slope of the bottom topography, denoted by γ, must be considered in analysis of waves interacting with bottom topography in stratified fluids. The most common method of classification is to account for both slopes by the ratio of the topographic slope to the wave slope, or γ/s (Phillips, 1977). Subcritical slopes ($\gamma/s < 1$) are cases where the topographic slope is considered flat compared to the wave characteristic slope and the internal wave beams are forward-reflected. When the topographic slope is greater than the wave characteristic slope $\gamma/s > 1$ and are classified as supercritical. Internal wave beams are back-reflected when encountering supercritical slopes. The critical slope case is defined by $\gamma/s = 1$. In this case the angle of wave propagation matches the angle of the slope resulting in a concentration of the internal wave energy upon interaction with the slope leading to increases in mixing. Incident internal waves enter the domain and propagate toward the bottom topography of a given simulation. As a result of this interaction some of the incident wave energy will be reflected, some will be dissipated and some will transmit past the bottom topography. Figure 7.1 shows a simple schematic of the possible components of wave energy as a result of internal wave - topography interaction.

In addition to field measurement in the ocean (e.g. Ray & Mitchum, 1996; Carter et al., 2005; Klymak et al., 2006; Pétrélis et al., 2006; Gill, 2016), laboratory experiments have been conducted to study internal wave interaction with sloping topography (e.g. Cacchione & Wunsch, 1974; Ivey

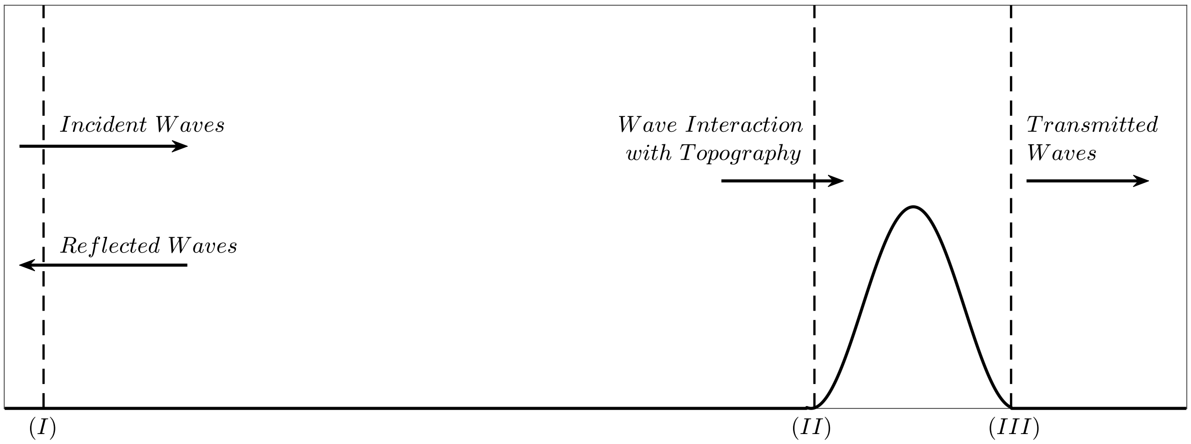

Figure 7.1: Schematic of the computational domain setup used in the simulations presented including a simple depiction of the possible components resulting from the interaction of an internal wave with bottom topography (modified from Venayagamoorthy & Fringer, 2007).

et al., 2000; Dauxois et al., 2004; King, 2010). These experiments corroborate the principles of internal wave reflection in a stratified fluid. Laboratory experiments are limited by their scale and both laboratory experiments and field measurements are limited by the difficulty of making spatially and temporally resolved measurements. Numerical simulations using computational fluid dynamics (CFD) codes have become an important tool for study of stratified flows in the geophysical setting. Direct numerical simulations (DNS) have been used to study stratified flow processes at the laboratory scale, $O(10\ m)$, and are able to resolve turbulence and directly calculate turbulent quantities (e.g. Mater & Venayagamoorthy, 2014b; Maffioli & Davidson, 2016; Garanaik, 2018; Pouquet et al., 2018). Slinn & Riley (1998); Venayagamoorthy (2006); Venayagamoorthy & Fringer (2007) used large eddy simulations (LES) to model internal wave interaction with a continental slope and shelf, showing the complexity of the interaction processes, quantifying estimates of the energy flux and dissipation of the processes as well as corroborating the formation of upslope-surging boluses that transport dense fluid onto the shelf. Jalali & Sarkar (2017) also used LES to model stratified flow around actual topographic features found in the Luzon Strait, South China Sea. Reynolds-averaged Navier-Stokes simulations (RANS) use turbulence closure models and have been used in parametric CFD studies of bulk flow behavior in stratified fluids at the field scale (e.g. Legg & Adcroft, 2003; Legg, 2004a,b; Klymak et al., 2012; Legg, 2014). These simulations aim to investigate flow structure resulting from internal wave-topography interaction at an intermediate simulation scale (greater than the laboratory scale $\sim 10\ m$, but less than a full field scale $\sim 1000\ m$). Investigations into observed changes in flow structure as simulations scale up to larger scales and more simplifying assumptions and parameterizations are included is an open line of inquiry. These simulations provide a first step in this analysis by not resolving the smallest turbulent flow scales and comparing the resulting flow structures to DNS that resolve the turbulent scales.

In this paper we present the results from nonhydrostatic simulations of the interaction of first-mode internal waves with a topographic ridge. Modifications to both the amplitude of the internal wave and the topographic features are explored according to a set of controlling parameters defining this study. The focus of this study is to present an analysis of the changes in flow behavior and features as a result of modifications to the controls. Layout of the paper is as as follows: In Section 7.2 the governing equations, problem setup and modeling tool are introduced; In Section 7.3 the results and analysis of the numerical simulations are presented.

7.2 Formulation and Numerics

The Navier-Stokes equations with the Boussinesq approximation are given by

$$\nabla \cdot \mathbf{u} = 0, \tag{7.2}$$

$$\frac{\partial \mathbf{u}}{\partial t} + \mathbf{u} \cdot \nabla \mathbf{u} = -\frac{1}{\rho_0}\nabla p + \nu \nabla^2 \mathbf{u} - \frac{g}{\rho_0}\rho \mathbf{k} \tag{7.3}$$

$$\frac{\partial \rho}{\partial t} + \nabla \cdot (\rho \mathbf{u}) = \kappa \nabla^2 \rho, \tag{7.4}$$

where ρ is the density, p is the pressure, $\mathbf{u}$ is the velocity vector, ν is the kinematic viscosity (constant) and κ is the molecular diffusivity of the scalar (also constant). Forty two-dimensional CFD

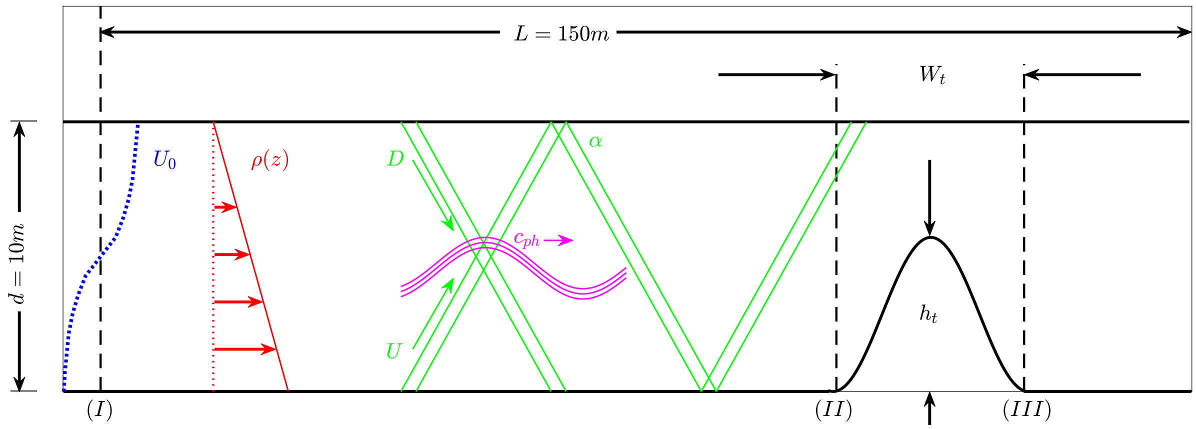

Figure 7.2: Schematic of the computational domain setup used in the simulations presents. Decomposition the internal wave beams is shown as a pair of upward (U) and downward (D) propagation beams (modified from Venayagamoorthy & Fringer, 2007).

simulations and 3 three-dimensional CFD simulations were completed using the Massachusetts Institute of Technology General Circulation Model (MITgcm) to compute Eqs. (7.2)-(7.4) for the domain depicted in Fig. 7.2. This research grade CFD code uses a finite volume formulation for discretizing the computational domain and solving the equations. The total length of the domain is $x = 150\ m$ and the flow depth is $z = 10\ m$. Resolution of the 2D simulations is $\Delta x = 0.05\ m$ and $\Delta z = 0.05\ m$ in the horizontal and vertical directions respectively, a total of $nx \times nz = 2800 \times 200$ or $560,000$ grid points. The three-dimensional simulations have a lateral width of $y = 8\ m$. Resolution of the 3D simulations is $\Delta x = 0.12\ m$, $\Delta y = 0.2\ m$ and $\Delta z = 0.1\ m$ in the horizontal, lateral and vertical directions respectively with a total of $nx \times ny \times nz = 1288 \times 40 \times 100$ or $5,152,000$ grid points.

Initial stratification is set over the entire domain using a linear background distribution $\rho_b(z)$ defined by

$$\frac{\rho(z,t=0)}{\rho_0} - 1 = \frac{\rho_b(z)}{\rho_0} = -\frac{\Delta\rho}{\rho_0}\left(\frac{z}{d}\right). \tag{7.5}$$

At the left inlet boundary the internal wave is forced by prescribing a velocity amplitude of forcing U_0 defined by

$$u(0,z,t) = U_0 cos(mz) sin(\omega t), \tag{7.6}$$

where $\omega = 0.035\ rad\ s^{-1}$ for all simulations. Free-slip boundary conditions are prescribed on the lateral boundaries and a no-slip condition is set at the bottom boundary. While the simulation resolution is not fine enough to resolve the bottom boundary layer setting this condition allows for friction to play a role in evolution of the flow. At the right hand outlet boundary an Orlanski radiative condition is applied allowing for the internal wave energy to leave the computation domain (Orlanski, 1976). At the top boundary a linearized free surface condition is applied allowing finite displacement of the top surface. This oscillation results in a nonzero contribution to the pressure, however, these boundary displacements η are very small relative to the flow depth so the top boundary conditions are applied at $z = 0$ similarly to the classical textbook solution for linear surface waves (Legg, 2014). The single topographic ridge is defined by a sine function providing a slope that is close to the same maximum value over much the change in elevation as discussed by Legg (2014). Wave reflected off of the topography will eventually contaminate the boundary forcing at the left inlet so all simulations are terminated before any contaminated waves reach the slope from the inlet. The topographic ridge is offset to allow for five internal wave periods to pass over the topography before the analyzed waves become influenced by the reflected energy dynamics.

Grid resolution of the simulations is not sufficiently fine to resolve the turbulence down to the dissipation scales. No sub-grid-scale mixing scheme is applied in these simulations, a constant eddy viscosity and turbulent eddy diffusivity are prescribed $\nu = \kappa = 10^{-5}\ m\ s^{-1}$, resulting in a Prandtl number $Pr = \frac{\nu}{\kappa} = 1$. This magnitude for the viscosity and diffusivity will result in the below a certain energy/size threshold being dissipated but is sufficiently small to allow for the majority of the flow structures larger than the grid scale to generate and evolve over the course of the simulation.

Based on an advective length scale $L_c = U_0/\omega = 0.42\ m$ and a characteristic overturning velocity $U_0 = 1.5\ cm\ s^{-1}$ a rough estimate of the turbulent Reynolds number for the median simulation is $Re_T = 620$. Beside the slope ratio γ/s, other important non-dimensional parameters in a finite depth domain include the non-dimensional measure of the incoming internal wave amplitude, or steepness, defined here as a Froude number, $Fr = U_0/c_{ph}$. As denoted above U_0 is the maximum velocity amplitude and c_{ph} is the linear first-mode internal wave phase celerity in a linearly stratified fluid defined by Kundu et al. (2008) as

$$c_{ph} = \frac{\omega}{k} = \frac{d}{\pi}\left(N^2 - \omega^2\right)^{1/2}, \tag{7.7}$$

where N is the buoyancy frequency, k is the horizontal wave number, d is the off ridge depth. The third non-dimensional parameter is the ratio of the topographic height h_t to the off topography domain depth d, h_t/d. Variation of this parameter changes the area obstructed by the ridge. A measure of the wave excursion to the topographic length scale is given by the excursion number $Ex = U_0T/\pi L_s$. This parameter is also sometimes used as measure of barotropic tide generation. Here $T = 2\pi/\omega$ defines the internal wave period and $L_s = \left[h_t^2 + (W/2)^2\right]^{1/2}$ is the length of the topographic slope where W_t defines the width of the ridge. By holding N and ω constant, s also remains constant. Simulation variations in this parametric space were completed by iterating γ/s between 0 and 1.5, h_t/d between 0.25 and 0.75 and Fr between 0.1 and 0.84 by modification to the velocity amplitude U_0. Values of the excursion parameter were calculated for each simulation for purposes of the analysis but this non-dimensional parameter was not explicitly varied as part of the study but varied as a function of the changes to the other parameters. These non-dimensional parameters comprise the set recognized for internal wave - topography interaction (Legg & Adcroft, 2003; Kunze & Smith, 2004; Venayagamoorthy & Fringer, 2007; Legg, 2014) and the full list of simulation details are presented in Table 7.1. Ranges of parameters chosen in this space give conditions that result in wave breaking and other non-linear dynamics over the course of the evolution of the majority of the simulations.

Table 7.1: Details of the 43 simulations, including the parameter space covered. Simulations 1-40 are completed in two dimensions and runs 41-43 are completed in three-dimensions.

Runs	γ/s	$Fr = U_0/c_{ph}$	$U_0T/(\pi L_s)$	ht/d	$Comments$
1-5	0	0.1-0.84	-	-	No-slope cases
6-8	0.25	0.1-0.84	0.03-0.27	0.5	Subcritical cases
9-11	0.5	0.1-0.84	0.06-0.52	0.5	Subcritical cases
12-16	1	0.1-0.84	0.12-1.03	0.5	Critical cases
17-19	1	0.25-0.84	0.62-2.06	0.25	Critical cases
20-23	1	0.5-0.84	0.24-0.67	0.75	Critical cases
24-26	1.25	0.1-0.84	0.29-2.43	0.25	Supercritical cases
27-29	1.25	0.1-0.84	0.15-1.21	0.5	Supercritical cases
30-32	1.25	0.1-0.84	0.1-0.81	0.75	Supercritical cases
33-35	1.5	0.1-0.84	0.33-2.78	0.25	Supercritical cases
36-38	1.5	0.1-0.84	0.17-1.39	0.5	Supercritical cases
39-40	1.5	0.5-0.84	0.56-1.39	0.75	Supercritical cases
41-43	1	0.5-0.84	0.56-1.39	0.5	3D Critical cases

7.3 Results

In this section the results of the 43 numerical simulations are presented and discussed. Subsection 7.3.1 qualitatively outlines the parametric space and the impact of the individual parameters on the flow features that develop over the course of a simulation. Subsection 7.3.2 presents a quantitative assessment of bolus dynamics, one of the main features observed to develop in the simulations enhancing mixing.

7.3.1 Flow Structures From Interaction And Generation Dynamics

Each of the simulations is run for the time it takes five internal waves to pass over the bottom topography, approximately 6.5 wave periods ($T = 2\pi/\omega = 1800\ s$) since the initial internal wave must travel the domain to the topography. This is a common criteria for setting the simulation duration in stratified flow CFD simulations and is also considered a necessary condition for a simulation to have reached steady state (Venayagamoorthy, 2006; Legg, 2014; Garanaik & Venayagamoorthy, 2019). Length of the domain is influenced by simulation duration. All simulations are stopped before waves that have been contaminated by energy reflected from the topography, impacts the inlet boundary condition, reach the control volume used in the analysis.

As each internal wave reaches the start of the bottom topography, defined by vertical analysis section II in Fig. 7.2, the dynamics of the flow change as a result of the internal wave-ridge interaction. Figure 7.3 shows a series of plots depicting an internal wave arriving and passing over the ridge, time sequenced in order from (a)-(g). This simulation plotted here is defined by $Fr = 0.67$, $h_t/d = 0.5$ and $\gamma/s = 1$. Each of the individual plots in this figure is also labelled with the simulation time t normalized by the internal wave period T. The temperature difference from the median profile temperature is used to visualize the stratification of the flow in the domain.

In Fig. 7.3a ($t/T = 5.33$) the oncoming internal wave can be seen near the left boundary of the figure. Effects of the previous wave are visible in the figure including the entrainment of lighter fluid from the fluid drawdown on the front side of the topography. This effect is created by the oncoming wave. Some localized mixing above and on the backside of the ridge is also present. Steepening of the wave front, with Kelvin-Helmholtz-like structures near the start of the ridge from the drawdown of the lighter fluid are visible in Fig. 7.3b ($t/T = 5.50$). Some overturning structures on the backside of the ridge remain from the previous internal wave. As the flow evolves, in Fig. 7.3c ($t/T = 5.58$) clockwise rotation of the core of dense fluid starts to form a bolus starting the advection of dense fluid from near the bottom of the ridge up the slope of the ridge. In Fig. 7.3d ($t/T = 5.56$) the bolus structure has clearly developed and is nearing the top of the ridge clearly influencing the surrounding flow. Counter-clockwise circulations in the region above the bolus core are notable as the bolus core progresses. The bolus reaches the top of the ridge and it is clear from Fig. 7.3e ($t/T = 5.83$) that a significant amount of the dense bottom fluid has been transported above its equilibrium position in the stratification to the top of the ridge. As the bolus crests the ridge, Fig. 7.3f ($t/T = 5.92$), momentum creates a small ejection of the structure where the core slightly loses contact with the boundary and lighter fluid is positioned between the bolus and the ridge. In addition to kinetic energy once the bolus reaches the crest of the ridge it now has potential energy. Because as a result of unstable stratification profile the bolus core has more mass than the fluid surrounding the core. While the structure visible is still considered a bolus because the mass of fluid is traveling downslope through less dense fluid it can be considered somewhat analogous to a gravity current. The bolus core has decreased in size by the time is has travelled halfway down the backside of the ridge as shown Fig. 7.3g ($t/T = 6.08$). It is still visibly rotating (clockwise) and generating reciprocating counter-clockwise circulations in the fluid above the core. Mixing still visible in the final plot, Fig. 7.3h ($t/T = 6.17$) but the core is surrounded by fluid of similar density as denser bottom fluid has been transport from the front to the backside of the ridge as a result of the flow dynamics.

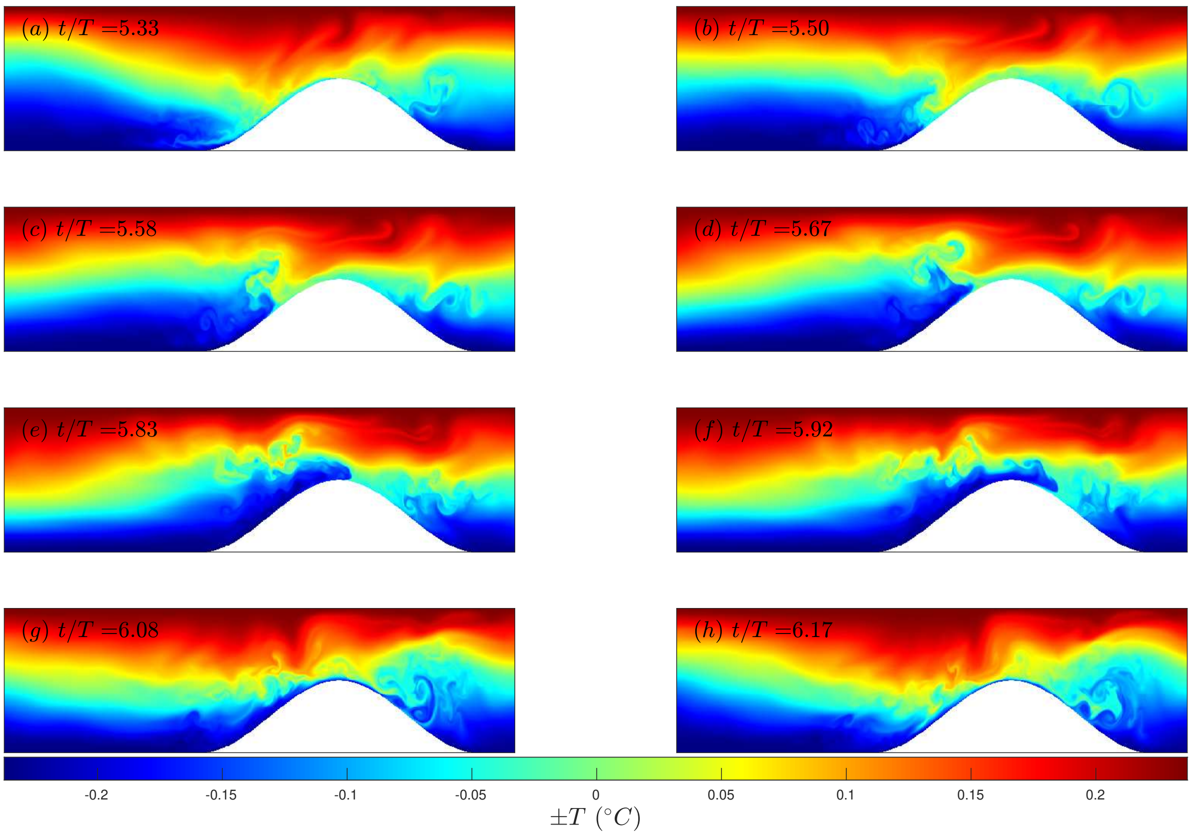

Figure 7.3: Times series capturing the development and travel of an internal bolus for simulation $Fr = 0.67$, $\gamma/s = 1$ and $h_t/d = 0.5$. The effect of the bolus on the surrounding fluid can also be observed as the simulation evolves in time. Flow is colored by the difference in temperature from the mean profile temperature, a measure of stratification used for this visualization.

Influence of Froude number

As discussed in Section 7.2 the Froude number is a measure of the steepness of the oncoming internal wave. In these simulations the Froude number is also used as a measure of the magnitude of forcing. The greater the magnitude of the Froude number the greater the energy of the internal wave forced at the left boundary. Figure 7.4 presents simulation results with $\gamma/s = 1$ and $h_t/d = 0.5$ held constant but three different values for the Froude number. The three subplots in Fig. 7.4, (a)-(c), each have two panels. The first in each row are analogous to those shown in Fig. 7.3 visualizing the computational domain and the stratification of the fluid as a function of temperature. Flow is captured at the non-dimensional time step of $t/T = 6$ and isopycnals (lines of constant density) have been added. Due to the resolution of the simulation quantities such as the kinetic energy dissipation rate ϵ_k and potential energy dissipation rate ϵ_{pe} can not be calculated directly. Plots in the second position of each row in Fig. 7.4 show the time-averaged tendency of the kinetic energy dissipation rate. This quantity is an inexact proxy for the kinetic energy dissipation rate. Values in these plots of the time integrated tendency are not directly useful for quantification of ϵ_k but are useful as a comparison tool for the distribution and relative magnitudes of dissipation between the cases studied in this analysis .

Figure 7.4a shows the results for $Fr = 0.1$. This case is the lowest energy and while the reflected internal wave beams are influencing the isopycnals in the left plot no overturns or significant mixing is occurring. Dissipation resulting from the internal wave beams reflecting off the topographic ridge (as well as adjacent to the boundary) is visible in the right panel of Fig. 7.4a. The pattern resulting from the beam reflection is a common distribution pattern resulting from the reflection of internal waves. When the Froude number is increased to a magnitude of 0.5 there is sufficient forcing to generate a bolus, visible on the backside of the ridge after being ejected from the peak in the left panel of Fig. 7.4b. Also clearly visible in this figure is overturning of the isopycnals and mixing of the stratified fluid. In the right plot of Fig. 7.4b the dissipation tendency due the reflected beams is no longer clearly visible but clearly the amount and magnitude of dissipation relative to the case with $Fr = 0.1$ is significantly greater. Plots in Fig. 7.4c show the case with $Fr = 0.84$. The size of the overturns, magnitude of isopycnal displacement and the amount and distribution of dissipation tendency increase. There is a noticeable increase near the start of the ridge. Entrainment from drawdown as the wave amplitude increases is also more significant.

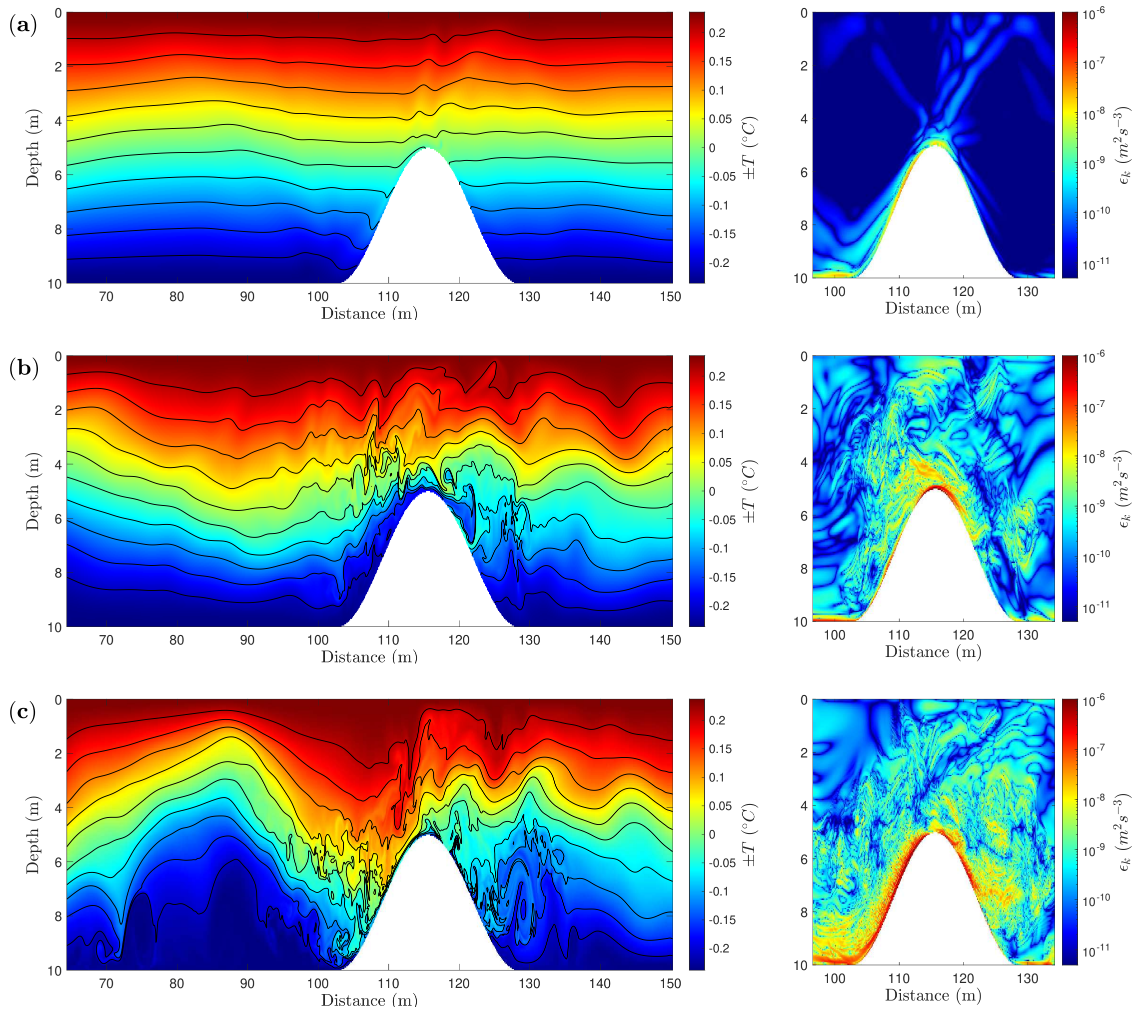

Figure 7.4: Flow structure and time-integrated kinetic energy dissipation rate tendency for three simulations at $t/T = 6$ for varied Froude numbers: (a) $Fr = 0.1$; (b) $Fr = 0.5$; and (c) $Fr = 0.84$. $h_t/d = 0.5$ and $\gamma/s = 1$ for all three simulations depicted. Flow is colored by the difference in temperature from the median profile temperature, a measure of stratification used for this visualization.

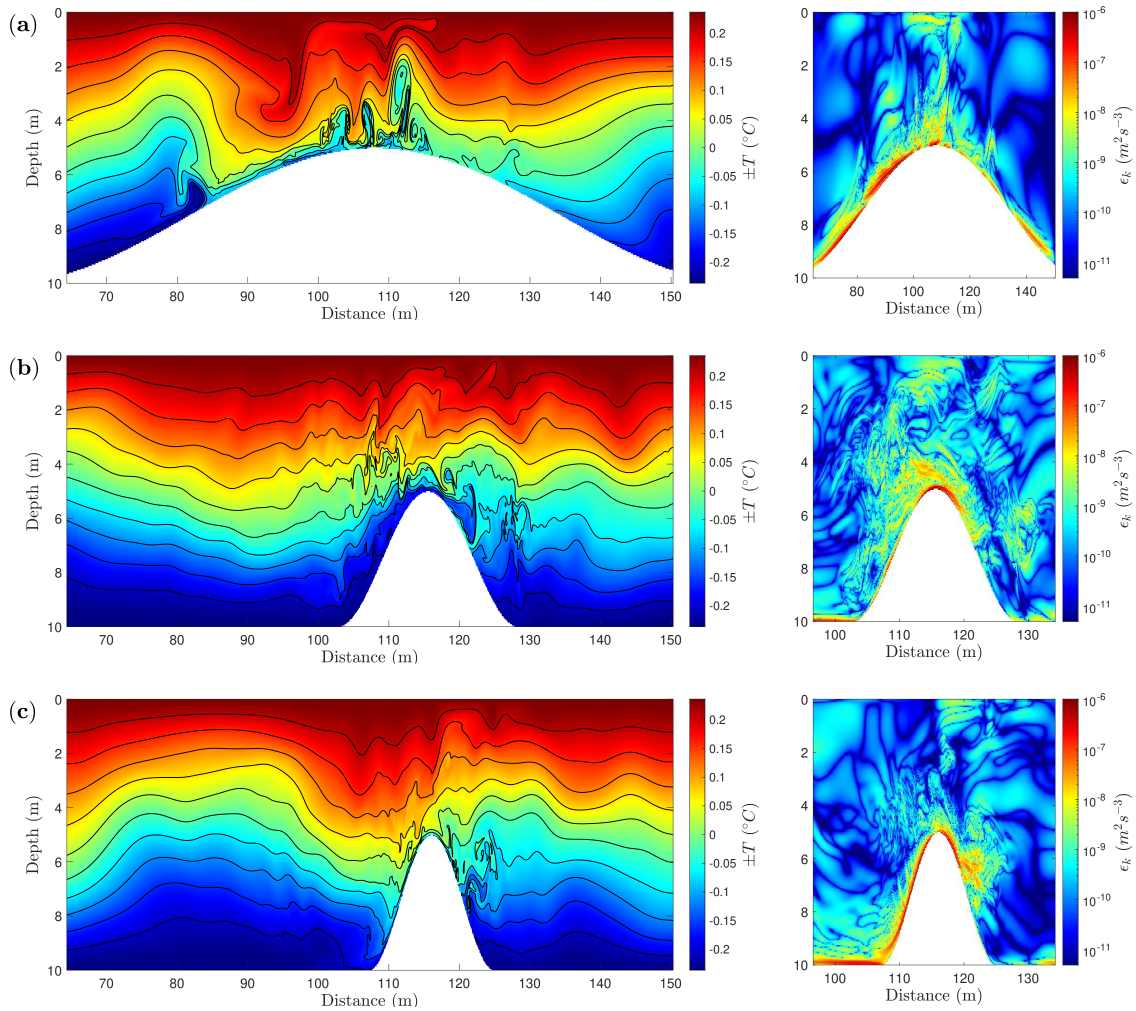

Figure 7.5: Flow structure and time-integrated kinetic energy dissipation rate tendency for three simulations at $t/T = 6$ for varied slopes: (a) $\gamma/s = 0.25$, (b) $\gamma/s = 1$ and (c) $\gamma/s = 1.5$. $h_t/d = 0.5$ and $Fr = 0.5$ for all three simulations depicted. Flow is colored by the difference in temperature from the median profile temperature, a measure of stratification used for this visualization.

From these plots in this figure it is clear that as the Froude number increases so do the non-linear dynamics.

Influence of slope

Figure 7.5 presents results in the same format as Fig. 7.4 but the simulations displayed are defined with constant $Fr = 0.5$ and $\gamma/s = 0.5$. Effects of changes in slope γ/s on the flow are visualized in this figure. In the first row of Fig. 7.5a $\gamma/s = 0.25$, in Fig. 7.5b $\gamma/s = 1$ and in Fig. 7.5c $\gamma/s = 1.5$. Note that the simulation in Fig. 7.5b is the same simulation presented in Fig. 7.4b.

For $Fr = 0.5$ dense fluid is transported over the ridge peak in each case. In condition (a) there is no concentration of the reflected wave energy and the small bolus that is generated continually decreases in size as it traverses the ridge. The advection of this fluid results in reciprocating counter-clockwise overturns, concentrated above the peak in the ridge where the majority of the bolus dissipation occurs. Dissipation tendency is concentrated near the boundary and above the ridge peak from the reciprocating circulations. As discussed previously the case presented in Fig. 7.5b depicts an ejected bolus, local overturns and increased distribution of energy dissipation tendency. For the three cases visualized in this figure this second case generates the largest bolus and greatest distribution of non-linear dynamics. For the supercritical case presented in Fig. 7.5c there is some fluid mass passing over the ridge. Also visible are some overturning structures but there is less impact on the isopycnals. There is reduced in the dynamics generated observable by both the magnitude of isopycnal displacement and smaller region around the ridge where they are significantly influenced. Distribution of dissipation tendency suggest that the mass coming over the ridge is likely fluid transported from the middle of the profile as most of the dissipation tendency is observed above the middle of the profile on the backside of the ridge. Little mixing appears to be occurring near the bottom on the downstream side of the ridge.

Influence of height

Figure 7.6 is used to visualize the influence of ridge height. $Fr = 0.5$ and $\gamma/s = 1$ constant for all three simulations presented. h_t/d is set at 0.25, 0.5 and 0.75 in Fig. 7.6a, Fig. 7.6b and Fig. 7.6c, respectively. Again, note that the simulation visualized in Fig. 7.6b is the same simulation presented in Fig. 7.4b and Fig. 7.5b. With a ridge height that is one-quarter of the flow depth more flow is able to transmit through the domain. While the internal wave-topography interaction still influences the flow dynamics the reduced size of the ridge greatly reduces the region of influence, which is concentrated within 20-meters and predominately downstream of the ridge. The magnitude of mixing is also much more limited for the case where the ridge height is 75% of the flow depth. There is little energy or mass progressing much past the peak in the ridge. Of most significance may be the increase in the non-linear dynamics on the upstream side of the

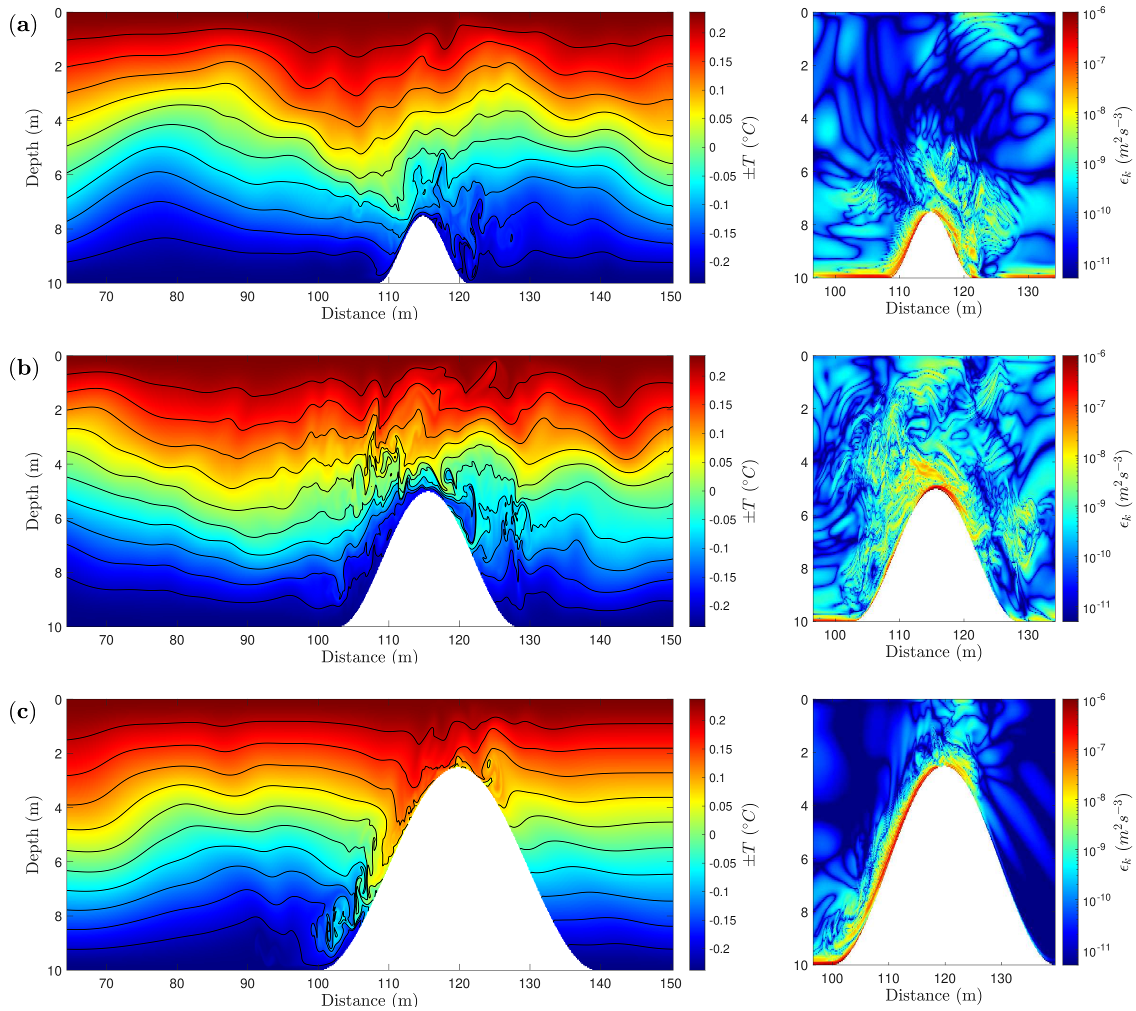

Figure 7.6: Flow structure and time-integrated kinetic energy dissipation rate tendency for three simulations at $t/T = 6$ for varied topographic ridge heights: (a) $h_t/d = 0.25$, (b) $h_t/d = 0.5$ and (c) $h_t/d = 0.75$. $Fr = 0.5$ and $\gamma/s = 1$ for all three simulations depicted. Flow is colored by the difference in temperature from the median profile temperature, a measure of stratification used for this visualization.

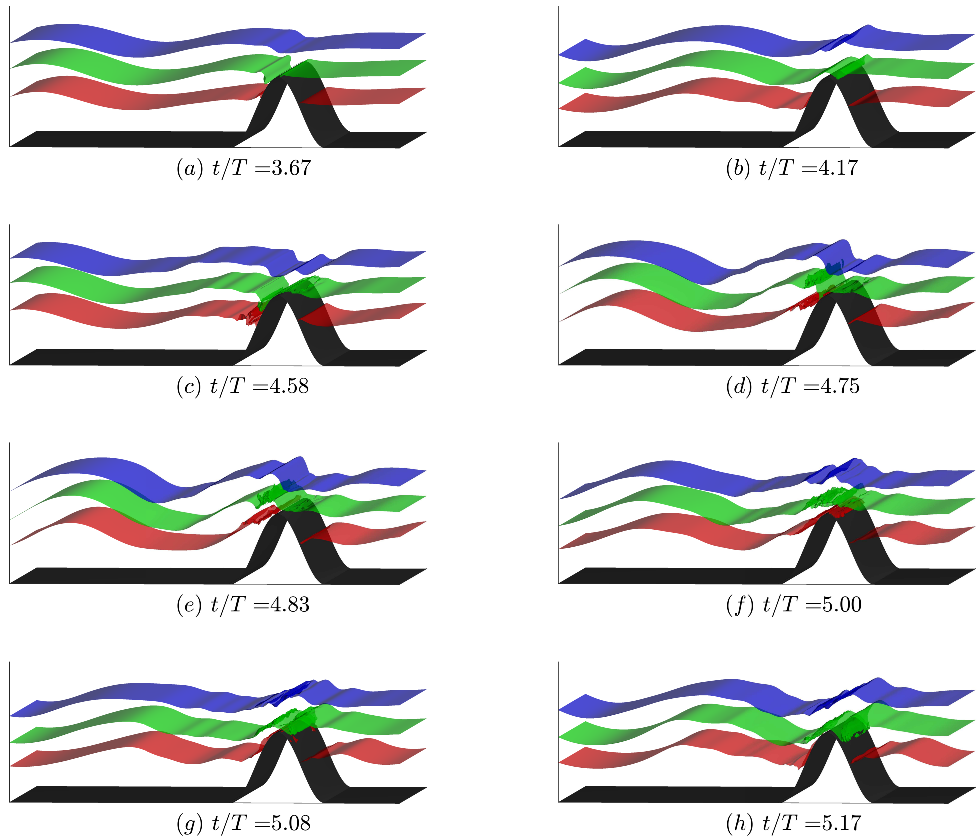

(a) t/T =3.67 (b) t/T =4.17

(c) t/T =4.58 (d) t/T =4.75

(e) t/T =4.83 (f) t/T =5.00

(g) t/T =5.08 (h) t/T =5.17

Figure 7.7: Visualization of density isosurfaces in three-dimensional simulation $Fr = 0.67$, $\gamma/s = 1$ and $h_t/d = 0.5$. Note surging and transfer of dense fluid over the topographic ridge.

ridge as the wave oscillations generate periodic drawdowns and surges that are mostly isolated on the upslope of the ridge. In this case displayed in Fig. 7.6c the dissipation tendency is highest along this upstream side of the ridge. The final figure in this section, Fig. 7.7, show isopycnal, surfaces in three dimensions for simulation where $Fr = 0.67$, $\gamma/s = 1$ and $h_t/d = 0.5$. From the time series of images non-linear dynamics such as overturns and the surging of the red isopycnal over the peak in topography can be observed.

7.3.2 Bolus Analysis

The analysis above gives a broad qualitative analysis of the parametric space and the impact of each of the parameters on the formation of boluses and non-linear dynamics. These simulations can be used for a quantitative analysis of the internal boluses following the analysis presented by Venayagamoorthy & Fringer (2007) in a DNS study of internal wave interaction with a continental slope. Having completed simulations for a range of γ/s values, ridge heights h_t as well as Fr magnitudes allows for a wide ranging analysis focused on bolus dynamics and their evolution and fate in internal wave-ridge interactions.

Using Eq. (7.8) the formation and vertical displacement Δz of an an internal bolus containing the densest fluid can be quantified as

$$\frac{\Delta z}{d} = \frac{z_{max(\rho)_{onslope}} - z_{eq}}{d}, \tag{7.8}$$

where $z_{max(\rho)_{onslope}}$ is the maximum elevation reached by the densest fluid traveling up the topographic ridge during the duration of the simulation. z_{eq} denotes the off-ridge equilibrium elevation of the maximum density contained with the bolus traveling up the slope of the ridge, $max(\rho)_{onslope}$, and is defined by

$$z_{eq} = -\frac{max(\rho)_{onslope} - \rho_0}{\Delta\rho} d, \tag{7.9}$$

where d is the off-ridge depth. Results plotted in Fig. 7.8 show the values calculated by applying Eq. (7.9) for each simulation in $\gamma/s - Fr$ space. Figure 7.8a gives the results for simulations with $h_t/d = 0.25$, Fig. 7.8b for simulations with $h_t/d = 0.5$ and Fig. 7.8c for $h_t/d = 0.75$. Contours in each plot show the trends of the calculated $\Delta z/d$ values, plotted as colored circles. Many of the qualitative observations from the previous section are quantified in this analysis. When the Froude number is small the incoming internal waves are dominated by linear dynamics and there is minimal isopycnal distortion/displacement and no bolus formation. As the magnitude of Fr increases more of the heavy fluid from low in the stratified fluid profile is displaced to a greater magnitude. As was shown in the analysis of Venayagamoorthy & Fringer (2007), it is evident that bolus formation and the resulting vertical displacement of fluid is strongly correlated with the Froude number. For a given value of Fr the vertical displacements are higher for critical slopes, as a result of the concentration of energy from the converging wave beams.

Application of linear wave theory can be used to analyze the wave reflection and to quantify the lower bound for the formation of bores/boluses. The analysis of Legg & Adcroft (2003) uses the criteria of advective velocity exceeding the phase velocity of the reflected internal wave for a bore or density front to develop from the flow. A Fr value of greater than 1 for the reflected wave would be needed using this criteria. As discussed in Section 7.2 the frequencies of incident internal wave are maintained when the wave is reflected. As a result the angles of inclination of the incident and reflected horizontal wave numbers (k_i and k_r, respectively) as measured from vertical/gravity must be equal (Phillips, 1977). Written as a function of the incident horizontal wave number the reflected horizontal wave number can be written as

$$k_r = k_i \frac{sin(\alpha + \theta)}{sin(|\alpha - \theta|)}, \tag{7.10}$$

where α is defined by Eq. (7.1) is the angle of the wave characteristic with respect to horizontal and θ is the topographic slope angle also from the horizontal. This formula implies that the horizontal phase velocity of the reflected wave is less than that of the incident wave (for slopes meeting the condition $0 < |\alpha - \theta| < \pi/2$) and can be defined by

$$(c_{ph})_r = \frac{\omega}{k_i} \frac{sin(\alpha + \theta)}{sin(|\alpha - \theta|)}. \tag{7.11}$$

For cases with topographic slope that are horizontal or vertical (i.e. $\theta = 0$ or $\theta = \pi/2$) it should be noted that the reflection is regular with $k_i = k_r$. The energy density of the reflected wave increases upon reflection resulting in an increase in the velocity amplitude

$$(U_0)_r = (U_0)_i \frac{sin(\alpha + \theta)}{sin(|\alpha - \theta|)}. \tag{7.12}$$

Using Eqs. (7.10)-(7.12) the reflected Froude number is defined as

$$Fr_r = \frac{(U_0)_r}{(c_{ph})_r} = \frac{(U_0)_i}{(c_{ph})_i} \left(\frac{sin(\alpha + \theta)}{sin(|\alpha - \theta|)} \right)^2. \tag{7.13}$$

If a condition $Fr_r > 1$ is needed for bores to develop a relationship can be written to define this region in parametric space in terms of γ directly (Legg & Adcroft, 2003) or in terms of γ/s (Venayagamoorthy & Fringer, 2007). Using γ/s as the second region to define the parametric space results in the following two equations:

$$(\gamma/s)_1 = \frac{Fr_i^{-1/2} - 1}{Fr_i^{-1/2} + 1} \qquad\qquad (\gamma/s)_2 = \frac{Fr_i^{-1/2} + 1}{Fr_i^{-1/2} - 1}. \tag{7.14}$$

The subcritical region is defined by $(\gamma/s)_1 < 1$ and the supercritical region by $(\gamma/s)_2 > 1$. The boundary defined by this theory is plotted as the curved solid black line in Fig. 7.8 and predicts the formation of boluses for conditions above the line. A bolus is not formed for all cases above this line where for marginal cases there may only be some density oscillation on the wave front surging up and down the slopes as the internal waves propagate through the domain. As noted in Venayagamoorthy & Fringer (2007), this theory is derived assuming linear inviscid waves and a finite viscosity will cause an increase in the critical Froude number for which boluses will form for a given γ/s, a observation corroborated by this analysis.

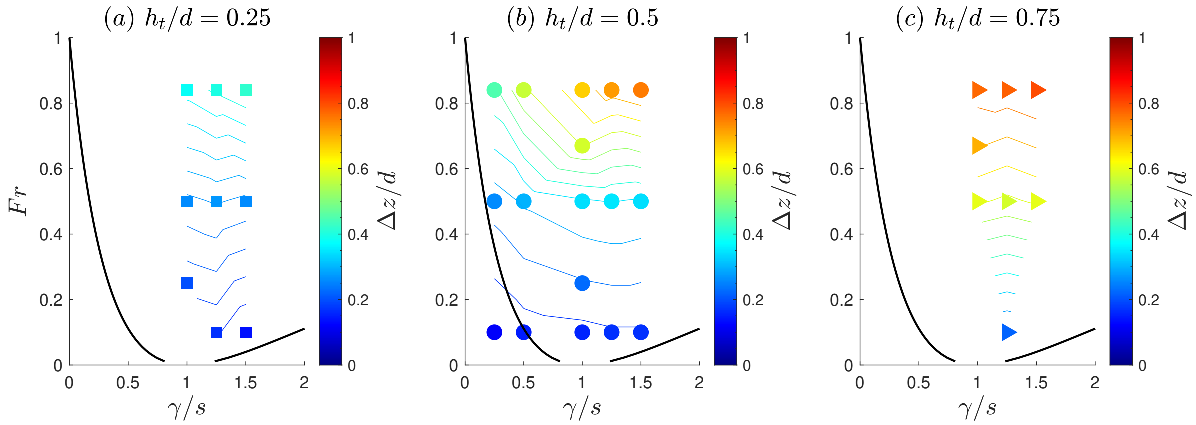

Figure 7.8: Contour plot interpolated from the simulation data points (filled circles) depicting the normalized vertical displacement $\Delta z/d$ of the lowest density fluid onto the topographic ridge in γ/s-Fr space calculated using Eq. (7.8). The black lines denote the lower boundary for the formation of propagating boluses by the linear theory given by Eqs. (7.14).

Under conditions where boluses form, mass is transported up the ridge slope against the stratification. Quantification of the quantity of mass transported provides a measure of the bolus strength and is defined by Venayagamoorthy & Fringer (2007) as

$$m = max\left(\int_{\not{V}} (\rho - \rho_b)\, d\not{V} / \int_{\not{V}} \rho_b d\not{V}\right), \tag{7.15}$$

where ρ is the density of the fluid within a control volume during the passage of the bolus and ρ_b is the background density of the ambient fluid within the control volume. In this analysis the control volume is defined by a $0.25d \times 0.25d$ ($\times 8\ m$ in the 3D case) with the base of the control volume starting and centered over the peak of the topographic ridge. In this analysis the mass of the bolus generated by the fifth internal is used to determine the bolus strength and correlates with the instant the bolus is also centered on the ridge. The control volume is held constant in the analysis of all the simulations. Performing the calculation in this manner preserves comparability between the simulations with variation in the topographic parameters such as height and slope/width. While this definition of the control volume has some impact on the analysis we believe it may be the best way to compare the bolus strength while varying both h_t/d and γ/s in addition to Fr. Figure 7.9 presents the results from the application of Eq. (7.15).

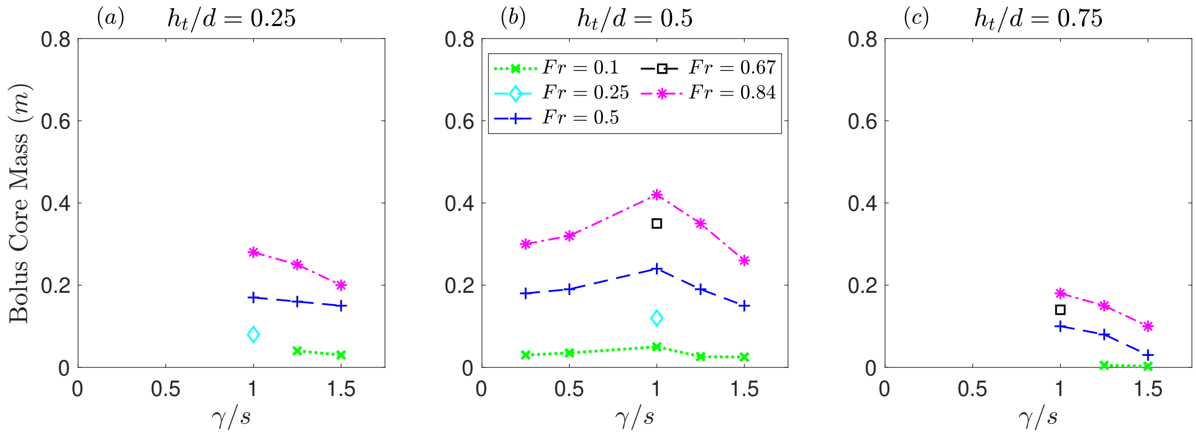

Figure 7.9: Non-dimensional mass of the bolus core calculated with Eq. (7.15).

In Fig. 7.9 the plots show that the largest masses of fluid are transported in the bolus for critical slopes. Variation of either ridge height or Fr influences the results but if these two parameters are constant between simulations the mass transported in the bolus will be less for slopes other than critical. These results give another example of how critical slopes concentrate the internal wave energy and create conditions for increased mixing. In addition to the clear influence of slope the plots in this figure reinforce the importance Froude number dependence discussed in the previous sections. The amount of mass contained by the bolus cores is less for both of the shorter and tall ridges. In the case of the smaller ridge this is likely a result of less ridge slope to interact with the internal wave and concentrate the wave energy. Most of the internal wave simply passes over the top of the ridge and less mass is transported as a result. Additional energy is needed for mass to reach the top of the tallest ridge. If the slope and Froude number are held constant the same amount of energy, or more, is directed on to the slope as in the case with $h_t/d = 0.5$. The bolus core generated must be transported to a location higher in the domain resulting in additional work against gravity reducing the size of the bolus before the peak of the ridge.

Once the bolus reaches the peak of the ridge in addition to kinetic energy the bolus now has potential energy. At the top of the ridge the dense core created by the internal wave interaction on the upstream side of the topography is surrounded by fluid of lower density and will start to progress down the backside of the ridge. The boluses analyzed by Venayagamoorthy & Fringer (2007) were shown to slow and decrease in size as they traveled along the shelf once they had

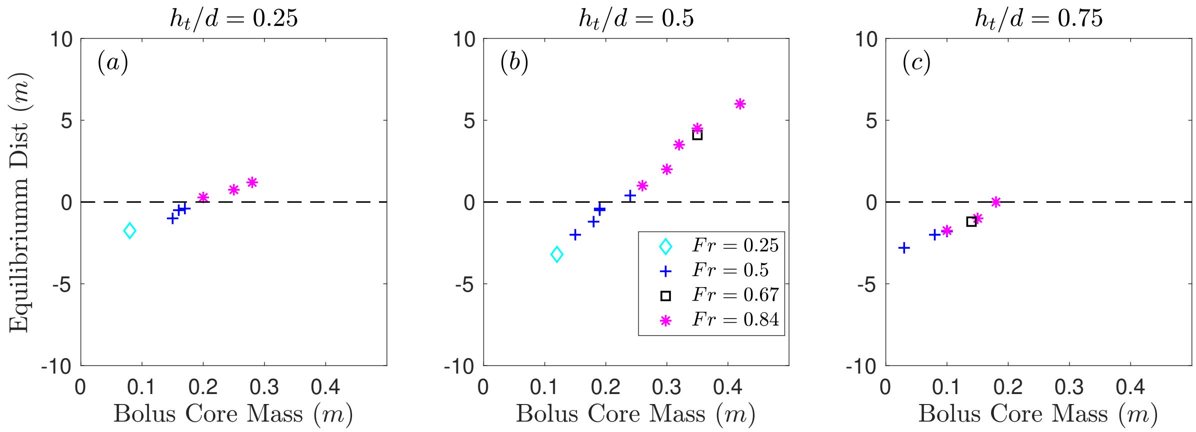

Figure 7.10: Distance travelled relative to the equilibrium position in the stratification of density of the bolus core.

reached the top of the slope. Here, the boluses are essentially similar to gravity currents as they travel down the back-slope of the ridge. These boluses have additional momentum then is considered in most analyses of gravity currents. Bolus cores will be composed by fluid of certain density depending the flow conditions set by the parameters. As it travels down the back side of ridge it will decrease in size, as shown by Venayagamoorthy & Fringer (2007) for a shelf. In the simplest case presented here the bolus will be dissipated by eddies at the level of stratification that has the same density of the bolus core. Additional momentum inherent to large boluses create conditions where the bolus will pass the level of stratification equal to the bolus core, entraining lighter fluid and generating mixing. This was qualitatively observed and discussed in Section 7.3.1. The two main types of gravity currents are intrusive gravity currents (IGC) that travels through an ambient fluid at the level of neutral buoyancy and bottom boundary gravity currents (BBGC) that travel along a solid boundary. Both types of gravity currents can significantly contribute to turbulence and mixing through entrainment flow. However, most studies of gravity currents on sloping bottom topography have been conducted within a homogenous fluid Simpson (1999). In these simulations, both types of classifications present.

Figure 7.10 plots the distance traveled by the bolus core relative to the equilibrium position of the fluid in the bolus core as a function of the previously derived dimensionless mass. The distance of travel of the bolus core was determined by taking a control volume surrounding the bolus core at the peak of the ridge, centering the control volume on the bolus and following it as it plunges off of the ridge. Once the density contained within this control volume was with 20% of the density of the background stratification contained by the same volume the bore was considered mixed. This threshold for determining destruction of the bore by the stratification or the turbulence is inexact, but was confirmed qualitatively by observations of the state of the bore at this threshold across the simulations analyzed. In Fig. 7.10 note that simulations with $Fr = 0.1$ are not included as they did not create this structure for analysis. Distance traveled by a bolus before mixing is strongly dependent on its mass where the larger the mass the further the distance it is able to travel. If the dimensionless mass of the bolus is greater 0.25 the bore will maintain sufficient momentum to pass its equilibrium position within the stratified fluid profile. When the dimensionless mass of the bore is around 0.2 the bore will tend toward becoming an intrusive gravity current and mixing at its equilibrium stratification level. Below this threshold the bolus will maintain contact with the slope and be mixed by frictional and viscous processes before it reaches its level of equilibrium stratification. While the previous sections of analysis have shown the relative importance of parameters this figure quantifies a measure of the region around a topographic ridge that will be impacted by bore propagation. In realistic topography many lesser ridges and prominent topographic points off of the main ridge peak are likely impacted by these types of structures in locations subjected to barotropic tides.

7.4 Summary/Conclusion

Observation and simulation of internal wave interaction with topography is an area of research that has received significant recent attention. This research furthers the understanding of the dynamics of internal wave interaction with a single ridge through a parametric study using numerical simulation. While imperative to understanding of ocean dynamics, field observation and measurement are limited by temporal and spatial resolution. Laboratory simulations are limited by scale and measurement limitations. With increases in computational power, numerical simulations have become a very important tool for understanding the processes and dynamics internal to the ocean.

A CFD simulation simply applies the governing equations derived from the salient physics. Up until this point the majority of numerical simulations of these processes have been studied using detailed DNS or LES simulations completed at the laboratory scale or very large scale LES or RANS simulations focusing on the bulk flow at field realistic scales. Here we present a set of detailed numerical simulations of internal wave-topography interactions at the intermediate scale to further our understanding of the dynamics but also to show that the local flow dynamics seen in the laboratory scale simulations translate to larger scales.

Qualitatively the range of results within the parametric framework are presented and discussed. Increased amplitude of incident internal waves leads to more instability, mixing and a more significant distribution of time integrated dissipation tendency. Importance of a critical slope in the concentration of internal wave energy and the partition of the energy into higher wave modes is also confirmed at the intermediated scale. Significant differences between the internal wave amplitude and the topographic amplitude, investigated by modification of h_t/d and Froude number influence the dynamics. Wave and topographic amplitudes of similar scale resulting in the most dynamic flows and mixing.

Internal bolus structures that form by this interaction have been observed in the field and simulated in detail at the laboratory scale (Venayagamoorthy & Fringer, 2007). In these simulations we see an equivalent partition of internal wave modes and a similar concentration of energy leading to the development of boluses that are ejected up and over the top of the topographic ridge. Strength of the bolus is shown to be a function of the mass of the structure, which increases as a function of increased Froude numbers. Within the parametric space, dynamics of flow leading to mixing and fluid transport by these boluses is strongly correlated with critical slope topography. Conditions allowing for the formation of boluses using linear theory is corroborated for these simulations at the intermediate scale. Variations in the topographic ridge height decreased the amount of mixing and the formation of bores. Smaller topography reduced the scale of interaction between the waves and ridge and less dynamic flows developed. Larger ridges, with amplitudes greater than most of the internal waves, blocked the flow and confined the bulk of the mixing to the front side of the ridge.

Analysis of bolus propagation past the ridge peak highlights a similarity to gravity currents, both in scaling and in the propagation dynamics. Structures analogous to intrusive gravity currents and bottom boundary gravity currents are observed to occur in the simulations. Formations of these two different types of gravity current is shown to be dependent on the mass of the propagating bolus core. Distance along the simulations boundary where mixing is influenced by the bolus propagation is also determined to be a function of the bolus mass. This study provides a detailed analysis of the interaction dynamics at the intermediate scale, providing a much needed bridge in the gap of study between simulations at the laboratory scale and the field scale. Laboratory scale simulations are the focus of theoretical analysis of the fluid mechanics and theory. Field scale simulations are the focus of field scientists and engineers focused on realistic scale processes. By maintaining simulation resolution that is able to resolve the majority of the flow dynamics and structure with a tool used by field scale modelers we hope this research provides at least the start of a bridge in the simulation scale gap. As the computational power of readily available resources continues to increase we theorize that simulations investigating this intermediate space will also see increased attention, eventually bridging the gap completely where detailed flow structures can be solved for in full field scale models.

Chapter 8

Summary & Conclusions

8.1 Investigation Summary

The work presented in this dissertation uses computational fluid dynamics to study turbulent dynamics of internal waves in a stratified fluid. Simulations and analysis completed can be categorized into two distinct types: direct numerical simulations(DNS) at the laboratory scale and pseudo large eddy simulations (LES) of internal wave interactions with bottom topography at an intermediate scale. The DNS studies apply scalings of dimensionless parameters to illustrate and inform the impact of common assumptions made in estimates of turbulent quantities from field measurements and the impact of commonly applied assumptions in parametric analysis of stratified flow turbulence. The pseudo-LES is used to analyze the structure and energy of internal wave interactions with bottom topography.

Chapters 1 introduces the field of study and the objectives of the dissertation. Chapter 2 covers the governing equations, theoretical scales of turbulence and field measurement techniques. Chapter 3 details past work through a literature review of stratified flow turbulence and internal waves covering nomenclature, flow classification, relevant non-dimensional parameters and recent relevant work that this dissertation analysis builds on.

In Chapter 4 DNS scaling analysis is used to illustrate the impacts of application of the Osborn model to field measurements for estimates of the diapycnal diffusivity. Use of the Osborn model for estimation of turbulent quantities has a clear impact on the scaling when DNS results are compared to results as they would be derived from field measurements. While this widespread method of estimating the diapycnal diffusivity using the Osborn model is not found to diverge entirely from the values calculated directly from the DNS, this analysis for the first time comprehensively shows that an assumption of $\Gamma = 0.2$ is in fact an artifact of error cancellation resulting from making several nebulous assumptions.

In Chapter 5 DNS results are used to evaluate the impact of Coriolis rotation f on the turbulent scales in stratified flows. All internal waves have a frequency in between the Coriolis frequency and the buoyancy frequency N. The ambiguity of the ratio of these two parameters is shown clearly within a parametric space using scaling arguments to evaluate the degree of turbulence and mixing. While the Coriolis rotation f clearly influences the dynamics and structure of inertial gravity waves in this analysis no clear impact on the turbulent quantities and specifically on the turbulent mixing coefficient.

Chapter 6 shows the detailed energetics of a 40 simulation parametric study of nonhydrostatic internal wave interaction with a ridge in two dimensions. This study fills a gap in the simulation space by completing the simulations at an intermediate scale, between the laboratory and field scales. The energetics observed in detailed simulations at the laboratory scale are observed even with the reduced resolution needed for these computations.

Chapter 7 focuses on the flow structure of the 40 simulations presented in Chapter 7 in addition to 3 three-dimensional simulations. Conditions for the formation of propagating bolus structures are observed and defined at the intermediate scales of the simulations. In addition, the height of fluid displacement, mass and distance travelled by the boluses generated in the simulations are all quantified and discussed showing the importance of these structures in stratified flows. These simulations detail many of the flow structures seen at a higher resolution using MITgcm, a tool predominantly used by and trusted by field scientists for field scale simulations.

8.2 Key Findings

The following summarizes the main contributions of this study as presented in Chapters 4-7.

1. The Osborn model $K_\rho = \Gamma(\epsilon/N^2)$ is commonly applied to estimate diapycnal eddy diffusivity. Diapycnal diffusivity can not be directly measured in the ocean and must be inferred from other measurements and assumptions. One of the most common assumptions is that the irreversible mixing coefficient is constant $\Gamma = 0.2$. Comparing the impact of this assumption as compared to the value calculated directly from the DNS show how the diffusivities will be

severely over- or underestimated for strongly and weakly stratified flows. This analysis leads to a better understanding of the relationship of irreversible process in stratified flow and what flow conditions can result in an under- or over-estimate of Γ used in parameterizations for mixing in larger models.

2. Inference of the kinetic energy dissipation rate ϵ using the Ellison scale and the Thorpe scale result in overestimates of the diapycnal diffusivity by up to one-order of magnitude when compared to the DNS values. This analysis shows for the first time that the common assumptions that were assumed to be a constant function of the flow are in fact a result of error cancellations. The results presented provide a tool, in conjunction with the analysis presented by Garanaik & Venayagamoorthy (2019), that can be used to obtain realistic values for diapycnal diffusivity from quantities directly measured in the field without the simplifying assumptions applied to the unmeasured turbulent quantities. These results will influence the determination of the type flow quantities measured by field scientists and will improve estimations of secondary quantities calculated from these measurements resulting in more accurate and informed estimates of mixing.

3. The ratio of the buoyancy (N) and Coriolis (f) frequencies has been frequently used for the flow classification of regimes in rotating-stratified-turbulence (RST). Analysis using a framework comparing N and f shows a that definitively shows this ratio is ambiguous and should not be used for flow classification. The framework is defined as a function of the turbulent Froude number and the turbulent Rossby number and implements a regimes classification as a function of the relative strength of rotation and stratification, terminology refined from Aluie & Kurien (2011). This analysis clearly shows that DNS defined by very different magnitudes of the turbulent Froude number can have the same N/f ratio.

4. DNS of stratified turbulence (and rotating stratified turbulence) sometimes generate values for certain quantities that are physically unrealistic. Through evaluation of calculated diapycnal diffusivity K_ρ a parameter termed the diffusivity ratio $\hat{\kappa}$ is proposed to ensure real

values are being used in studies derived from DNS. This quantity is defined by the ratio of the turbulent diffusivity to the molecular diffusivity and must be at least one order of magnitude greater than one if the results are representative of actual flows. $\hat{\kappa} > O(10)$ is a necessary condition for realistic turbulent mixing to be produced in DNS results. This tool aims to help set guidelines for realistic simulations and lead to more widespread acceptance of DNS as a tool for gaining insights and developing parameterizations for turbulent mixing in stratified flows. Ensuring that simulations reach realistically observable thresholds defined by $\hat{\kappa}$ will help build trust in theoretical models showing that the analysis is physically realistic.

5. DNS results show that inclusion of Coriolis rotation f as a forcing parameter does not influence the framework developed by Garanaik & Venayagamoorthy (2019) for determining the irreversible mixing coefficient Γ. This result is important as it shows rotation plays limited to no role at the scales of mixing. These findings show how simulations can be used as a tool for improved estimates of ocean mixing quantities from measurements as well as how DNS evaluation can be improved with direct consideration of applicability to the field or laboratory setting.

6. Interaction of an internal wave with topography results in a percentage of a wave's energy being reflected, dissipated and transmitted past the topography. Detailed evaluation of energy using forty nonhydrostatic two-dimensional simulations show that differences in ridge height, ridge slope and the velocity amplitude of forcing all influence the internal wave-topography interaction. Similar analysis has been completed for shelf topography at the laboratory scale. This analysis presents a detailed analysis for a ridge, varies ridge height and shows similar results at a lower resolution and much larger scale simulation. Velocity amplitude of forcing and slope criticality are shown to be the most influential parameters of the partition of wave energy. This analysis also shows that models can obtain similar results to DNS without resolving turbulence and works toward finding a modeling middle ground where the level of flow resolution is sufficiently detailed to analyze flow structure without resolution that resolves turbulent scales.

7. Formation of bolus structures that form dense cores that advect fluid up and over the crest of the ridge have been observed in the field, in the laboratory and in simulations. New analysis detailing the bolus behavior after the crest of the ridge is presented for the first time. Vertical displacement of fluid, core mass and distance travelled are all evaluated as a function of simulation parameters. Increases in available computational resources have made simulations at the intermediate scale that resolve significant portions of the flow structures present in the flow possible and highlight how flow behavior observed at the laboratory scale is realistic even with increased scale. This analysis increases our understanding of the distribution of these flow structures and the dynamics they induce near the topographic boundary where it is difficult to measure such phenomena. With these simulations targeted measurement can be made near the boundary and compared to these results. This analysis provides tools to help build a bridge in the understanding of stratified turbulence between the theoreticians and field scientists.

8.3 Suggestions For Future Work

As the availability and power of computational resources increase, both resolution and scale of simulations will also be able to increase. Simulations eventually will be able to resolve eddies and turbulent structures at realistic field scales to refine our understanding of these processes. Due to the complexity of field measurements of turbulence in oceanic flows, numerical simulations will remain one of the most important tools for the study and understanding of stratified turbulent flows. Field observation and validation would enhance the findings of this research.

Beside increases in resolution and scale of simulated flows, different topographic distributions could be simulated to increase our understanding of internal wave-topography interaction. Many hotspots for internal wave breaking are situated near island/seamount chains or oceanic ridges. These locations are more complex than the isolated ridge presented in this study. A single Gaussian-type seamount, distributions of Gaussian type seamounts, multiple ridges with varied relative height and spacing as well as scaled real topography all represent realistic scenarios that would benefit from further studies using eddy resolving simulations.

In this analysis DNS were examined and used as a tool to evaluate field measurement methods and assumptions. Using the internal wave topography simulation data, ‘simulated’ field sampling and analysis could be conducted. If data was extracted from these simulations as it would be in a field campaign, analysis could be completed and compared to true data values from the simulation, synthesizing the findings and methods presented in this dissertation.

References

Aguilar, D., & Sutherland, B. (2006). Internal wave generation from rough topography. *Physics of Fluids*, *18*(6), 066603.

Aguilar, D., Sutherland, B., & Muraki, D. (2006). Laboratory generation of internal waves from sinusoidal topography. *Deep Sea Research Part II: Topical Studies in Oceanography*, *53*(1-2), 96–115.

Alford, M., Girton, J. B., Voet, G., Carter, G. S., Mickett, J. B., & Klymak, J. M. (2013). Turbulent mixing and hydraulic control of abyssal water in the samoan passage. *Geophysical Research Letters*, *40*(17), 4668–4674.

Alford, M., MacKinnon, J., Zhao, Z., Pinkel, R., Klymak, J., & Peacock, T. (2007). Internal waves across the pacific. *Geophysical Research Letters*, *34*(24).

Althaus, A. M., Kunze, E., & Sanford, T. B. (2003). Internal tide radiation from mendocino escarpment. *Journal of Physical Oceanography*, *33*(7), 1510–1527.

Aluie, H., & Kurien, S. (2011). Joint downscale fluxes of energy and potential enstrophy in rotating stratified boussinesq flows. *Europhysics Letters*, *96*(4), 44006.

Ambaum, M. H., & Marshall, D. P. (2005). The effects of stratification on flow separation. *Journal of the atmospheric sciences*, *62*(7), 2618–2625.

Armi, L., & Mayr, G. J. (2011). The descending stratified flow and internal hydraulic jump in the lee of the sierras. *Journal of Applied Meteorology and Climatology*, *50*(10), 1995–2011.

Arthur, R. S., Venayagamoorthy, S., Koseff, J. R., & Fringer, O. B. (2017). How we compute n matters to estimates of mixing in stratified flows. *Journal of Fluid Mechanics*, *831*.

Baines, P. G. (1987). Upstream blocking and airflow over mountains. *Annual review of fluid mechanics*, *19*(1), 75–95.

Baines, P. G. (1998). *Topographic effects in stratified flows*. Cambridge university press.

Balmforth, N., Ierley, G., & Young, W. (2002). Tidal conversion by subcritical topography. *Journal of Physical Oceanography*, *32*(10), 2900–2914.

Bell, T. (1975). Lee waves in stratified flows with simple harmonic time dependence. *Journal of Fluid Mechanics*, *67*(4), 705–722.

Bell Jr, T. (1975). Topographically generated internal waves in the open ocean. *Journal of Geophysical Research*, *80*(3), 320–327.

Bouffard, D., & Boegman, L. (2013). A diapycnal diffusivity model for stratified environmental flows. *Dynamics of Atmospheres and Oceans*, *61*, 14–34.

Brethouwer, G., Billant, P., Lindberg, E., & Chomaz, J. M. (2007). Scaling analysis and simulation of strongly stratified turbulent flows. *Journal of Fluid Mechanics*, *585*, 343-368.

Brethouwer, G., Billant, P., Lindborg, E., & Chomaz, J.-M. (2007). Scaling analysis and simulation of strongly stratified turbulent flows. *Journal of Fluid Mechanics*, *585*, 343–368.

Cacchione, D., & Wunsch, C. (1974). Experimental study of internal waves over a slope. *Journal of Fluid Mechanics*, *66*(2), 223–239.

Carter, G. S., Gregg, M. C., & Lien, R.-C. (2005). Internal waves, solitary-like waves, and mixing on the monterey bay shelf. *Continental Shelf Research*, *25*(12-13), 1499–1520.

Chen, C.-Y. (2009). Amplitude decay and energy dissipation due to the interaction of internal solitary waves with a triangular obstacle in a two-layer fluid system: the blockage parameter. *Journal of Marine Science and Technology*, *14*(4), 499.

Chen, C.-Y., Hsu, J. R.-C., Cheng, M.-H., & Chen, C.-W. (2008). Experiments on mixing and dissipation in internal solitary waves over two triangular obstacles. *Environmental Fluid Mechanics*, *8*(3), 199–214.

Chow, F. K., & Street, R. L. (2004). Explicit filtering and reconstruction turbulence modeling for large-eddy simulations of field-scale flows. *Adv. Hydro-Sci. Eng*, *6*, 1–12.

Cimatoribus, A. A., van Haren, H., & Gostiaux, L. (2014). Comparison of ellison and thorpe scales from e ulerian ocean temperature observations. *Journal of Geophysical Research: Oceans*, *119*(10), 7047–7065.

Cummins, P. F., Armi, L., & Vagle, S. (2006). Upstream internal hydraulic jumps. *Journal of Physical Oceanography*, *36*(5), 753–769.

Cushman-Roisin, B., & Beckers, J.-M. (2008). *Introduction to geophysical fluid dynamics.* Accademic Press, Cambridge.

Danaila, L., Voivenel, L., & Varea, E. (2017). Self-similarity criteria in anisotropic flows with viscosity stratification. *Physics of Fluids*, *29*(2), 020716.

Dauxois, T., Didier, A., & Falcon, E. (2004). Observation of near-critical reflection of internal waves in a stably stratified fluid. *Physics of Fluids*, *16*(6), 1936–1941.

de Bruyn Kops, S. M. (2019). The effects of stable stratification on the decay of initially isotropic homogeneous turbulence. *Journal of Fluid Mechanics*, *860*, 787-821.

Dillon, T. M. (1982). Vertical overturns: A comparison of thorpe and ozmidov length scales. *Journal of Geophysical Research: Oceans*, *87*(C12), 9601–9613.

Di Lorenzo, E., Young, W. R., & Smith, S. L. (2006). Numerical and analytical estimates of m 2 tidal conversion at steep oceanic ridges. *Journal of physical oceanography*, *36*(6), 1072–1084.

Ding, L., Calhoun, R. J., & Street, R. L. (2003). Numerical simulation of strongly stratified flow over a three-dimensional hill. *Boundary-Layer Meteorology*, *107*(1), 81–114.

Dohan, K. (2004). *Internal wave generation from a turbulent mixed region* (Unpublished doctoral dissertation). University of Alberta.

Drazin, P. G. (1961). On the steady flow of a fluid of variable density past an obstacle. *Tellus*, *13*(2), 239–251.

Dupont, P., Kadri, Y., & Chomaz, J.-M. (2001). Internal waves generated by the wake of gaussian hills. *Physics of Fluids*, *13*(11), 3223–3233.

Ecke, R. E., & Niemela, J. J. (2014). Heat transport in the geostrophic regime of rotating rayleigh-bénard convection. *Physical Review Letters*, *113*(11), 114301.

Ellison, T. (1957). Turbulent transport of heat and momentum from an infinite rough plane. *Journal of Fluid Mechanics*, *2*(5), 456–466.

Feraco, F., Marino, R., Pumir, A., Primavera, L., Mininni, P. D., Pouquet, A., & Rosenberg, D. (2018). Vertical drafts and mixing in stratified turbulence: Sharp transition with froude number. *Europhysics Letters*, *123*(4), 44002.

Fontana, M., Bruno, O. P., Mininni, P. D., & Dmitruk, P. (2020). Fourier continuation method for incompressible fluids with boundaries. *Comp. Phys. Comm.*, *256*, 107482.

Fringer, O. B., & Street, R. L. (2003). The dynamics of breaking progressive interfacial waves. *Journal of Fluid Mechanics*, *494*, 319–353.

Galperin, B., Kantha, L., Mellor, G., & Rosati, A. (1989). Modeling rotating stratified turbulent flows with application to oceanic mixed layers. *Journal of Physical Oceanography*, *19*(7), 901–916.

Garanaik, A. (2018). *Mixing in stably stratified turbulent flows: improved parameterizations of diapycnal mixing in oceanic flows* (Unpublished doctoral dissertation). Colorado State University.

Garanaik, A., & Venayagamoorthy, S. (2018). Assessment of small-scale anisotropy in stably stratified turbulent flows using direct numerical simulations. *Physics of Fluids*, *30*, 126602.

Garanaik, A., & Venayagamoorthy, S. (2019). On the inference of the state of turbulence and mixing efficiency in stably stratified flows. *Journal of Fluid Mechanics*, *867*, 323–333.

Gargett, A. E. (1988). The scaling of turbulence in the presence of stable stratification. *Journal of Geophysical Research: Oceans*, *93*(C5), 5021–5036.

Garrett, C., & Kunze, E. (2007). Internal tide generation in the deep ocean. *Annu. Rev. Fluid Mech.*, *39*, 57–87.

Gayen, B., & Sarkar, S. (2011). Direct and large-eddy simulations of internal tide generation at a near-critical slope. *Journal of Fluid Mechanics*, *681*, 48–79.

Gerkema, T., Staquet, C., & Bouruet-Aubertot, P. (2006). Decay of semi-diurnal internal-tide beams due to subharmonic resonance. *Geophysical research letters*, *33*(8).

Gill, A. E. (2016). *Atmosphereocean dynamics*. Elsevier.

Grant, H., Stewart, R., & Moilliet, A. (1962). Turbulence spectra from a tidal channel. *Journal of Fluid Mechanics*, *12*(2), 241–268.

Gregg, M. (1987). Diapycnal mixing in the thermocline: A review. *Journal of Geophysical Research: Oceans*, *92*(C5), 5249–5286.

Gregg, M. (1989). Scaling turbulent dissipation in the thermocline. *Journal of Geophysical Research: Oceans*, *94*(C7), 9686–9698.

Gregg, M., D'Asaro, E., Riley, J., & Kunze, E. (2018). Mixing efficiency in the ocean. *Annual review of marine science*, *10*, 443–473.

Gregg, M., & Pratt, L. J. (2010). Flow and hydraulics near the sill of hood canal, a strongly sheared, continuously stratified fjord. *Journal of Physical Oceanography*, *40*(5), 1087–1105.

Hall, R. A., Huthnance, J. M., & Williams, R. G. (2013). Internal wave reflection on shelf slopes with depth-varying stratification. *Journal of Physical Oceanography*, *43*(2), 248–258.

Hebert, D., & de Bruyn Kops, S. M. (2006). Relationship between vertical shear rate and kinetic energy dissipation rate in stably stratified flows. *Geophysical Research Letters*, *33*, L06602.

Helfrich, K. R. (1992). Internal solitary wave breaking and run-up on a uniform slope. *Journal of Fluid Mechanics*, *243*, 133–154.

Holford, J. M., & Linden, P. (1999). Turbulent mixing in a stratified fluid. *Dynamics of atmospheres and oceans*, *30*(2-4), 173–198.

Hult, E., Troy, C., & Koseff, J. (2011). The mixing efficiency of interfacial waves breaking at a ridge: 2. local mixing processes. *Journal of Geophysical Research: Oceans*, *116*(C2).

Hult, E., Troy, C. D., & Koseff, J. R. (2009). The breaking of interfacial waves at a submerged bathymetric ridge. *Journal of Fluid Mechanics*, *637*, 45–71.

Hunt, J., & Snyder, W. (1980). Experiments on stably and neutrally stratified flow over a model three-dimensional hill. *Journal of Fluid Mechanics*, *96*(4), 671–704.

Huppert, H. E., & Miles, J. W. (1969). Lee waves in a stratified flow part 3. semi-elliptical obstacle. *Journal of Fluid Mechanics*, *35*(3), 481–496.

Ijichi, T., & Hibiya, T. (2018). Observed variations in turbulent mixing efficiency in the deep ocean. *Journal of Physical Oceanography*, *48*(8), 1815–1830.

Itsweire, E., Koseff, J., Briggs, D., & Ferziger, J. (1993). Turbulence in stratified shear flows: Implications for interpreting shear-induced mixing in the ocean. *Journal of physical oceanography*, *23*(7), 1508–1522.

Ivey, G., & Imberger, J. (1991). On the nature of turbulence in a stratified fluid. part i: The energetics of mixing. *Journal of Physical Oceanography*, *21*(5), 650–658.

Ivey, G., & Nokes, R. (1989). Vertical mixing due to the breaking of critical internal waves on sloping boundaries. *Journal of Fluid Mechanics*, *204*, 479–500.

Ivey, G., Winters, K., & De Silva, I. (2000). Turbulent mixing in a sloping benthic boundary layer energized by internal waves. *Journal of Fluid Mechanics*, *418*, 59–76.

Jalali, M., & Sarkar, S. (2017). Large eddy simulation of flow and turbulence at the steep topography of luzon strait. *Geophysical Research Letters*, *44*(18), 9440–9448.

Jalali, M., VanDine, A., Chalamalla, V. K., & Sarkar, S. (2017). Oscillatory stratified flow over supercritical topography: Wave energetics and turbulence. *Computers & Fluids*, *158*, 39–48.

Jarosz, E., Wijesekera, H. W., Teague, W. J., Fribance, D. B., & Moline, M. A. (2014). Observations on stratified flow over a bank at low froude numbers. *Journal of Geophysical Research: Oceans*, *119*(9), 6403–6421.

Javam, A., Imberger, J., & Armfield, S. (1999). Numerical study of internal wave reflection from sloping boundaries. *Journal of Fluid Mechanics*, *396*, 183–201.

Kantha, L., Rosati, A., & Galperin, B. (1989). Effect of rotation on vertical mixing and associated turbulence in stratified fluids. *Journal of Geophysical Research: Oceans*, *94*(C4), 4843–4854.

Khatiwala, S. (2003). Generation of internal tides in an ocean of finite depth: analytical and numerical calculations. *Deep Sea Research Part I: Oceanographic Research Papers*, *50*(1), 3–21.

King, B. T. (2010). *Laboratory and numerical studies of internal wave generation and propagation in the ocean* (Unpublished doctoral dissertation).

Klymak, J. M., Legg, S., Alford, M., Buijsman, M., Pinkel, R., & Nash, J. D. (2012). The direct breaking of internal waves at steep topography. *Oceanography*, *25*(2), 150–159.

Klymak, J. M., Moum, J. N., Nash, J. D., Kunze, E., Girton, J. B., Carter, G. S., … Gregg, M. C. (2006). An estimate of tidal energy lost to turbulence at the hawaiian ridge. *Journal of Physical Oceanography*, *36*(6), 1148–1164.

Kolmogorov, A. N. (1941). The local structure of turbulence in incompressible viscous fluid for very large reynolds numbers. In *Dokl. akad. nauk sssr* (Vol. 30, pp. 299–303).

Kundu, P. K., Cohen, I. M., & Dowling, D. (2008). *Fluid mechanics 4th*. Elsevier.

Kunze, E., Firing, E., Hummon, J. M., Chereskin, T. K., & Thurnherr, A. M. (2006). Global abyssal mixing inferred from lowered adcp shear and ctd strain profiles. *Journal of Physical Oceanography*, *36*(8), 1553–1576.

Kunze, E., & Sanford, T. B. (1996). Abyssal mixing: Where it is not. *Journal of Physical Oceanography*, *26*(10), 2286–2296.

Kunze, E., & Smith, S. G. L. (2004). The role of small-scale topography in turbulent mixing of the global ocean. *Oceanography*, *17*(1), 55–64.

Kurien, S., & Smith, L. M. (2014). Effect of rotation and domain aspect-ratio on layer formation in strongly stratified boussinesq flows. *Journal of Turbulence*, *15*(4), 241–271.

Lamb, K. G. (2014). Internal wave breaking and dissipation mechanisms on the continental slope/shelf. *Annual Review of Fluid Mechanics*, *46*, 231–254.

Ledwell, J. R., St. Laurent, L. C., Girton, J. B., & Toole, J. M. (2011). Diapycnal mixing in the antarctic circumpolar current. *Journal of Physical Oceanography*, *41*(1), 241–246.

Legg, S. (2004a). Internal tides generated on a corrugated continental slope. part i: Cross-slope barotropic forcing. *Journal of Physical Oceanography*, *34*(1), 156–173.

Legg, S. (2004b). Internal tides generated on a corrugated continental slope. part ii: Along-slope barotropic forcing. *Journal of Physical Oceanography*, *34*(8), 1824–1838.

Legg, S. (2014). Scattering of low-mode internal waves at finite isolated topography. *Journal of Physical Oceanography*, *44*(1), 359–383.

Legg, S., & Adcroft, A. (2003). Internal wave breaking at concave and convex continental slopes. *Journal of Physical Oceanography*, *33*(11), 2224–2246.

Legg, S., & Huijts, K. M. (2006). Preliminary simulations of internal waves and mixing generated by finite amplitude tidal flow over isolated topography. *Deep Sea Research Part II: Topical Studies in Oceanography*, *53*(1-2), 140–156.

Legg, S., & Klymak, J. (2008). Internal hydraulic jumps and overturning generated by tidal flow over a tall steep ridge. *Journal of Physical Oceanography*, *38*(9), 1949–1964.

Lelong, M.-P., & Sundermeyer, M. A. (2005). Geostrophic adjustment of an isolated diapycnal mixing event and its implications for small-scale lateral dispersion. *Journal of physical oceanography*, *35*(12), 2352–2367.

Levine, M. D., & Boyd, T. J. (2006). Tidally forced internal waves and overturns observed on a slope: Results from home. *Journal of physical oceanography*, *36*(6), 1184–1201.

Lighthill, M. J., & Lighthill, J. (2001). *Waves in fluids*. Cambridge university press.

Lilly, D., & Klemp, J. (1979). The effects of terrain shape on nonlinear hydrostatic mountain waves. *Journal of Fluid Mechanics*, *95*(2), 241–261.

Lindborg, E., & Brethouwer, G. (2008). Vertical dispersion by stratified turbulence. *Journal of Fluid Mechanics*, *614*, 303–314.

Linden, P., & Redondo, J. (1991). Molecular mixing in rayleigh–taylor instability. part i: global mixing. *Physics of Fluids A: Fluid Dynamics*, *3*(5), 1269–1277.

Llewellyn Smith, S. G., & Young, W. (2002). Conversion of the barotropic tide. *Journal of Physical Oceanography*, *32*(5), 1554–1566.

Long, R. R. (1953). Some aspects of the flow of stratified fluids: I. a theoretical investigation. *Tellus*, *5*(1), 42–58.

Long, R. R. (1972). Finite amplitude disturbances in the flow of inviscid rotating and stratified fluids over obstacles. *Annual Review of Fluid Mechanics*, *4*(1), 69–92.

Lueck, R. G., Wolk, F., & Yamazaki, H. (2002). Oceanic velocity microstructure measurements in the 20th century. *Journal of Oceanography*, *58*(1), 153–174.

Lyra, G. (1943). Theorie der stationären leewellenströmung in freier atmosphäre. *ZAMM-Journal of Applied Mathematics and Mechanics/Zeitschrift für Angewandte Mathematik und Mechanik*, *23*(1), 1–28.

Maffioli, A., Brethouwer, G., & Lindborg, E. (2016a). Mixing efficiency in stratified turbulence. *Journal of Fluid Mechanics*, *794*, R3.

Maffioli, A., Brethouwer, G., & Lindborg, E. (2016b). Mixing efficiency in stratified turbulence. *Journal of Fluid Mechanics*, *794*.

Maffioli, A., & Davidson, P. (2016). Dynamics of stratified turbulence decaying from a high buoyancy reynolds number. *Journal of Fluid Mechanics*, *786*, 210–233.

Malalasekera, W., & Versteeg, H. (2007). An introduction to computational fluid dynamics. *The finite volume method, Harlow: Prentice Hall*, 1995.

Marino, R., Mininni, P. D., Rosenberg, D., & Pouquet, A. (2013). Inverse cascades in rotating stratified turbulence: fast growth of large scales. *EPL (Europhysics Letters)*, *102*(4), 44006.

Marino, R., Mininni, P. D., Rosenberg, D., & Pouquet, A. (2014). Large-scale anisotropy in stably stratified rotating flows. *Physical Review E*, *90*, 023018.

Marino, R., Pouquet, A., & Rosenberg, D. (2015). Resolving the paradox of oceanic large-scale balance and small-scale mixing. *Physical Review Letters*, *114*(11), 114504.

Marino, R., Rosenberg, D., Herbert, C., & Pouquet, A. (2015). Interplay of waves and eddies in rotating stratified turbulence and the link with kinetic-potential energy partition. *EuroPhysics Letters*, *112*, 49001.

Marshall, J., Adcroft, A., Hill, C., Perelman, L., & Heisey, C. (1997). A finite-volume, incompressible navier stokes model for studies of the ocean on parallel computers. *Journal of Geophysical Research: Oceans*, *102*(C3), 5753–5766.

Mater, B. D., Schaad, S. M., & Venayagamoorthy, S. (2013). Relevance of the thorpe length scale in stably stratified turbulence. *Physics of Fluids*, *25*(7), 076604.

Mater, B. D., & Venayagamoorthy, S. (2014a). The quest for an unambiguous parameterization of mixing efficiency in stably stratified geophysical flows. *Geophysical Research Letters*, *41*(13), 4646–4653.

Mater, B. D., & Venayagamoorthy, S. (2014b). A unifying framework for parameterizing stably stratified shear-flow turbulence. *Physics of Fluids*, *26*(3), 036601.

Mininni, P. D., Rosenberg, D., Reddy, R., & Pouquet, A. (2011). A hybrid mpi–openmp scheme for scalable parallel pseudospectral computations for fluid turbulence. *Parallel Computing*, *37*(6-7), 316–326.

Monismith, S. G., Koseff, J. R., & White, B. L. (2018). Mixing efficiency in the presence of stratification: When is it constant? *Geophysical Research Letters*, *45*(11), 5627–5634.

Moum, J., & Smyth, W. (2006). The pressure disturbance of a nonlinear internal wave train. *Journal of Fluid Mechanics*, *558*, 153–177.

Munk, W. (1966). Abyssal recipes. In *Deep sea research and oceanographic abstracts* (Vol. 13, pp. 707–730).

Munk, W., & Wunsch, C. (1998). Abyssal recipes ii: Energetics of tidal and wind mixing. *Deep Sea Research Part I: Oceanographic Research Papers*, *45*(12), 1977–2010.

Muraki, D. J. (2011). Large-amplitude topographic waves in 2d stratified flow. *Journal of Fluid Mechanics*, *681*, 173–192.

Musgrave, R. C., Pinkel, R., MacKinnon, J., Mazloff, M. R., & Young, W. (2016). Stratified tidal flow over a tall ridge above and below the turning latitude. *Journal of Fluid Mechanics*, *793*, 933–957.

Nash, J. D., Kunze, E., Toole, J. M., & Schmitt, R. W. (2004). Internal tide reflection and turbulent mixing on the continental slope. *Journal of Physical Oceanography*, *34*(5), 1117–1134.

Nikurashin, M., & Ferrari, R. (2013). Overturning circulation driven by breaking internal waves in the deep ocean. *Geophysical Research Letters*, *40*(12), 3133–3137.

Nikurashin, M., & Legg, S. (2011). A mechanism for local dissipation of internal tides generated at rough topography. *Journal of Physical Oceanography*, *41*(2), 378–395.

Orlanski, I. (1976). A simple boundary condition for unbounded hyperbolic flows. *Journal of computational physics*, *21*(3), 251–269.

Osborn, T. R. (1980). Estimates of the local rate of vertical diffusion from dissipation measurements. *Journal of Physical Oceanography*, *10*(1), 83–89.

Osborn, T. R., & Cox, C. S. (1972). Oceanic fine structure. *Geophysical Fluid Dynamics*, *3*(4), 321–345.

Osborn, T. R., & Lueck, R. G. (1985). Turbulence measurements with a submarine. *Journal of physical oceanography*, *15*(11), 1502–1520.

Ozmidov, R. (1965). On the turbulent exchange in a stably stratified ocean. izv. acad. sci. ussr. *Atmos. Oceanic Phys.*, *1*, 861–871.

Peltier, W. R., & Caulfield, C. P. (2003). Mixing efficiency in stratified shear flows. *Annual Review Fluid Mechanics*, *35*, 135-167.

Pétrélis, F., Smith, S. L., & Young, W. (2006). Tidal conversion at a submarine ridge. *Journal of Physical Oceanography*, *36*(6), 1053–1071.

Phillips, O. M. (1977). The dynamics of the upper ocean.

Polzin, K. (2009). An abyssal recipe. *Ocean Modelling*, *30*(4), 298–309.

Polzin, K., Toole, J., Ledwell, J., & Schmitt, R. (1997). Spatial variability of turbulent mixing in the abyssal ocean. *Science*, *276*(5309), 93–96.

Pope, S. B. (2000). *Turbulent flows.* IOP Publishing.

Pouquet, A., Rosenberg, D., & Marino, R. (2019). Linking dissipation, anisotropy, and intermittency in rotating stratified turbulence at the threshold of linear shear instabilities. *Physics of Fluids*, *31*(10), 105116.

Pouquet, A., Rosenberg, D., Marino, R., & Herbert, C. (2018). Scaling laws for mixing and dissipation in unforced rotating stratified turbulence. *Journal of Fluid Mechanics*, *844*, 519–545.

Praud, O., Sommeria, J., & Fincham, A. M. (2006). Decaying grid turbulence in a rotating stratified fluid. *Journal of Fluid Mechanics*, *547*, 389–412.

Queney, P. (1947). *Theory of perturbations in stratified currents with applications to air flow over mountain barriers*. University of Chicago Press.

Ray, R. D., & Mitchum, G. T. (1996). Surface manifestation of internal tides generated near hawaii. *Geophysical Research Letters*, *23*(16), 2101–2104.

Richardson, L. F. (1922). *Weather prediction by numerical process*. Cambridge university press.

Riley, J. J., & de Bruyn Kops, S. M. (2003). Dynamics of turbulence strongly influenced by buoyancy. *Physics of Fluids*, *15(7)*, 2047-2059.

Riley, J. J., & Lelong, M.-P. (2000). Fluid motions in the presence of strong stable stratification. *Annual Review of Fluid Mechanics*, *32*, 613-657.

Riley, J. J., & Lindborg, E. (2013). *Recent progress in stratified turbulence - ten chapters in turbulence*. Cambridge University Press.

Riley, J. J., Metcalfe, R. W., & Weissman, M. A. (1981). Direct numerical simulations of homogeneous turbulence in density-stratified fluids. In *Aip conference proceedings* (Vol. 76, pp. 79–112).

Rorai, C., Mininni, P. D., & Pouquet, A. (2015). Stably stratified turbulence in the presence of large-scale forcing. *Physical Review E*, *92*(1), 013003.

Rosenberg, D., Marino, R., Herbert, C., & Pouquet, A. (2016). Variations of characteristic time scales in rotating stratified turbulence using a large parametric numerical study. *The European Physical Journal E*, *39*(1), 8.

Rosenberg, D., Marino, R., Herbert, C., & Pouquet, A. (2017). Correction to: Variations of characteristic time scales in rotating stratified turbulence using a large parametric numerical study. *The European Physical Journal E*, *40*(10), 87.

Rosenberg, D., Pouquet, A., Marino, R., & Mininni, P. D. (2015). Evidence for bolgiano-obukhov scaling in rotating stratified turbulence using high-resolution direct numerical simulations. *Physics of Fluids*, *27*(5), 055105.

Rudnick, D. L., & Klinke, J. (2007). The underway conductivity–temperature–depth instrument. *Journal of Atmospheric and Oceanic Technology*, *24*(11), 1910–1923.

Salehipour, H., & Peltier, W. R. (2015). Diapycnal diffusivity, turbulent Prandtl number and mixing efficiency in Boussinesq stratified turbulence. *Journal Fluid Mechanics*, *775*, 464-500.

Sarkar, S. (2003). The effect of stable stratification on turbulence anisotropy in uniformly sheared flow. *Computers & Mathematics with Applications*, *46*(4), 639–646.

Scorer, R. S. (1949). Theory of waves in the lee of mountains. *Quarterly Journal of the Royal Meteorological Society*, *75*(323), 41–56.

Scotti, A., & Pineda, J. (2004). Observation of very large and steep internal waves of elevation near the massachusetts coast. *Geophysical research letters*, *31*(22).

Shih, L. H., Koseff, J. R., Ivey, G. N., & Ferziger, J. H. (2005). Parameterization of turbulent fluxes and scales using homogeneous sheared stably stratified turbulence simulations. *Journal of Fluid Mechanics*, *525*, 193–214.

Shroyer, E., Moum, J., & Nash, J. (2009). Observations of polarity reversal in shoaling nonlinear internal waves. *Journal of Physical Oceanography*, *39*(3), 691–701.

Simpson, J. E. (1999). *Gravity currents: In the environment and the laboratory*. Cambridge university press.

Skyllingstad, E., & Wijesekera, H. (2003). Large-eddy simulation of flow over coastal ridges. In *Proceedings of the 13thaha hulikoa hawaiian winter workshop, honolulu, hi, university of hawaii at manoa* (pp. 107–109).

Slinn, D. N., & Levine, M. D. (2003). *Modeling internal tides and mixing over ocean ridges: Home analysis* (Tech. Rep.). FLORIDA UNIV GAINESVILLE DEPT OF CIVIL AND COASTAL ENGINEERING.

Slinn, D. N., & Riley, J. (1998). A model for the simulation of turbulent boundary layers in an incompressible stratified flow. *Journal of Computational Physics*, *144*(2), 550–602.

Smith, R. B. (1979). The influence of mountains on the atmosphere. In *Advances in geophysics* (Vol. 21, pp. 87–230). Elsevier.

Smith, R. B. (1985). On severe downslope winds. *Journal of the atmospheric sciences*, *42*(23), 2597–2603.

Smith, R. B. (1988). Linear theory of stratified flow past an isolated mountain in isosteric coordinates. *Journal of the atmospheric sciences*, *45*(24), 3889–3896.

Smith, R. B. (1989). Hydrostatic airflow over mountains. In *Advances in geophysics* (Vol. 31, pp. 1–41). Elsevier.

Smith, R. B., Skubis, S., Doyle, J. D., Broad, A. S., Kiemle, C., & Volkert, H. (2002). Mountain waves over mont blanc: Influence of a stagnant boundary layer. *Journal of the Atmospheric Sciences*, *59*(13), 2073–2092.

Smyth, W. D., & Moum, J. N. (2000). Anisotropy of turbulence in stably stratified mixing layers. *Physics of Fluids*, *12*(6), 1343–1362.

Smyth, W. D., & Moum, J. N. (2012). Ocean mixing by kelvin-helmholtz instability. *Oceanography*, *25*(2), 140–149.

Snyder, W. H., Thompson, R. S., Eskridge, R. E., Lawson, R. E., Castro, I. P., Lee, J., … Ogawa, Y. (1985). The structure of strongly stratified flow over hills: dividing-streamline concept. *Journal of Fluid Mechanics*, *152*, 249–288.

Spedding, G., Browand, F., & Fincham, A. (1996). The long-time evolution of the initially turbulent wake of a sphere in a stable stratification. *Dynamics of Atmospheres and oceans*, *23*(1-4), 171–182.

St. Laurent, L., & Garrett, C. (2002). The role of internal tides in mixing the deep ocean. *Journal of Physical Oceanography*, *32*(10), 2882–2899.

Sujovolsky, N., Mininni, P., & Pouquet, A. (2018). Generation of turbulence through frontogenesis in sheared stratified flows. *Physics of Fluids*, *30*, 086601.

Sutherland, B. (2002). Large-amplitude internal wave generation in the lee of step-shaped topography. *Geophysical research letters*, *29*(16), 16–1.

Suzuki, M., & Kuwahara, K. (1992). Stratified flow past a bell-shaped hill. *Fluid dynamics research*, *9*(1-3), 1–18.

Sveen, J. K., Guo, Y., Davies, P. A., & Grue, J. (2002). On the breaking of internal solitary waves at a ridge. *Journal of Fluid Mechanics*, *469*, 161–188.

Tennekes, H., Lumley, J. L., Lumley, J., et al. (1972). *A first course in turbulence.* MIT press.

Thompson, D. J., Latorre Iglesias, E., Liu, X., Zhu, J., & Hu, Z. (2015). Recent developments in the prediction and control of aerodynamic noise from high-speed trains. *International Journal of Rail Transportation*, *3*(3), 119–150.

Thorpe, S. (1977). Turbulence and mixing in a scottish loch. *Philosophical Transactions of the Royal Society of London. Series A, Mathematical and Physical Sciences*, *286*(1334), 125–181.

Thorpe, S. (1999). On the breaking of internal waves in the ocean. *Journal of physical oceanography*, *29*(9), 2433–2441.

Thorpe, S. (2004). Recent developments in the study of ocean turbulence. *Annu. Rev. Earth Planet. Sci.*, *32*, 91–109.

Thorpe, S. (2005). *The turbulent ocean.* Cambridge University Press.

Thorpe, S. (2010). Turbulent hydraulic jumps in a stratified shear flow. *Journal of Fluid Mechanics*, *654*, 305–350.

Thorpe, S., & Haines, A. (1987). On the reflection of a train of finite-amplitude internal waves from a uniform slope. *Journal of Fluid Mechanics*, *178*, 279–302.

Thorpe, S., & Li, L. (2014). Turbulent hydraulic jumps in a stratified shear flow. part 2. *Journal of Fluid Mechanics*, *758*, 94–120.

Thorpe, S., & Umlauf, L. (2002). Internal gravity wave frequencies and wavenumbers from single point measurements over a slope. *Journal of marine research*, *60*(5), 699–723.

Venayagamoorthy, S. (2006). *Energetics and dynamics of internal waves on a shelf break using numerical simulations* (Vol. 67) (No. 11).

Venayagamoorthy, S., & Fringer, O. (2006). Numerical simulations of the interaction of internal waves with a shelf break. *Physics of Fluids*, *18*(7), 076603.

Venayagamoorthy, S., & Fringer, O. B. (2007). On the formation and propagation of nonlinear internal boluses across a shelf break. *Journal of Fluid Mechanics*, *577*, 137–159.

Venayagamoorthy, S., & Fringer, O. B. (2012). Examining breaking internal waves on a shelf slope using numerical simulations. *Oceanography*, *25*(2), 132–139.

Venayagamoorthy, S., & Koseff, J. R. (2016). On the flux richardson number in stably stratified turbulence. *Journal of Fluid Mechanics*, *798*.

Venayagamoorthy, S., & Stretch, D. D. (2010). On the turbulent prandtl number in homogeneous stably stratified turbulence. *Journal of Fluid Mechanics*, *644*, 359–369.

Vlasenko, V., & Hutter, K. (2002). Numerical experiments on the breaking of solitary internal wavesover a slope–shelf topography. *Journal of Physical Oceanography*, *32*(6), 1779–1793.

Vlasenko, V., Stashchuk, N., & Hutter, K. (2005). *Baroclinic tides: theoretical modeling and observational evidence*. Cambridge University Press.

Voisin, B. (1991). Internal wave generation in uniformly stratified fluids. part 1. green's function and point sources. *Journal of Fluid Mechanics*, *231*, 439–480.

Vosper, S., Castro, I., Snyder, W., & Mobbs, S. (1999). Experimental studies of strongly stratified flow past three-dimensional orography. *Journal of Fluid Mechanics*, *390*, 223–249.

Waite, M. L., & Bartello, P. (2006). The transition from geostrophic to stratified turbulence. *Journal of Fluid Mechanics*, *568*, 89–108.

Walter, R. K., Squibb, M. E., Woodson, C. B., Koseff, J. R., & Monismith, S. G. (2014). Stratified turbulence in the nearshore coastal ocean: Dynamics and evolution in the presence of internal bores. *Journal of Geophysical Research: Oceans*, *119*(12), 8709–8730.

Waterhouse, A. F., MacKinnon, J. A., Nash, J. D., Alford, M., Kunze, E., Simmons, H. L., … others (2014). Global patterns of diapycnal mixing from measurements of the turbulent dissipation rate. *Journal of Physical Oceanography*, *44*(7), 1854–1872.

Wessels, F., & Hutter, K. (1996). Interaction of internal waves with a topographic sill in a two-layered fluid. *Journal of Physical Oceanography*, *26*(1), 5–20.

Wesson, J., & Gregg, M. (1988). Turbulent dissipation in the strait of gibraltar and associated mixing. In *Elsevier oceanography series* (Vol. 46, pp. 201–212). Elsevier.

Wijesekera, H., Jarosz, E., Teague, W., Wang, D., Fribance, D., Moum, J., & Warner, S. (2014). Measurements of form and frictional drags over a rough topographic bank. *Journal of Physical Oceanography*, *44*(9), 2409–2432.

Winters, K. B., & Armi, L. (2012). Hydraulic control of continuously stratified flow over an obstacle. *Journal of Fluid Mechanics*, *700*, 502–513.

Winters, K. B., Lombard, P. N., Riley, J. J., & D'Asaro, E. A. (1995). Available potential energy and mixing in density-stratified fluids. *Journal of Fluid Mechanics*, *289*, 115–128.

Wunsch, C. (1975). Internal tides in the ocean. *Reviews of Geophysics*, *13*(1), 167–182.

Wunsch, C., & Ferrari, R. (2004). Vertical mixing, energy, and the general circulation of the oceans. *Annu. Rev. Fluid Mech.*, *36*, 281–314.

Zang, Y. (1994). On the development of tools for the simulation of geophysical flows.

Zang, Y., Street, R. L., & Koseff, J. R. (1993). A dynamic mixed subgrid-scale model and its application to turbulent recirculating flows. *Physics of Fluids A: Fluid Dynamics*, *5*(12), 3186–3196.